

Influence of Meridional Width on Head-Curve Instability and Pump Performances

Vom Fachbereich Maschinenbau und Verfahrenstechnik
der Technischen Universität Kaiserslautern
zur Erlangung des akademischen Grades

Doktor-Ingenieur (Dr.-Ing.)

genehmigte

Dissertation

von

Herrn

M.Sc. Joohyen Kim

geb. in Seoul

Tag der mündlichen Prüfung:	30.04.2021
Dekan:	Prof. Dr.-Ing. Tilmann Beck
Vorsitzender:	Prof. Dr.-Ing. Eberhard Kerscher
Berichterstatter:	Prof. Dr.-Ing. Martin Böhle Prof. Dr.-Ing. Uwe Janoske

To my beloved wife in heaven, Tae Soon

Acknowledgements

This dissertation is a research output from 2015 to 2021 at the institute of Fluid Mechanics and Turbomachinery (SAM) in Technical University of Kaiserslautern.

I would like to appreciate Prof. Dr.-Ing. Martin Böhle, the director of SAM, for his professional guidance and personal encouragement. I also express my gratitude to the chairman of the PhD examination group, Prof. Dr.-Ing. Eberhard Kerscher, and the reviewer, Prof. Dr.-Ing. Uwe Janoske, for their support.

My special thanks go to Dr.-Ing. Johann Friedrich Gülich. He has provided me with many valuable comments and personal advices.

I wish to appreciate managers of HYOSUNG GOODSPRINGS, Mr. Woo Seop Lim, Mr. Hyeon Sig Kim, Mr. Sang Gyu Jeon, and Mr. Gyu Jin Park, for their long-term trust and financial support in the present study. My thanks also go to Dr.-Ing. Harald Roclawski, Mr. Artur Schimpf and Mr. Young Joon Ahn for their help in performing numerical simulations and designing test loop. I am very grateful to my colleagues, Mr. Jong Bum Kim, and Mr. Jin Ho Son, about the efforts for mechanical-component designs and experiments.

Finally, I express my deepest gratitude to my beloved wife, Tae Soon. She found peace with God in heaven. Thanks to her love, I could finish this dissertation. All my love goes to my children, Somang and Hamin.

Abstract

The present study deals with the cause of head-curve instability and the influence of impeller-outlet and diffuser-inlet width on pump performances. Experiments and Computational Fluid Dynamics (CFD) simulations were carried out on a 4-stage model pump. Three impellers and diffusers with different meridional-widths were designed for a specific speed around 30 [m³/s, m, rpm]. Overall-performance curves, stage-head curves, inlet recirculation in the 1st stage, internal-head curves in the 2nd stage and pressure profiles in the impeller side room were measured with 29 pressure sensors. Pressure pulsations were recorded at various positions in the multistage pump.

When the pump ran at the onset of the instability, an excessive head-loss was detected in the inlet triangular section of the diffuser. The pressure profiles in the side room and flow patterns in the impeller showed a sudden shift of flow recirculation at the impeller outlet across the span. According to [1, 2], this flow phenomenon is called *flow pattern switching*. The abrupt movement of outlet recirculation across the span produced a large momentum-exchange between streamlines and a massive mixing-loss in the inlet triangular section. This was considered the main cause of the instability.

As the meridional-width increased, flow recirculation at the impeller outlet was intensified, giving a higher head and power at shut-off. In contrast, the onset of the instability did not vary systematically with the meridional width. Diffuser rotating-stall was detected at $f/f_n = 0.029$ when the pump with the largest width ran at the onset of the instability. Even though all three designs generated a head-curve instability, the rotating stall appeared only in the largest meridional-width.

The uncertainty in the CFD prediction of pressure pulsations was evaluated. The discrepancy between measured and calculated values was largely dependent on the sampling location and operating points.

Kurzfassung

In der vorliegenden Dissertation werden die Ursache der Kennlinieninstabilität und der Einfluss der meridionalen Breite von Laufrad und Leitrاد auf die Leistungsdaten einer Radialpumpe untersucht. Die Ergebnisse basieren auf experimentellen Untersuchungen und Simulationen mittels Computational Fluid Dynamics (CFD). Als Versuchsobjekt dient eine vierstufige Modellpumpe. Je drei Laufräder und Leiträder mit unterschiedlichen meridionalen Breiten mit spezifischen Drehzahlen $n_q \approx 30$ [m³/s, m, rpm] wurden untersucht. Neben den Kennlinien der gesamten Pumpe, wurden die Förderhöhen der einzelnen Stufen, das Auftreten des Teillastwirbels in der ersten Stufe, die Druckerhöhung in Laufrad und Leitrاد sowie die Druckverläufe im Radseitenraum mit insgesamt 29 Drucksensoren aufgenommen. Druckpulsationen wurden in Saug- und Druckstutzen sowie am Leitradeintritt und im Radseitenraum gemessen.

Beim Einsetzen der Kennlinieninstabilität konnte ein signifikanter Förderhöhenabfall über den Schrägabschnitt am Leitradeintritt festgestellt werden. Wie Druckverläufe im Radseitenraum und berechnete Geschwindigkeitsverteilungen im Laufrad zeigen, verschiebt sich das Rezirkulationsgebiet am Laufradaustritt im instabilen Bereich von einer Radscheibe zur anderen. Nach [1, 2] kann dieses Phänomen als „flow pattern switching“ bezeichnet werden. Dieser Wechsel des Rezirkulationsgebiet erzeugt einen starken Impulsaustausch zwischen den Stromlinien und somit einen hohen Mischungsverlust am Eintritt des Leitrades. Hierin ist eine Hauptursache für die Entstehung der Kennlinieninstabilität zu sehen.

Die Untersuchungen zum Einfluss der meridionalen Breite auf die Leistungsdaten zeigen, dass breitere Laufräder die Rezirkulation am Laufradaustritt begünstigen; dadurch steigen Förderhöhe und Leistungsbedarf bei Nullförderung. Zwischen dem Einsetzen der Kennlinieninstabilität und der meridionalen Breite wurde kein systematischer Zusammenhang gefunden.

Druckpulsationsmessungen zeigten für die breiteste Variante rotierende Ablösungen im Leitrad mit einer Frequenz von $f/f_n = 0.029$. Alle Varianten weisen eine Kennlinieninstabilität auf; die rotierende Ablösung im Leitrad erschien aber lediglich in der breitesten Variante.

Die Unsicherheit der mit CFD berechneten Druckschwankungen wurde durch Vergleich mit der Messung bestimmt. Die Diskrepanz zwischen gemessen und CFD-berechneten Druckpulsationen hängt stark ab vom Ort der Auswertung und dem Betriebspunkt.

Contents

Acknowledgements	I
Abstract	III
Nomenclature	VIII
List of Figures	XV
List of Tables	XX
1 Introduction	1
1.1 Problem Overview and Motivation	1
1.2 Objective and Test Program	10
2 Experimental Investigation Method	13
2.1 Model Pump	13
2.2 Test Loop	18
2.3 Reynolds Number Dependence of Head Curves	20
2.4 Influence of Test Loop on Pressure Pulsations.....	22
3 Numerical Investigation Method	25
3.1 Governing Equations and Simulation Method	25

3.2	Near-wall Mesh Dependency Study	36
3.3	Numerical Setup	44
4	Data Analysis Method	48
5	Investigation of Head-curve Instability in a Multistage Pump	55
5.1	Performance Curve	55
5.2	Flow Pattern Switching.....	65
5.3	Discussion	75
6	Impact of Meridional Width and Width Ratio on Performance Curve and Pressure Pulsations	79
6.1	Effect of Meridional Width.....	79
6.2	Uncertainty in CFD Prediction of Pressure Pulsations.....	92
6.3	Effect of Width Ratio	97
7	Conclusion	100
	References	102
	List of Supervised Student Thesis	114
	Curriculum Vitae	115

Nomenclature

LATIN

b_2	[m]	meridional width at impeller outlet
b_2^*	[−]	relative width at impeller outlet = b_2/d_2
b_3	[m]	meridional width at diffuser inlet
b_3^*	[−]	relative width at diffuser inlet = b_3/d_2
BEP	[−]	best efficiency point
c	[m/s]	absolute flow-velocity
c_m	[m/s]	meridional component of flow velocity
c_u	[m/s]	circumferential component of flow velocity
$c_{\bar{p}}$	[−]	static-pressure coefficient
c_τ	[m/s]	friction velocity = $\sqrt{\tau_w/\rho}$
c^+	[−]	dimensionless velocity = c/c_τ
d, D	[m]	diameter
d_n	[m]	shaft diameter at impeller inlet

$d_{1\text{eff}}$	[m]	effective diameter of modified inlet-streamline
DFT	[−]	discrete Fourier transform
FFT	[−]	fast Fourier transform
f	[Hz]	frequency
f_n	[Hz]	rotational frequency = $N/60$
f_R	[Hz]	frequency resolution of the spectrum = $1/T$
f_s	[Hz]	sampling rate
g	[m/s]	gravitational acceleration
Gap A	[−]	radial clearance between shroud plates of impeller and diffuser = $r_{3D} - r_{2D}$
Gap B	[−]	radial clearance between impeller blade and diffuser vane = $r_3 - r_2$
H	[m]	total head = $p/(\rho g) + c^2/(2g) + z$
H_{ove}	[m]	total head of a multistage pump
H_s	[m]	static head
H_{th}	[m]	Euler head = $(u_2 c_{2u} - u_1 c_{1u})/g$
ISR	[−]	impeller side room
i	[°]	incidence angle = blade angle – flow angle
k	[m ² /s ²]	turbulent kinetic energy

$\overline{k_{shr}}$	$[-]$	average rotation factor in the front ISR
n_q	$[\text{m}^3/\text{s}, \text{m}, \text{rpm}]$	specific speed
N	$[\text{rpm}]$	rotational speed of a shaft = revolution/minute
NPSH_i	$[\text{m}]$	net positive suction head required for cavitation inception
$\text{NPSH}_{3\%}$	$[\text{m}]$	net positive suction head required for operation with 3% head drop
p	$[\text{Pa}]$	static-pressure
P	$[\text{W}]$	power
q^*	$[-]$	dimensionless flow-rate = Q/Q_{design}
q_b^*	$[-]$	dimensionless flow-rate in the current project = $Q/0.09064 [\text{m}^3/\text{s}]$
Q	$[\text{m}^3/\text{s}]$	flow rate
r	$[\text{m}]$	radius
Re	$[-]$	Reynolds number = $r_2 u_2 / \nu$
Re_{IEC}	$[-]$	Reynolds number according to IEC60193 = $d_{1a} u_{1a} / \nu$
RMS	$[-]$	root-mean-square
RSI	$[-]$	rotor-stator-interaction
s_{ax}	$[\text{m}]$	axial distance between impeller shroud and casing
t	$[\text{s}]$	time

T	[s]	total sampling time
u	[m/s]	circumferential speed of blade = $\pi dN/60$
VPF	[Hz]	blade passing frequency = $f_n z_{La}$
w	[m/s]	relative flow-velocity
x_i	[m]	Cartesian coordinates for $i = 1, 2, 3$
x_{ov}	[−]	axial overlap length between shroud plates of the impeller and diffuser
y^+	[−]	wall length-unit = $y/\delta_v = \nu\sqrt{\rho/\tau_w}$
z	[m]	height above a reference plane
z_{La}	[−]	number of impeller blade = 7
z_{Le}	[−]	number of diffuser vane = 12
z_{st}	[−]	number of stage = 4

GREEK

β	[°]	blade angle
δ_v	[m]	viscous length-scale = ν/c_τ
Δp	[Pa]	pressure pulsation = $p - \bar{p}$
Δp^*	[−]	dimensionless pressure-pulsation

$\widetilde{\Delta p}^*$	$[-]$	dimensionless pressure-pulsation averaged over each shaft rotation
Δp_{ove}^*	$[-]$	overall RMS value of dimensionless pressure-pulsation
Δp_{RMS}^*	$[-]$	RMS value of dimensionless pressure-pulsation
ϵ	$[\text{m}^2/\text{s}^3]$	dissipation of turbulent kinetic energy
$\zeta_{\text{E},1\text{st}}$	$[-]$	loss coefficient in a suction casing
η	$[-]$	efficiency
η_n	$[-]$	efficiency coefficient
λ	$[-]$	power coefficient
μ	$[\text{kg}/(\text{ms})]$	dynamic viscosity
ν	$[\text{m}^2/\text{s}]$	kinetic viscosity $= \mu/\rho$
ν_T	$[\text{m}^2/\text{s}]$	kinetic turbulent-viscosity
ρ	$[\text{kg}/\text{m}^3]$	density
σ_n	$[-]$	normalized standard deviation = standard deviation/mean
τ	$[\text{Pa}]$	viscous shear-stress
ψ	$[-]$	total-head coefficient
ψ_s	$[-]$	static-head coefficient
ω	$[\text{rad}/\text{s}]$	angular rotor velocity

SUBSCRIPT

1	impeller blade leading edge
2	impeller blade trailing edge
2D	outer of impeller shroud plate
3	diffuser vane leading edge
3D	inner of diffuser shroud plate
3q	diffuser inlet throat
4q	diffuser outlet throat
6	return vane outlet
a, m, i	shroud, mean, and hub layer
La	impeller
Le	diffuser
m	meridional component
opt	operation at BEP
u	circumferential component
w	wall

SUPERSCRIPT

— time average

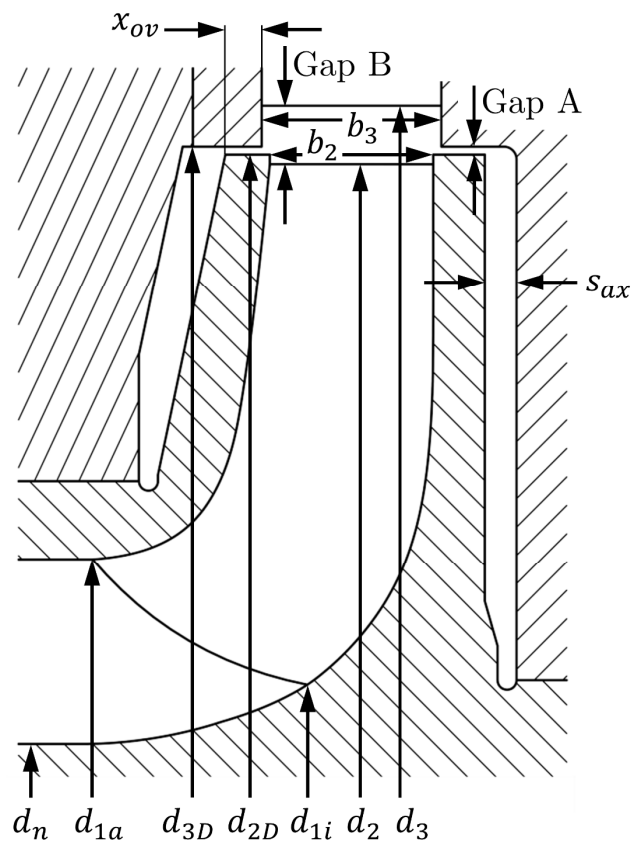


Figure 0.1: Geometric dimensions

List of Figures

Figure 0.1:	Geometric dimensions	XIV
Figure 1.1:	Typical patterns of flow recirculation in the impeller	2
Figure 1.2:	Meridional section of three impellers and diffusers with an assembly condition of $b_3/b_2 = 1.1$	10
Figure 2.1:	Model pump sectional drawing with measurement details.....	13
Figure 2.2:	Static-pressure and dynamic-pressure measurement locations in the 2 nd stage.....	14
Figure 2.3:	Miniature pressure-pulsation sensors installed in the 2 nd stage.....	17
Figure 2.4:	4-stage model pump	17
Figure 2.5:	Test loop	18
Figure 2.6:	Overall-head curves at different Reynolds numbers.....	20
Figure 2.7:	Overall RMS values of dimensionless pressure-pulsations at the discharge nozzle for various rotational-speeds.....	22
Figure 2.8:	Spectra of dimensionless pressure-pulsations at the discharge nozzle for various flow-rates at $Re_{IEC} = 5 \times 10^6$	23
Figure 3.1:	Comparison of predicted flow-fields past a circular cylinder.....	31
Figure 3.2:	Schematic drawing of spatial discretization in ANSYS CFX.....	35
Figure 3.3:	Computation domain of the single-stage pump for the near-wall mesh dependency study	37

Figure 3.4:	Top – predicted velocity-profiles in the boundary layer depending on y^+ , Bottom – mesh shapes around the impeller leading edge at $y^+ = 48.5$ and 2.0 ($q_b^* = 1.0$)	37
Figure 3.5:	Variation of pump performances depending on y^+ ($q_b^* = 1.0$)	38
Figure 3.6:	Span-wise distribution of dimensionless meridional and circumferential-velocity components at the impeller outlet for different y^+ ($q_b^* = 1.0$)	39
Figure 3.7:	Variation of pump performances depending on y^+ ($q_b^* = 0.75$)	40
Figure 3.8:	Span-wise distribution of dimensionless meridional and circumferential-velocity components at the impeller outlet for different y^+ ($q_b^* = 0.75$)	41
Figure 3.9:	Dimensionless relative-velocity contours on the suction side of the impeller blade leading edge; span-position is near hub (span = 0.95) ($q_b^* = 0.75$)	42
Figure 3.10:	Computational domain for the 4-stage model pump.....	44
Figure 3.11:	Variation of pump performances at different mesh resolutions in the mean-flow passages ($q_b^* = 1.0$, $y^+ = 24.7$).....	45
Figure 3.12:	Computational domains and interfaces in the 2 nd stage.....	47
Figure 4.1:	Spectra of dimensionless pressure-pulsations measured at the diffuser inlet in the 2 nd stage of the model pump ($q_b^* = 1.0$)	53
Figure 5.1:	Overall-performance curves of Test-05.....	55
Figure 5.2:	Stage-head curves of Test-05 from the measurement.....	57
Figure 5.3:	Loss coefficient in the suction casing and the onset flow-rate of inlet recirculation of Test-05 from the measurement	58
Figure 5.4:	2 nd stage internal-head curves of Test-05 from the measurement	60

Figure 5.5:	Pressure recovery in the diffusing channels of Test-05 from the measurement and its quadratic fitting curve by the least-squares-method.....	61
Figure 5.6:	2 nd stage internal-head curves of Test-05	64
Figure 5.7:	Static-head curves in the inlet triangular section and diffusing channels in the 2 nd stage of Test-05.....	64
Figure 5.8:	Average rotation factors on the front ISR in the 2 nd stage of Test-05	65
Figure 5.9:	Pressure-coefficient distribution on the front ISR in the 2 nd stage of Test-05	66
Figure 5.10:	Span-wise velocity distribution at the impeller outlet in the 2 nd stage from the CFD of Test-05.....	67
Figure 5.11:	Dimensionless meridional-velocity contours with vectors in the 2 nd stage impeller from the CFD of Test-05	69
Figure 5.12:	Dimensionless velocity contours in the 2 nd stage diffuser of Test-05 from the CFD.....	71
Figure 5.13:	Close-up view of Fig. 5.12 between 9 and 12 o'clock position.....	72
Figure 5.14:	Span position definition for Fig. 5.12 and 5.13	73
Figure 5.15:	Dimensionless velocity contours at the diffuser inlet throat in the 2 nd stage from the CFD of Test-05	74
Figure 5.16:	Span-wise velocity distribution at the impeller outlet in the 2 nd and last stage from the CFD of Test-05	78
Figure 5.17:	Dimensionless velocity contour in the last stage diffuser, annular chamber and discharge casing of Test-05 from CFD.....	78
Figure 6.1:	Overall-performance curves of different meridional-widths from the measurement.....	79

Figure 6.2:	2 nd stage internal-head curves of different meridional-widths from the measurement.....	81
Figure 6.3:	Average rotation factors on the front ISR in the 2 nd stage from the measurement.....	82
Figure 6.4:	Dimensionless meridional-velocity distribution in the span-wise direction at the 2 nd stage impeller outlet from the CFD at BEP	84
Figure 6.5:	Dimensionless absolute-velocity distribution in the pitch-wise direction at the 2 nd stage impeller outlet from the CFD at BEP	85
Figure 6.6:	Overall RMS values of dimensionless pressure-pulsations measured at the suction nozzle (PT27), discharge nozzle (PT28) and diffuser inlet in the 2 nd stage (PT31).....	86
Figure 6.7:	Overall RMS values of dimensionless pressure-pulsations measured at the front ISR at d_2 (PT29) and diffuser inlet (PT31) in the 2 nd stage of Test-01	87
Figure 6.8:	Spectra of dimensionless pressure-pulsations measured at PT31 in Test-01 for different flow-rates	90
Figure 6.9:	Coherence between PT29 and PT31 of Test-01 at $q_b^* = 0.62$	91
Figure 6.10:	Dimensionless pressure-pulsations at PT31 averaged over each impeller revolution of Test-01 at $q_b^* = 0.62$	91
Figure 6.11:	Overall RMS values of dimensionless pressure-pulsations of Test-05	92
Figure 6.12:	Spectra of dimensionless pressure-pulsations at PT31 of Test-05	94
Figure 6.13:	Overall RMS values of dimensionless pressure-pulsations at PT31 for the different meridional-widths	95

Figure 6.14: Overall-head curves of different b_3/b_2 from the measurement	99
---	----

List of Tables

Table 1.1:	Test program for different meridional-widths at a constant b_3/b_2	12
Table 1.2:	Test program for different b_3/b_2 at a constant b_2^*	12
Table 2.1:	Main data of the 4-stage model pump with Test-01 configuration	14
Table 2.2:	Pressure-pulsations measurement information	15
Table 3.1:	Near-wall mesh dependency study	36
Table 3.2:	Number of mesh nodes	46
Table 4.1:	Mean, RMS and peak-to-peak definitions	48
Table 4.2:	Non-dimensionalization and variable definitions	49
Table 6.1:	Main performance data of Test-01, 05 and 06	80
Table 6.2:	Geometric dimensions and shut-off head of Test-04, 05 and 07	98

1 Introduction

1.1 Problem Overview and Motivation

It is well known that centrifugal pumps equipped with vane diffusers are prone to the head-curve instability at part-load when the specific speed is larger than around 30 [m³/s, m, rpm] [1–7]. A positive slope in the head curve ($dH/dQ > 0$) needs to be avoided because it restricts the allowable operating range of a pump.

Various studies [1-5, 8] reported that the cause of the instability is related to flow separation in hydraulic passages of a pump. When an operating flow-rate is significantly below BEP flow-rate, flow angle at the leading edge of impeller blades and diffuser vanes becomes too small compared to the blade and vane angle. A large reduction of fluid velocity in hydraulic passages and the large mismatch between the flow and blade angle initiate flow separation. At sufficiently low flow-rates, flow recirculations appear at the impeller inlet and outlet [8-10]. Typical recirculation patterns are depicted in Figure 1.1.

Hergt and Starke [4] investigated flow phenomena linked to the head-curve instability in a single-stage pump. When the pump ran near the onset flow-rate of the instability, a backflow with negative circumferential-velocity component was detected near the shroud at the diffuser inlet. The authors described that the instability was caused by this backflow. Later Hergt and Jaberg [5] measured velocity distributions at the impeller outlet in three different pumps. Distinct flow-separations were observed near the shroud at the onset of the instability in all pumps. They reported that flow separation generating the instability started in a form of a rotating stall. A hypothesis about the origin of the instability was suggested by Gülich, called *flow pattern switching* [1, 2]. He carried out model-pump tests by changing two different impellers in a given diffuser. Impeller A produced a stable head-curve, but impeller B an instability at part-load. Velocity profiles measured at the impeller outlet showed that there was a difference of

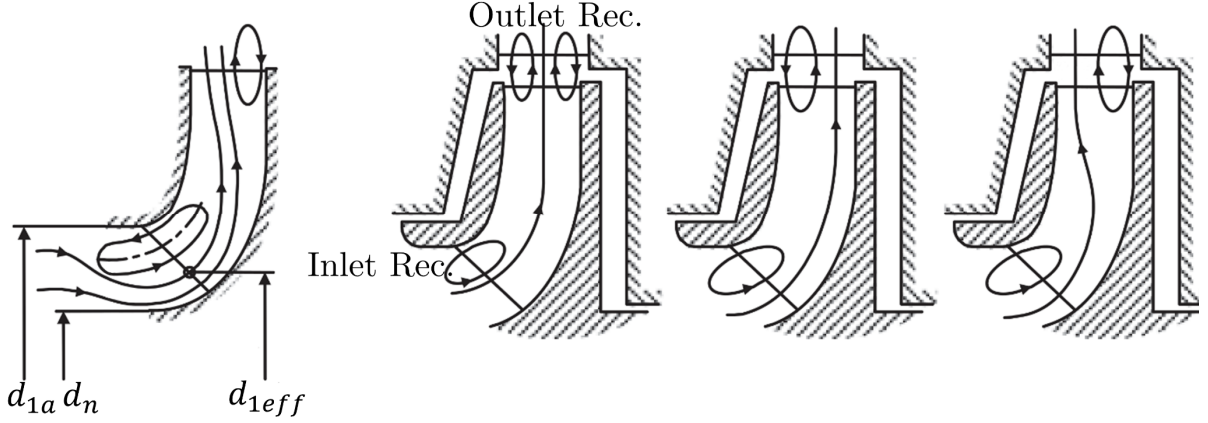


Figure 1.1: Typical patterns of flow recirculation in the impeller [adapted from [3]]

flow-recirculation pattern. Outlet recirculation in the impeller A appeared near the shroud at part-load and became stronger as the operating flow-rate decreased. However, outlet recirculation in the impeller B did not stay at a constant position but moved across the span as the operating point varied. Gülich named this phenomenon as flow pattern switching. Eisele *et al* [8] observed flow-field in a diffuser-type pump using Laser Particle Tracking Velocimetry (LPTV) and Laser Doppler Anemometry (LDA) techniques. The model pump had the head-curve instability in a range of $q^* = 0.65 \sim 0.55$. Measurement results showed that there was a movement of outlet recirculation from the shroud to hub while the dimensionless flow-rate was reduced from 0.68 to 0.50, i.e. the flow pattern switching occurred near the onset of the instability.

Even though some design guidelines were suggested to avoid the positive slope in the head curve [3, 6], the instability is still an unsolved problem. There is no reliable design-rule to ensure a continuously rising head-curve toward shut-off yet. The main difficulty in the instability study is that outlet recirculation is affected by various hydraulic parameters in a complex manner. Literatures were reviewed to investigate the impact of geometric and operating parameters on the instability and pump performances. Some key findings are summarized below:

- (1) **Collector type (diffuser vs volute):** The collector type has a large influence on head-curve instability, shut-off performance, and hydraulic excitation forces [1, 7, 11–13]. Kanki *et al* [7] carried out model-pump tests

by changing a diffuser and volute in a given radial-impeller. There was a noticeable difference in the head curves. The diffuser configuration gave a flat head-curve at part-load, but the volute an unstable head-curve near shut-off. In general, a volute is designed with a larger radial clearance between the impeller outlet and cutwater (Gap B), a larger inlet meridional-width (b_3), and a smaller angle at the cutwater (β_3) compared to a diffuser. There are usually one or two cutwaters in a volute, but seven to twelve vanes in a diffuser. These differences make a volute react in a less sensitive way to a large incidence-angle (=blade angle – flow angle) and non-uniform flow distributions at the impeller outlet that appear at reduced operating flow-rates. The instability at part-load is rarely found in volute-type pumps below $n_q = 70$ [3].

- (2) **Flow pattern at the impeller inlet:** Head generation and hydraulic excitations in a pump are affected by velocity distribution of the approach flow. Gülich [13] measured head curves of a single-stage model pump with changing an axial and a radial inlet casing in a given impeller. The results were compared with a head curve measured in 2nd stage of a 3-stage multistage pump that was equipped with the same hydraulic components. Three head-curves were distinctly different from each other, especially at part-load. It was because the different inlet-velocity profiles changed the head generation and flow patterns in the impeller, which subsequently affected pressure recovery in the diffuser. Van Esch [14] reported that fluid-induced forces on a rotor of a single-stage mixed-flow pump significantly varied depending on inlet-velocity profiles.
- (3) **Number of blades:** Blade solidity (=blade length over circumferential spacing between blades) is one of the main parameters to determine blade loading [15–17]. A too small number of blades generates a high blade-loading and non-uniform flow-distribution over the impeller circumference, causing large mixing-losses and pressure-pulsations [3]. Therefore, a proper selection of the number of blades may improve pump performances, e.g. in [16]. The number of blades affects energy transfer from the blades to fluid. A larger number of blades decreases *slip* at the impeller outlet (=deviation of the flow angle from the blade angle) and increases head near BEP. However,

circumferential spacing in the individual blade-channel becomes narrower with increasing number of blades, which is likely to weaken the intensity of flow recirculation at part-load and shut-off. Baun und Flack [18] performed model-pump tests using two impellers with different numbers of blades in a single-stage pump. An impeller with four blades generated lower head near BEP and higher head near shut-off than one with five blades. Consequently, a lesser number of blades had a steeper head-curve.

- (4) **Shape of the blade leading edge:** At part-load, flow angle at the blade leading edge is smaller than the blade angle. A proper profiling at the leading edge mitigates the mismatch between the blade and flow angle, which may delay the onset of flow separation into a smaller flow-rate. Riegger and Nicklas [19] reported that a well-profiled leading edge of the diffuser vane could suppress the head-curve instability and improve the pump efficiency at reduced operating-points. It is well known that the leading-edge geometry of an impeller is an important design parameter for cavitation performance [20–24]. For high-energy pumps with a high circumferential-speed at the blade inlet (e.g. boiler feed application), it is preferable to avoid occurrence of any cavitation within operating ranges since the impeller blade may be seriously damaged by cavitation erosion. An asymmetric profile at the leading edge is known to give a mild increase of the static pressure near the blade inlet, which reduces the cavity length for a given suction pressure [3]. Several studies reported an improvement of the cavitation inception ($NPSH_i$) by means of a suction-side profiling at the leading edge [22] or a biased-wedge-shape profiling [23, 24].
- (5) **Impeller-Side-Room design (ISR):** Fluid at the impeller outlet enters (or comes out of) the ISR through a small gap between shroud plates of the impeller and diffuser. The radial clearance between two plates (Gap A) and the axial overlap length between them (x_{ov}) determine the degree of interaction between main flow at the impeller outlet and side flow in the ISR. The effect of ISR design on the head curve and axial thrust of pumps was extensively reviewed by [25]. Makay and Barrett [26] reported that the head-curve instability, pump noise and vibration were changed by modifying Gap A, Gap B, and x_{ov} in multistage pumps. Several studies [4, 27, 28]

described that the axial displacement of centerlines of the impeller and diffuser affected the head curve and axial thrust. It is because the axial offset of a rotor changes ISR geometries (x_{ov} and side gap clearance in the ISR (s_{ax})), which results in a different coupling between the main flow and side-room flow.

- (6) **Impeller inlet diameter:** The blade inlet diameter at the shroud (d_{1a}) and hub (d_{1i}) affects not only the cavitation performance, but also the head-generation and power-consumption at part-load and shut-off [3, 17, 29–31]. Considering the Euler head equation,

$$\begin{aligned}
 Gl. 1-1 \quad H_{th} &= \frac{u_2 c_{2u} - u_1 c_{1u}}{g} \\
 Gl. 1-2 \quad &= \frac{u_2^2 - u_1^2}{2g} + \frac{c_2^2 - c_1^2}{2g} - \frac{w_2^2 - w_1^2}{2g}
 \end{aligned}$$

the first term in (Gl. 1-2) is the head-development by the centrifugal effect from the blade inlet to outlet. Note that it is independent on the operating flow-rate, i.e. the centrifugal head-rise is supposed to be constant over the whole flow-range based on the Euler head equation. However, it is true only when there is no flow recirculation in the impeller. Once inlet recirculation occurs at part-load, the effective streamline at the impeller inlet is shifted toward the hub as depicted in the left side in Fig. 1.1 where d_{1eff} is an effective diameter of the modified inlet-streamline. Then, the centrifugal head-rise in (Gl. 1-2) increases since the minus u_1^2 becomes smaller. The gain of the theoretical head due to the inlet recirculation can be roughly estimated as $\Delta H_{Rec} = u_2^2(d_{1a}^2 - d_{1eff}^2)/(2gd_2^2)$ according to [1]. Yedidiah [29] reported that a forward advancement of the blade leading edge in the meridional section produced higher shut-off head. It was most likely due to the reduced d_{1i} since fluid could receive more energy from the blade inlet, i.e. higher centrifugal head-rise under the inlet recirculation. Gülich and Egger [1] reported test results of a 3-stage model pump that a larger d_{1a} increased the shut-off head. A similar result can be found in Breugelmans and Sen's tests [30] that a larger d_{1a}/d_{1i} gave higher head and power at shut-off (even though some other design parameters also changed in the same time). It is

because inlet recirculation becomes stronger with increasing d_{1a} [31].

- (7) **Blade angle distribution along the streamline:** The blade angle development from the inlet to outlet determines velocity and loading distributions on the blade surface [17, 32–35]. If the blade angle rapidly increases near the inlet, a high blade-loading is formed near the leading edge. It gives a large drop in the static pressure on the blade inlet, resulting in a poor cavitation-performance [3]. Various studies reported that the control of angle development had a substantial change on performance curves since secondary-flow pattern in the impeller was affected [32–35]. The effect of the blade-angle distribution on hydraulic excitation forces in a single-blade pump can be found in [36].
- (8) **Rake angle:** The rake angle of an impeller is defined as an angle between the hub plate and blade trailing edge in span-wise direction. The rake angle affects the span-wise pressure-gradient near the blade outlet. Van den Braembussche [37] showed a significant change of velocity distributions in the meridional plane when the rake angle was applied. Zangeneh *et al* [34] reported that a modification of the rake angle (combined with an adjustment of the blade angle distribution) resulted in a distinct variation of flow patterns in radial and semi-axial impellers.
- (9) **Impeller outlet width:** The meridional width at the impeller outlet has a substantial influence on outlet recirculation and velocity uniformity. The recirculation plays an important role in head-rise and power-consumption at reduced flow-rates since it brings fluid with low c_u from the diffuser to impeller and re-accelerates it. Gülich [1, 3] and Karassik *et al* [17] described that a larger b_2^* tends to intensify outlet recirculation, which results in a higher head and power at shut-off. However, a wider impeller is likely to make velocity distribution at the impeller outlet less uniform in the span-wise direction. Then, one may assume that a larger meridional-width generates flow separation and outlet recirculation at a higher flow-rate, and increases hydraulic-losses. Schill [6] suggested that head curve might be stabilized by reducing b_2^* , but no supporting data was furnished. Gottschalk [38] reported that fans with a small b_2^* rarely showed unstable head-curve at part-load. There is little experimental data available to clarify the impact of

the meridional width on the head-curve instability and hydraulic losses in centrifugal pumps.

(10) Width ratio of the diffuser inlet to impeller outlet (b_3/b_2): When fluid exits the impeller outlet, a sudden deceleration of the meridional velocity occurs due to an abrupt increase of the width from the impeller outlet to diffuser inlet. Presumably, a larger width-ratio (b_3/b_2) intensifies the flow deceleration, and then flow recirculation and instability may occur at a higher flow-rate. To the best of the author's knowledge, the only published measurement data regarding b_3/b_2 is in [1]. Inlet width of the last-stage diffuser in a multistage pump was modified to investigate two different $b_3/b_2 = 1.12$ and 0.93 . A larger b_3/b_2 produced a higher shut-off head and power. More interestingly, the head-curve instability appeared at a higher flow-rate. However, there is a limitation to interpret the test result because the diffuser inlet was narrower than the impeller outlet in the test case of the small b_3/b_2 . It gave an *acceleration* of the meridional velocity between the impeller outlet and diffuser inlet rather than the deceleration.

The current study investigates the impact of meridional width and width-ratio on pump performances. Model-pump tests were carried out by varying b_2^* and b_3^* of impellers and diffusers. A change of meridional width requires an adjustment of blade-outlet-angle (β_2) to achieve the same head-coefficient in a constant d_2 . A narrower width is expected to improve outlet-flow quality in the span-wise direction. However, it may deteriorate velocity uniformity over the impeller circumference due to the increased β_2 . These possible counter-acting tendencies of velocity uniformity in the span-wise and pitch-wise direction suggest that there would be an optimum b_2^* for a given specification to minimize hydraulic losses and pressure pulsations. These hypotheses are examined in the present work.

Pressure pulsations in centrifugal pumps and their influence on rotor-dynamics, mechanical stresses, vibrations and piping systems were investigated in many studies, e.g. [39–43]. There are various sources to create pressure pulsations, but the strongest one is normally wake flow exiting the impeller blade outlet and its impingement on the diffuser vane leading edge (or volute cutwater), called rotor-stator-interaction (RSI). It generates strong pressure-pulsations at

vane passing frequency and its super-harmonics frequency components [40]. Pressure pulsations usually increase with decreasing flow-rate because various sizes of turbulent structures are created by flow separation and recirculation that gives the pressure pulsations over certain frequency ranges (=broadband) [1, 40]. Measurement data of unsteady pressure distributions in hydraulic passages can be found in various literatures, e.g. [44-48]. Another source of pressure pulsations is a geometric deviation of impeller blade channels. Impellers are usually manufactured by casting methods in industrial applications. Dimensional deviations between blade passages are frequently observed that may produce unbalanced hydraulic-force and pressure pulsations at the rotating frequency and/or its super-harmonics [3, 49]. Vane number combination between the impeller and diffuser has a significant effect on pressure mode-shapes in the pump [3, 42, 50-53]. Flow exiting the impeller outlet has a periodicity in the pressure field corresponding to the number of impeller blades (z_{La}) and its integer multipliers as $v_2 z_{La}$ for $v_2 = 1, 2, 3 \sim \infty$. The diffuser also generates a periodicity in the pressure field as $v_3 z_{Le}$ where z_{Le} is the number of diffuser vanes and $v_3 = 1, 2, 3 \sim \infty$. Fourier series of these two pressure-fields and its modulation give two interaction components, $k_1 = v_2 z_{La} - v_3 z_{Le}$ and $k_2 = v_2 z_{La} + v_3 z_{Le}$, defining diametral pressure mode-shape on the impeller shroud due to RSI. Detailed derivation can be found in several literatures [42, 50, 51]. k_2 has little practical value for centrifugal pumps since the corresponding pressure-pulsations are located at very high frequencies and thus have a little energy level. However, k_1 is important to select an appropriate number of the impeller blade and diffuser vane. When the absolute value of k_1 is zero (i.e. when number of impeller blades and diffuser vanes have common integer multipliers), a pressure field with zero diametral mode appears on the impeller shroud. This hydraulic excitation is an umbrella shape, resulting in a strong axial force and pressure pulsations. $|k_1| = 1$ means one diametral mode (=positive pressure-pulsation in the half of impeller shroud and negative in the remaining half) and generates a strong radial-force. $|k_1| = 2$ gives a pressure field with two diametric nodes. In general, the vane combination must be selected in a way to avoid $|k_1| = 0$ and 1 in the first and second order of v_2 and v_3 to prevent strong vibrations and pressure-pulsations [3]. When a pump runs in a condition of $NPSH_{av} <$

NPSH_i, vapor bubbles are formed in the impeller blade and pressure pulsations are created due to implosions of cavitation bubbles. The cavitation-induced pressure pulsations usually appear above kilohertz frequency range [54, 55]. Rotating stall in the impeller and diffuser creates pressure pulsation at a discrete frequency below the rotational frequency of the shaft [42, 48, 56, 57]. Sinha *et al* [56] detected rotating stall in a diffuser-type single-stage pump at $f = 0.93$ Hz when the pump ran near the onset flow-rate of head-curve instability. Takamine *et al* [57] reported a distinct peak in pressure pulsations at around $f = 1.7$ Hz that was caused by the diffuser rotating stall in a 3-stage pump. The operating point was in an unstable range of the head-curve near shut-off.

1.2 Objective and Test Program

The present work investigates the influence of meridional width at the impeller outlet and diffuser inlet on head-curve instability, performance curve, and pressure pulsations in a 4-stage model pump. Impellers and diffusers with three different meridional-widths were designed at around $n_q = 30$. Overall-performance curves, stage-head curves, suction recirculation, 2nd stage internal-head curves and pressure profiles in the impeller side room were measured. Pressure pulsations were sampled at various positions in the multistage pump. Computational Fluid Dynamics (CFD) simulations were carried out to interpret the measurement data and estimate flow-patterns in the hydraulic components.

Blade outlet angles for the three impellers with different b_2^* were selected to achieve a constant ψ_{opt} for a given d_2 . A systematic design procedure according to [3] was applied for the development of the impellers and diffusers to minimize arbitrary choices of geometric parameters. Figure 1.2 shows meridional shapes of the three impellers and diffusers in a constant $b_3/b_2 = 1.1$. The shroud contour of the impellers was kept constant and only the hub contour was modified from the inlet to outlet to achieve the different b_2^* . The blade angle distribution was determined using a pre-defined shape-function that enabled a

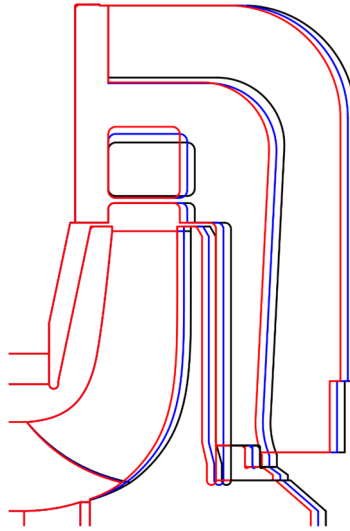


Figure 1.2: Meridional section of three impellers and diffusers with an assembly condition of $b_3/b_2 = 1.1$; Test-01 – black, Test-05 – blue, Test-06 – red

smooth β development from the trailing edge to leading edge. The three diffusers with different b_3^* were designed as follows:

- (1) Inlet throat area was the same to keep a constant BEP flow-rate.
- (2) Vane inlet diameter was the same for a constant Gap B.
- (3) Vane outlet diameter was the same.
- (4) Suction side of the vane leading edges was profiled.
- (5) Outlet angle of the return vanes was the same.
- (6) Expansion angle in the diffusing-channel area along the streamline was similar.

Other main design parameters are: impeller blade number = 7, diffuser vane number = 12, Gap B_{1st&4th stage}/ r_2 = 0.08, and Gap B_{2nd&3rd stage}/ r_2 = 0.06.

Three tests were carried out to investigate the influence of meridional width on pump performances at a constant b_3/b_2 , which is summarized in Table 1.1. Using the available hydraulic components, three additional tests were performed by varying b_3/b_2 in a given b_2^* as shown in Table 1.2. The impellers and diffusers from 2nd to 4th stages were replaced at each test according to the test programs in Table 1.1 and 1.2. However, the suction impeller and diffuser were not changed during the whole test since they were designed for the cavitation performance.

Table 1.1: Test program for different meridional-widths at a constant b_3/b_2

	Test-01		Test-05		Test-06	
Stage	1 st	2 nd , 3 rd , 4 th	1 st	2 nd , 3 rd , 4 th	1 st	2 nd , 3 rd , 4 th
b_2^*	0.086	0.086	0.086	0.078	0.086	0.071
b_3/b_2	1.1	1.1	1.1	1.1	1.1	1.1
$i_{3,BEP}$ [°]	1.0	1.0	1.0	1.0	1.0	1.0

Table 1.2: Test program for different b_3/b_2 at a constant b_2^*

	Test-04		Test-05		Test-07	
Stage	1 st	2 nd , 3 rd , 4 th	1 st	2 nd , 3 rd , 4 th	1 st	2 nd , 3 rd , 4 th
b_2^*	0.086	0.078	0.086	0.078	0.086	0.078
b_3/b_2	1.1	1.0	1.1	1.1	1.1	1.21
$i_{3,BEP}$ [°]	1.0	1.1	1.0	1.0	1.0	1.3

2 Experimental Investigation Method

2.1 Model Pump

The 4-stage model pump was built with a suction casing, a suction impeller, series impellers for 2nd, 3rd and 4th stage, diffusers with return vanes for 1st, 2nd and 3rd stage, a last stage diffuser, a discharge casing, and a balance drum. The sectional drawing and main data of the constructed pump are presented in Fig. 2.1 and Table 2.1, respectively. The impellers in each stage were arranged in a staggering manner to reduce hydraulic excitation forces. Following performances were measured using the model pump:

- | | |
|--------------------------------|--------------------------|
| A: Axial thrust | I: Internal-head curves |
| B: Balance drum inlet-pressure | L: Balance leakage flow |
| C: Cavitation visualization | R: Suction recirculation |
| D: Pressure pulsation | S: Stage-head curves |

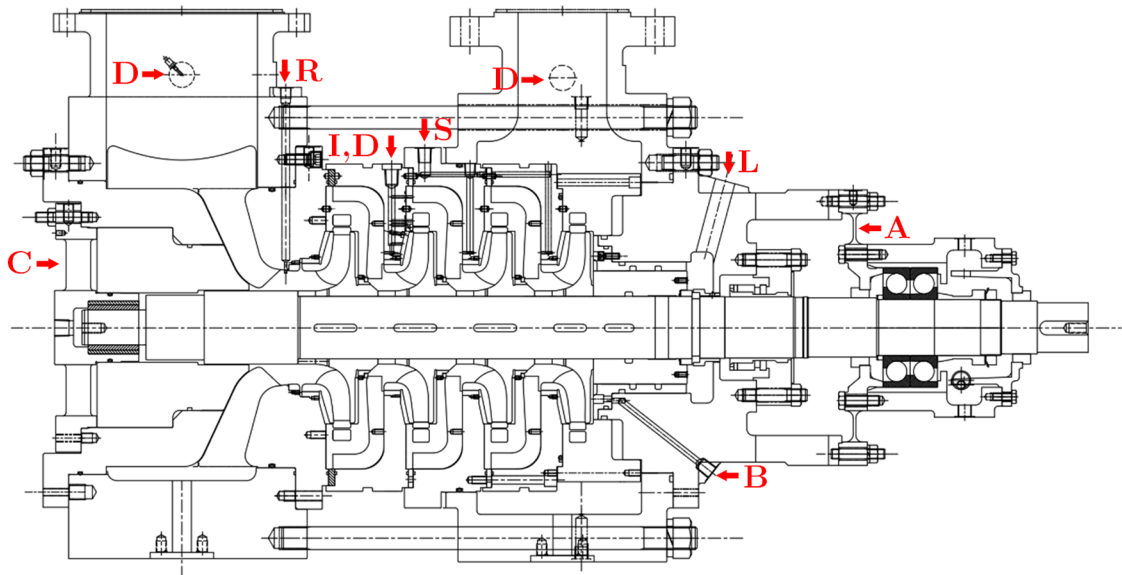


Figure 2.1: Model pump sectional drawing with measurement details

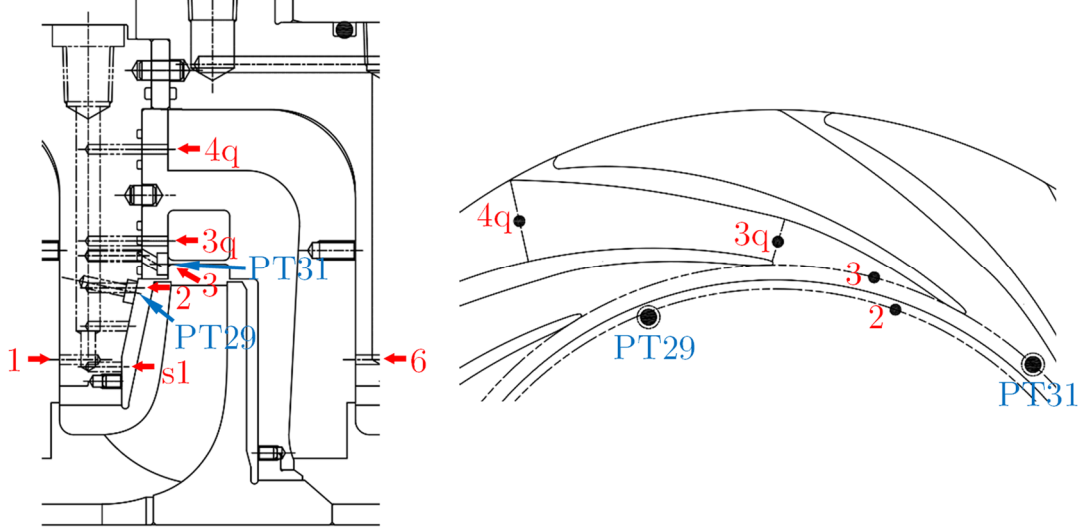


Figure 2.2: Static-pressure and dynamic-pressure measurement locations in the 2nd stage

- (1) overall-performance curves – flow, head, torque, rotational speed of the shaft
- (2) stage-head curves
- (3) internal-head curves in the 2nd stage
- (4) pressure profile on the front ISR of the 2nd stage
- (5) pressure pulsations at various positions in the multistage pump
- (6) suction-casing loss and onset flow-rate of the inlet recirculation in the 1st stage
- (7) leakage flow-rate through the balance drum
- (8) static-pressure difference across the balance drum
- (9) axial thrust
- (10) cavitation performance and visualization of the 1st stage: NPSH_i, NPSH_{3%}

The measurement results from (1) to (6) are discussed in this work. Static-pressure distributions in the multistage pump were measured with 29 pressure

Table 2.1: Main data of the 4-stage model pump with Test-01 configuration

N	[rpm]	2400	d_2	[m]	0.3
Q_{opt}	[m ³ /s]	325	b_2	[m]	0.0257
H_{opt}	[m]	277.5	d_3	[m]	0.318
$n_{q,opt}$	[m ³ /s, m, rpm]	30	b_3	[m]	0.0283

sensors through pressure taps drilled on the casing walls. Figure 2.2 shows detailed measurement locations in the 2nd stage. PT29 and PT31 indicate tag numbers of pressure-pulsation sensors and others represent evaluation stations for internal-head curves. Static pressures were measured at two or three different circumferential positions at each evaluation station, and their averaged values were used for the data analysis. Pressure pulsations at the suction and discharge nozzles were sampled using typical quartz-type piezoelectric sensors manufactured by PCB Piezotronics. In the 2nd stage, miniature dynamic-pressure sensors with diameter 9.5 mm and thickness 4.2 mm were used considering the space limitation (Fig. 2.3). All dynamic-pressure sensors were flush-mounted. Table 2.2 shows pressure-pulsation measurement details. The 4-stage model pump is shown in Fig. 2.4.

All unsteady signal was recorded at a sampling rate of 25.6 kHz during 60 s to obtain a fine frequency-resolution ($f_R = 0.0167$ Hz) in the spectra. However, when the operating point was below $q_b^* = 0.3$, the sampling time was reduced to 20 s to avoid mechanical damages caused by the increased vibration and hydraulic excitations. A new data acquisition (DAQ) system was developed using Labview software and National Instrument equipment. Analog low-pass filters at 9.0 kHz were inserted ahead of DAQ devices to prevent aliasing error. Hanning window was applied in the post processing of collected unsteady-data [58], but spectral outputs with and without Hanning window were carefully reviewed to avoid any error caused by the window function. Matlab was used for post processing of the collected data.

Reading-scale measurement uncertainties according to [59] were static-

Table 2.2: Pressure-pulsation measurement information

Tag no.	Installation position	Sensor type	Natural frequency
PT27	Suction nozzle	Piezoelectric quartz	> 500 kHz
PT28	Discharge nozzle	Piezoelectric quartz	> 500 kHz
PT29	2 nd stage front ISR at d_2	Piezoresistive silicon	> 30 kHz
PT31	2 nd stage diffuser mid-pitch on the shroud at d_3	Piezoresistive silicon	> 30 kHz

pressure $\leq \pm 0.03\%$ and dynamic-pressure: PT27 = $\pm 0.9\%$, PT28 = $\pm 3.0\%$, PT29 = $\pm 0.4\%$ and PT31 = $\pm 0.4\%$.



Figure 2.3: Miniature pressure-pulsation sensors installed in the 2nd stage

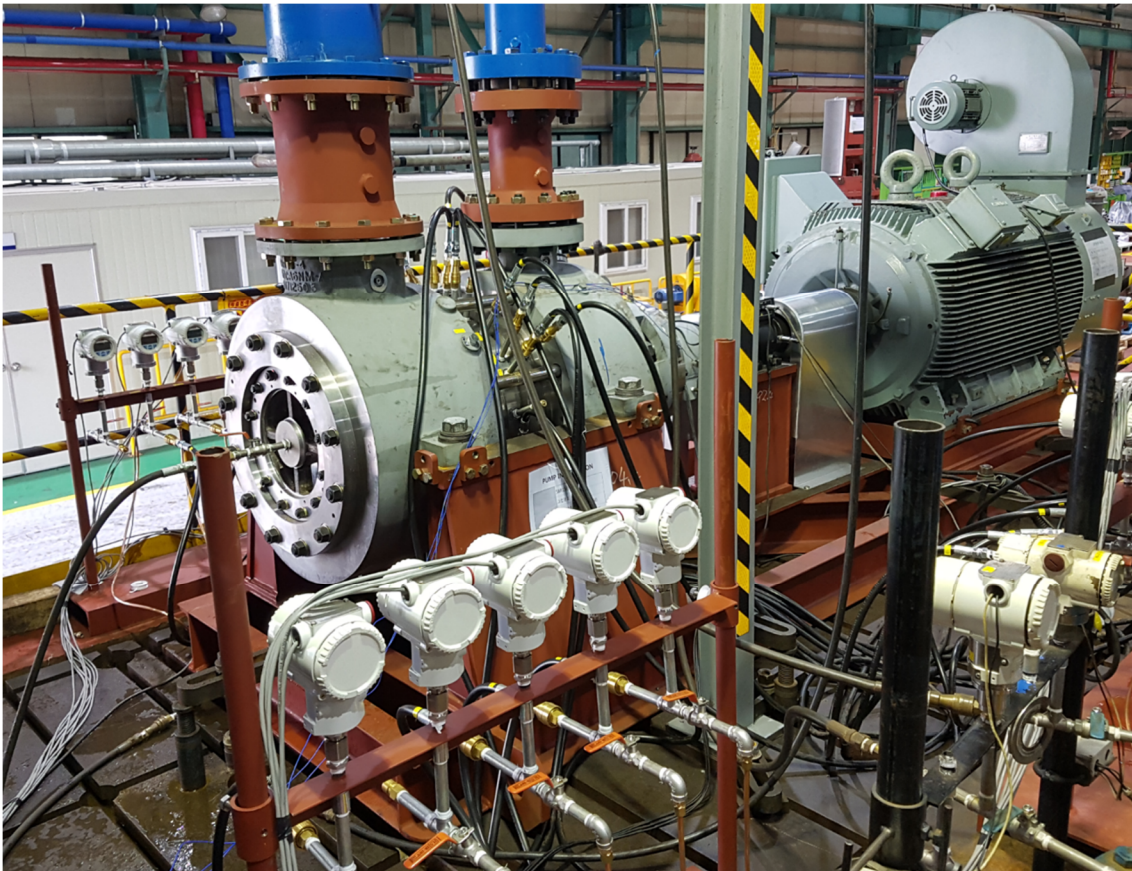


Figure 2.4: 4-stage model pump

2.2 Test Loop

A new test-loop was constructed for the maximum operating pressure of 16 bar,g at the suction piping and 100 bar,g at the discharge piping. Nominal diameters of the suction and discharge pipe were 200 mm and 150 mm, respectively. The test loop was a closed-type equipped with a pressurizer and heat exchanger [3]. The small pressurizer was connected to the suction pipe of main loop through a small by-pass pipe to control inlet pressure of the pump. The test liquid (=water) was circulated only inside the main loop and did not pass through the small pressurizer. A globe-type control valve was installed at a sufficient distance downstream of the discharge flange of the model pump. The pump was driven by an electric motor with an output power of 350 kW and the motor was controlled by a variable frequency converter.

The suction and discharge pressure were measured at $2D$ away from the pump flange. A ring manifold connecting four pressure taps on the pipe wall around the circumference was installed at each measuring section [59]. A torque meter of 2 kN equipped with an encoder was installed between the pump and motor shaft to measure the shaft power and rotational speed. An electromagnetic flow-meter was installed far downstream of the discharge control-valve for the flow-rate measurement in the main loop. Balance-drum leakage was measured with an electromagnetic flow-meter in a pipe returning the leakage back to the



Figure 2.5: Test loop

pump inlet. Water temperature in the test loop was measured in the suction pipe. Figure 2.5 shows the test loop and model pump before clamping them on the ground.

Reading-scale measurement uncertainties of the overall performances according to [59] were $Q = \pm 0.37\%$, $H = \pm 0.03\%$, $P = \pm 0.40\%$, $\eta = \pm 0.53\%$.

2.3 Reynolds Number Dependence of Head Curves

According to IEC60193 [60], Reynolds number for performance test of a model pump needs to be larger than 4×10^6 for a radial impeller to ensure a good hydraulic similarity between the model and prototype pump. The Reynolds number in IEC60193 is calculated as $Re_{IEC} = u_{1a}d_{1a}/\nu$ where d_{1a} is the impeller inlet diameter and u_{1a} is the inlet tip speed.

Reynolds number dependency of overall-head curves was investigated by varying rotational speed of the shaft of the manufactured model-pump. Figure 2.6 shows measured head-curves at four different Reynolds numbers. ψ and q_b^* are dimensionless head and flow-rate, respectively. Water temperature at each

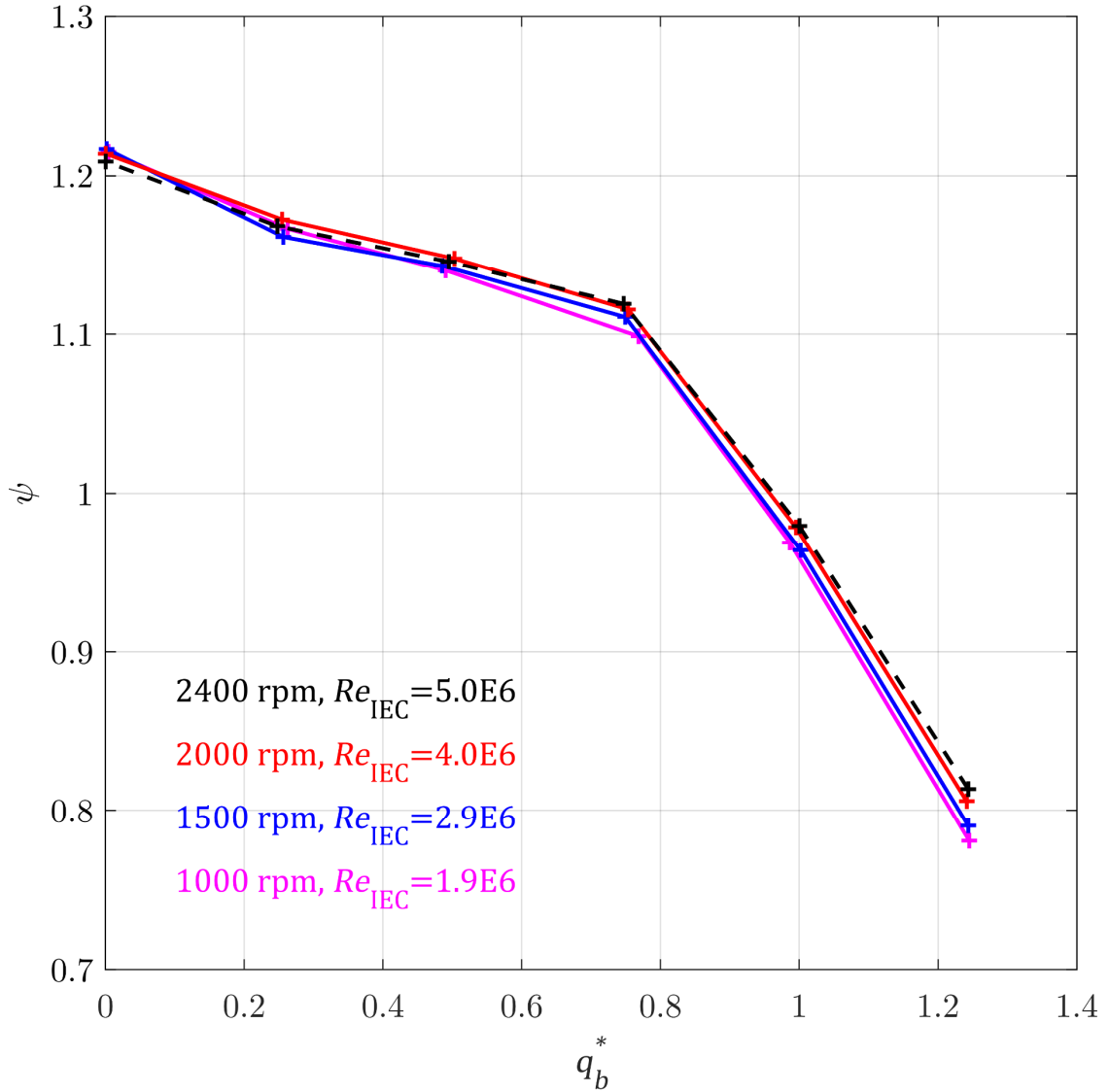


Figure 2.6: Overall-head curves at different Reynolds numbers

test was slightly different but in a range of $26 \sim 32$ °C. The shut-off head is almost identical in all Reynolds number. However, as the operating flow-rate increases, a lower Reynolds number tends to produce a lower head. The head at BEP is different by as much as 2.1% between $Re_{IEC} = 1.9 \times 10^6$ and 5.0×10^6 . The dynamic similarity tends to be satisfied when the Reynolds number is larger than 4.0×10^6 .

Therefore, all model-pump tests in the present study were carried out at 2400 rpm. At this rotational speed, the pump could run up to the maximum flow rate of $q_b^* = 1.5$ using the electric motor of 350 kW, which was sufficient for the purpose of the current project.

2.4 Influence of Test Loop on Pressure Pulsations

Various studies [3, 41, 57, 61] reported that pressure pulsations in a pump can be affected by the test loop. Sudden area-variations in piping system generate sound waves, which results in acoustic resonances at certain frequencies. Throttle valve installed in the test loop creates broadband pressure-pulsations since it dissipates energy of the fluid during the adjustment of operating flow-rate. If a booster pump is installed in front of the main pump to supply a required suction-pressure, pressure pulsations are also generated by the booster pump. These test-loop parameters interfere with the measurement output of pressure pulsations of the target pump.

The system influence can be roughly checked by comparing the overall RMS of dimensionless pressure-pulsations, Δp_{ove}^* according to (Gl. 4-22), at different rotational-speeds [3]. It is because pressure pulsations are approximately proportional to the square of the blade tip speed when the system influence is little or weak on the measurement output.

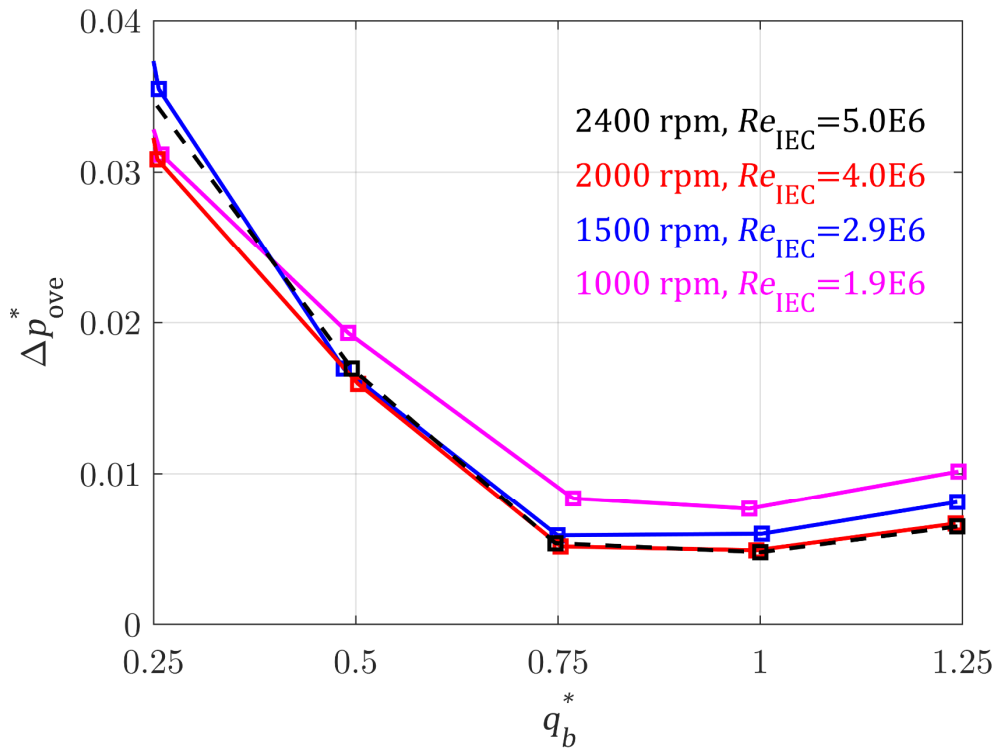


Figure 2.7: Overall RMS values of dimensionless pressure-pulsations at the discharge nozzle for various rotational-speeds

Figure 2.7 shows measured Δp_{ove}^* at the discharge nozzle of the 4-stage model pump at four different rotational-speeds. When the rotational speed is higher than 2000 rpm, Δp_{ove}^* at BEP tend to converge. It confirms the finding in Fig. 2.6 that the similarity laws are satisfied at $Re_{\text{IEC}} \geq 4 \times 10^6$ in the current project. The pressure pulsations at 2000 and 2400 rpm are almost identical for $q_b^* = 0.5 \sim 1.25$, indicating that the influence of the test loop on pressure pulsations is negligible in this flow-range. However, a distinct deviation is observed between them when the dimensionless flow-rate is smaller than 0.5.

Spectra of the pressure pulsations measured at 2400 rpm are analyzed for various flow-rates in Fig. 2.8. The left figure shows frequency range of $f/f_n = 0.0025 \sim 21$ and the right one $0.0025 \sim 3$. At $q_b^* = 1.0$ and 0.75 , a typical

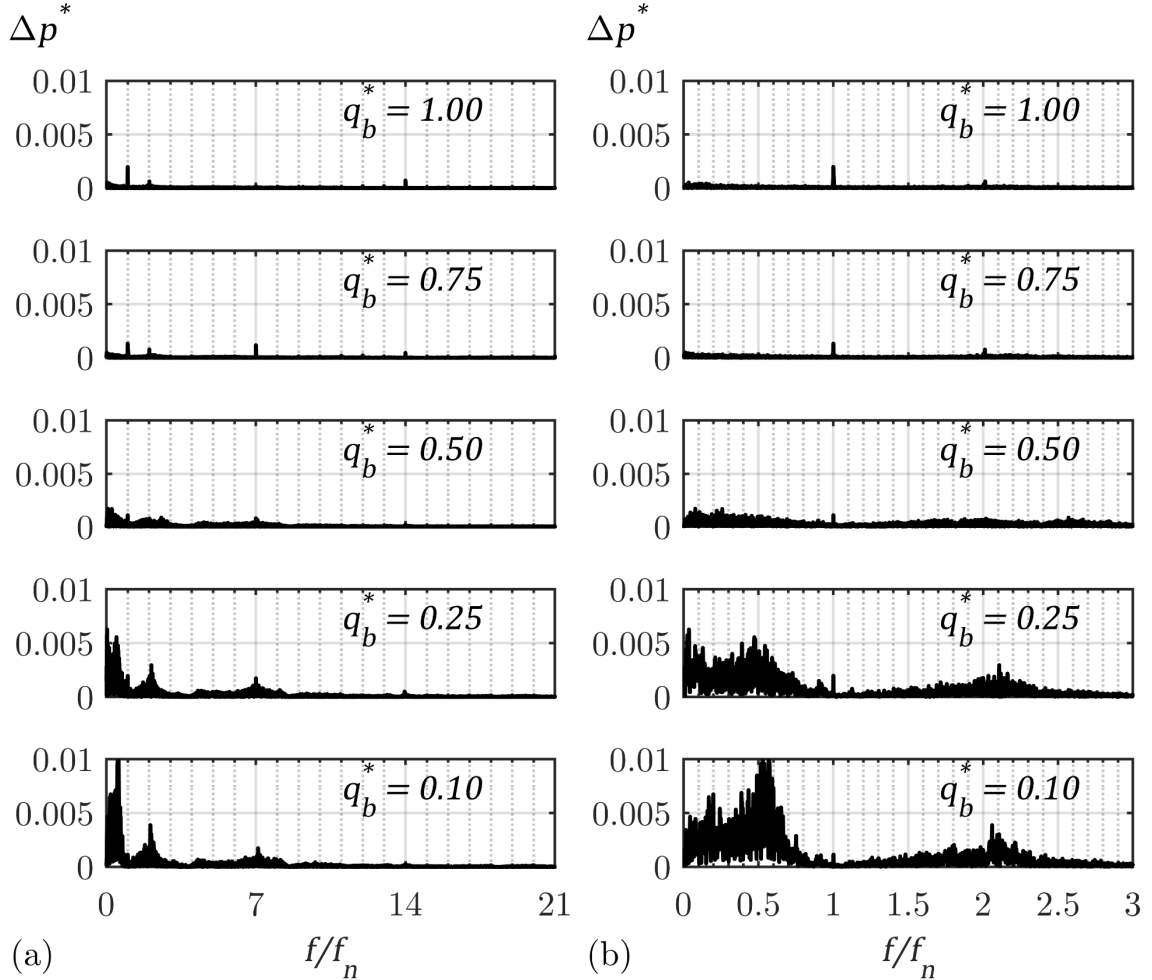


Figure 2.8: Spectra of dimensionless pressure-pulsations at the discharge nozzle for various flow-rates at $Re_{\text{IEC}} = 5 \times 10^6$ (ordinate = zero-peak amplitude): (a) $f/f_n = 0.0025 \sim 21$, (b) zoom-in: $f/f_n = 0.0025 \sim 3$

pattern of pressure-pulsation spectra is observed. Peaks appear at the rotational frequency, vane passing frequency and its super-harmonics. At $q_b^* = 0.50$, flow recirculation and turbulent structures of various scales create pressure pulsations in a broadband manner, which is common at part-load. However, at $q_b^* = 0.25$ and 0.1 , strong broadband-excitations are detected near $f/f_n = 0.5$ and 2.1 . The amplitude is many times higher than that at f_n or VPF. It is very unlikely that the model pump can generate such strong hydraulic-excitations at these non-synchronous frequency ranges. It implies that there is a strong interference of the test loop on the measured pressure-pulsations when the pump operates at $q_b^* < 0.50$. Presumably, a large throttling of the control valve at deep part-load creates strong flow separation and turbulence, resulting in the peculiar broadband pressure-pulsations. The true origin of the abnormal pressure-pulsations needs to be investigated in a future project. The current work analyzes the pressure pulsations only above $q_b^* = 0.5$.

3 Numerical Investigation Method

3.1 Governing Equations and Simulation Method

Governing Equations

CFD simulations were carried out to help the interpretation of test results by analyzing flow patterns. A commercial CFD software, ANSYS CFX version 17.2, was utilized for this purpose. Governing equations describing time-dependent incompressible-fluid motion are [62, 63]:

$$Gl. 3-1 \quad \frac{\partial c_i}{\partial x_i} = 0$$

$$Gl. 3-2 \quad \rho \left(\frac{\partial c_i}{\partial t} + c_j \frac{\partial c_i}{\partial x_j} \right) = - \frac{\partial p}{\partial x_i} + \frac{\partial \tau_{ij}}{\partial x_j} + f_i$$

where f_i is a body force term. In Newtonian fluid, the viscous shear stresses (τ_{ij}) are proportional to the dynamic viscosity and the strain rate as:

$$Gl. 3-3 \quad \tau_{ij} = \mu \left(\frac{\partial c_i}{\partial x_j} + \frac{\partial c_j}{\partial x_i} \right)$$

Then, incompressible Navier-Stokes equation for Newtonian fluid becomes:

$$Gl. 3-4 \quad \rho \left(\frac{\partial c_i}{\partial t} + c_j \frac{\partial c_i}{\partial x_j} \right) = - \frac{\partial p}{\partial x_i} + \mu \frac{\partial^2 c_i}{\partial x_j \partial x_j} + f_i$$

In turbomachinery applications, it is often convenient to use a rotating coordinate system rather than an absolute one. A position of a fluid particle in the absolute frame of reference (\vec{X}) can be expressed as $\vec{X} = \vec{x} + \vec{o}$ where \vec{x} is a

position of the fluid particle in the rotating frame of reference, and \vec{o} is a distance vector between origins of the two frames. Time differentiation of the position relation gives a velocity relation as:

$$Gl. 3-5 \quad \vec{c} = \vec{w} + \frac{d\vec{o}}{dt} + \vec{\omega} \times \vec{x}$$

where \vec{c} is the velocity vector in the absolute frame, \vec{w} is the velocity vector in the rotating frame, and $\vec{\omega}$ is the angular velocity vector of the rotating frame. Time differentiation of the velocity relation gives an acceleration relation as:

$$Gl. 3-6 \quad \frac{d\vec{c}}{dt} = \frac{d\vec{w}}{dt} + \frac{d^2\vec{o}}{dt^2} + \frac{d\vec{\omega}}{dt} \times \vec{x} + 2\vec{\omega} \times \vec{w} + \vec{\omega} \times (\vec{\omega} \times \vec{x})$$

In the current study, the acceleration of the rotating frame origin is zero and the rotational speed is constant. The remaining terms in the right side of (Gl. 3-6) are the acceleration of the relative velocity, Coriolis acceleration and the centripetal acceleration as:

$$Gl. 3-7 \quad \frac{d\vec{c}}{dt} = \frac{d\vec{w}}{dt} + 2\vec{\omega} \times \vec{w} + \vec{\omega} \times (\vec{\omega} \times \vec{x})$$

The thermodynamic properties and viscous stresses in (Gl. 3-4) are independent of the frame of reference. By arranging (Gl. 3-7) and (Gl. 3-4), Navier-Stokes equation in the rotating frame is obtained as:

$$Gl. 3-8 \quad \rho \left(\frac{\partial w_i}{\partial t} + w_j \frac{\partial w_i}{\partial x_j} \right) = -\frac{\partial p}{\partial x_i} + \mu \frac{\partial^2 w_i}{\partial x_j \partial x_j} + f_i + f_r$$

where $f_r = \rho(-2\vec{\omega} \times \vec{w} - \vec{\omega} \times (\vec{\omega} \times \vec{x}))$

Simulation Approach and Turbulence Model

If the governing equations are numerically solved using sufficiently fine meshes and small time-step that can resolve all relevant spatial and temporal

scales of turbulence structures in a flow field, an accurate prediction of flow motion is possible [64, 65]. This approach is called Direct-Numerical-Simulation (DNS). However, the spatial and temporal size of the smallest turbulent eddies decrease with increasing Reynolds number, which makes the computational cost for the DNS extremely high.

In many flow-fields, large-scale eddies that are mostly determined by the flow geometry are more significant than small-scale ones. If a numerical simulation explicitly computes large-scale motions and estimate the influence of small-scale eddies based on simple models, the computational cost can be significantly reduced. Large-Eddy-Simulation (LES) is such a method. In the LES approach, a spatial filter operator is applied to the Navier-Stokes equation to separate large and small-scale turbulent structures. The LES is less expensive than the DNS, but still challenging for flows with high Reynolds number due to a huge amount of grid points and calculation time-steps to resolve a thin boundary layer near the wall region [66].

Reynolds-averaged Navier-Stokes (RANS) is a popular simulation method in many engineering applications because the required memory-size and computation-time are feasible. In RANS (or URANS), the governing equations are averaged over a certain time-interval to decompose the unsteady flow variables into mean values (or ensemble-averaged values) and turbulent fluctuation values [67]:

$$Gl. 3-9 \quad \phi(t, x_i) = \bar{\phi}(t, x_i) + \phi'(t, x_i)$$

$$\text{where } \bar{\phi}(t, x_i) = \frac{1}{T} \int_{-\frac{T}{2}}^{\frac{T}{2}} \phi(t + \tau, x) d\tau$$

If the averaging time-interval (T) is longer than time-scale of small turbulent motions but sufficiently shorter than one of large motions, the time-dependent RANS approach may estimate some important flow-features. By applying (Gl. 3-9) into (Gl. 3-4), (U)RANS equations are obtained as:

$$Gl. 3-10 \quad \rho \left(\frac{\partial \bar{c}_i}{\partial t} + \bar{c}_j \frac{\partial \bar{c}_i}{\partial x_j} \right) = - \frac{\partial \bar{p}}{\partial x_i} + \mu \frac{\partial^2 \bar{c}_i}{\partial x_j \partial x_j} - \rho \frac{\partial \overline{c'_i c'_j}}{\partial x_j} + f_i$$

The mean values are explicitly solved and the influence of turbulent fluctuations is modelled by the terms $\overline{c'_i c'_j}$ that are called Reynolds stresses. A turbulence model is necessary to determine the Reynolds stresses, which is based on either the turbulent-viscosity hypothesis or modelled Reynolds-stress transport equations [65]. The turbulent-viscosity hypothesis (or Boussinesq hypothesis) describes the Reynolds stresses in a relation of turbulent kinetic energy (k) and a product of mean rate of strain and a turbulent-viscosity (or eddy-viscosity) (ν_T) as:

$$Gl. 3-11 \quad \overline{c'_i c'_j} = \frac{2}{3} k \delta_{ij} - \nu_T \left(\frac{\partial \bar{c}_i}{\partial x_j} + \frac{\partial \bar{c}_j}{\partial x_i} \right)$$

where δ_{ij} is Kronecker delta function, and the turbulent kinetic energy is defined as:

$$Gl. 3-12 \quad k = \frac{1}{2} \overline{c'_i c'_i}$$

There are various turbulence models based on the turbulent-viscosity hypothesis that are summarized below:

- **Algebraic model (or zero-equation model):** the turbulent-viscosity is determined from an algebraic equation, for example, as the product of a velocity-scale (c_s) and a length-scale (l_s): $\nu_T = c_s l_s$. It is the simplest turbulence-model but incomplete since c_s and l_s must be specified depending on each flow characteristic [65].
- **One-equation model:** Kolmogorov [68] and Prandtl [69] suggested to estimate the velocity-scale based on the turbulent kinetic energy as $c_s = c\sqrt{k}$ where c is a constant. Then, the turbulent-viscosity is determined as $\nu_T = c\sqrt{k}l_s$. A model transport equation must be solved to obtain k , i.e. one-equation model.
- **Two-equation model:** the turbulent-viscosity is calculated by two

turbulence quantities instead of the velocity-scale and length-scale that are dependent on each flow characteristic. For example, $k - \epsilon$ model solves two transport equations for the turbulent kinetic energy (k) and dissipation (ϵ) and determines the turbulence-viscosity as $\nu_T = c_\mu k^2/\epsilon$. The $k - \epsilon$ model usually yields an acceptable estimation for simple flows, but can be inaccurate for complex ones [65]. Another popular two-equation model is $k - \omega$ model suggested by Wilcox [70]. It solves transport equations for k and turbulent-frequency (ω). The turbulent-viscosity is calculated as $\nu_T = k/\omega$. This model is known to be accurate in the viscous sub-layer, but unsatisfactory in non-turbulent free-stream boundaries [65]. Menter [71, 72] suggested shear-stress transport (SST) by combining strengths of the $k - \epsilon$ and $k - \omega$ model. A blending function F_1 is introduced in the SST model in order that the $k - \omega$ model is applied in the near-wall region ($F_1 = 1$) and the $k - \epsilon$ model in the free stream ($F_1 = 0$). The turbulent-viscosity is determined as $\nu_T = a_1 k / \max(a_1 \omega, \Omega F_2)$. Here, F_2 is another blending function to suppress over-prediction of turbulent shear stress in an adverse pressure-gradient boundary-layer as $F_2 = 1$ for boundary-layer flows, and $F_2 = 0$ for free shear layers. The SST model equations are as below [72]:

$$Gl. 3-13 \quad \frac{\partial \rho k}{\partial t} + \bar{c}_j \frac{\partial \rho k}{\partial x_j} = \tau_{ij} \frac{\partial \bar{c}_i}{\partial x_j} - \beta^* \rho \omega k + \frac{\partial}{\partial x_j} \left[(\mu + \sigma_k \mu_t) \frac{\partial k}{\partial x_j} \right]$$

$$Gl. 3-14 \quad \begin{aligned} \frac{\partial \rho \omega}{\partial t} + \bar{c}_j \frac{\partial \rho \omega}{\partial x_j} = & \frac{\gamma}{\nu_t} \tau_{ij} \frac{\partial \bar{c}_i}{\partial x_j} - \beta \rho \omega^2 + \frac{\partial}{\partial x_j} \left[(\mu + \sigma_\omega \mu_t) \frac{\partial \omega}{\partial x_j} \right] \\ & + 2\rho(1 - F_1)\sigma_{\omega 2} \frac{1}{\omega} \frac{\partial k}{\partial x_j} \frac{\partial \omega}{\partial x_j} \end{aligned}$$

$$Gl. 3-15 \quad \phi = F_1 \phi_1 + (1 - F_1) \phi_2$$

Here, ϕ_1 is any constant for the $k - \omega$ model, ϕ_2 for the $k - \epsilon$ model, and ϕ the corresponding constant for (Gl. 3-13, 3-14). The constants in (Gl. 3-13, 3-14, 3-15) are as below:

$$F_1 = \tanh(\arg_1^4), \quad \arg_1 = \min \left(\max \left(\frac{\sqrt{k}}{0.09\omega y}, \frac{500\nu}{y^2\omega} \right), \frac{4\rho\sigma_{\omega 2}k}{CD_{k\omega}y^2} \right)$$

$$CD_{k\omega} = \max \left(2\rho\sigma_{\omega 2} \frac{1}{\omega} \frac{\partial k}{\partial x_j} \frac{\partial \omega}{\partial x_j}, 10^{-20} \right), \quad \nu_T = \frac{a_1 k}{\max(a_1\omega, \Omega F_2)}$$

$$\phi_1: \sigma_{k1} = 0.85, \quad \sigma_{\omega 1} = 0.5, \quad \beta_1 = 0.075, \quad a_1 = 0.31, \quad \beta^* = 0.09, \quad \kappa = 0.41,$$

$$\gamma_1 = \frac{\beta_1}{\beta^*} - \frac{\sigma_{\omega 1}\kappa^2}{\sqrt{\beta^*}}$$

$$\phi_2: \sigma_{k2} = 1.0, \quad \sigma_{\omega 2} = 0.856, \quad \beta_2 = 0.0828, \quad \gamma_2 = \frac{\beta_2}{\beta^*} - \frac{\sigma_{\omega 2}\kappa^2}{\sqrt{\beta^*}}$$

$$F_2 = \tanh(\arg_2^2), \quad \arg_2 = \max \left(\frac{2\sqrt{k}}{0.09\omega y}, \frac{500\nu}{y^2\omega} \right)$$

Ω = absolute value of the vorticity

URANS with the SST turbulence model has been used for many applications, for example [24, 73–76]. However, Menter and Egrov [77] reported that the SST model has a limitation in accuracy of capturing small-scale turbulent motions even though the spatial and temporal resolution of a numerical simulation is sufficient. It is because the SST model usually over-estimates the turbulent-viscosity, which prevents the break-up of turbulent structures from large to small scales. Menter *et al* [78] suggested a new simulation method, called Scale-Adaptive-Simulation (SAS). A destruction term for the turbulent-viscosity is introduced into an existing turbulent transport equation, which makes the prediction of small-scale eddies possible in URANS. The SAS method was integrated into the ω – equation of the SST model [77], which was named as SAS-SST model [79]. Figure 3.1 shows an example of broadband turbulent eddies predicted by the SAS-SST model [77, 80]. The SAS-SST equations are given in (Gl. 3-16, 3-17) [81, 82]. Here, Q_{SAS} term in the ω – equation (Gl. 3-17) plays a

role to increase ω for unsteady flow regions, which results in a reduction of the turbulent-viscosity [83]:

$$Gl. 3-16 \quad \frac{\partial \rho k}{\partial t} + \bar{c}_j \frac{\partial \rho k}{\partial x_j} = P_k - \rho c_\mu k \omega + \frac{\partial}{\partial x_j} \left[\left(\mu + \frac{\mu_t}{\sigma_k} \right) \frac{\partial k}{\partial x_j} \right]$$

$$Gl. 3-17 \quad \begin{aligned} \frac{\partial \rho \omega}{\partial t} + \bar{c}_j \frac{\partial \rho \omega}{\partial x_j} = & \alpha \frac{\omega}{k} P_k - \beta \rho \omega^2 + Q_{SAS} + \frac{\partial}{\partial x_j} \left[\left(\mu + \frac{\mu_t}{\sigma_\omega} \right) \frac{\partial \omega}{\partial x_j} \right] \\ & + (1 - F_1) \frac{2\rho}{\sigma_{\omega 2}} \frac{1}{\omega} \frac{\partial k}{\partial x_j} \frac{\partial \omega}{\partial x_j} \end{aligned}$$

where

$$Q_{SAS} = \max \left[\rho \zeta_2 \kappa S^2 \left(\frac{L}{L_{vK}} \right)^2 - c \frac{2\rho k}{\sigma_\Phi} \max \left(\frac{1}{\omega^2} \frac{\partial \omega}{\partial x_j} \frac{\partial \omega}{\partial x_j}, \frac{1}{k^2} \frac{\partial k}{\partial x_j} \frac{\partial k}{\partial x_j} \right), 0 \right],$$

$$\sigma_{\omega 2} = 0.856, \quad \zeta_2 = 3.51, \quad \sigma_\Phi = \frac{2}{3}, \quad c = 2, \quad \kappa = 0.41, \quad c_\mu = 0.09,$$

$$L = \frac{\sqrt{k}}{c_\mu^{1/4}} \omega, \quad L_{vK} = \frac{\kappa S}{|c''|},$$

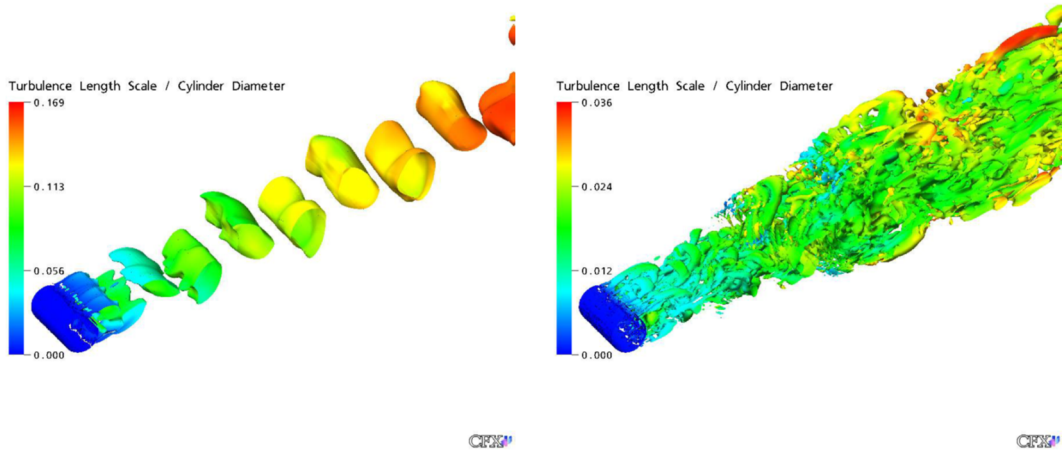


Figure 3.1: Comparison of predicted flow-fields past a circular cylinder: Left – URANS with SST model, Right – SAS-SST [77, 80]

$$c'' = \sqrt{\frac{\partial^2 \bar{c}_i}{\partial x_k^2} \frac{\partial^2 \bar{c}_i}{\partial x_j^2}}, \quad S = \sqrt{2S_{ij}S_{ij}}, \quad S_{ij} = \frac{1}{2} \left(\frac{\partial \bar{c}_i}{\partial x_j} + \frac{\partial \bar{c}_j}{\partial x_i} \right), \quad P_k = \mu_t S^2$$

Various test simulations based on the SAS-SST model were presented in [80, 81]. In pump applications, the SAS-SST model was used to estimate performance curves over the whole operating flow-range at $n_q = 36$ [84] and head-curve instabilities and cavitation performances at $n_q = 95$ [85]. Lucius and Brenner [86] reported that the SAS-SST model was superior to capture small-scale turbulent structures in flow fields of an impeller than the SST model. Ennouri *et al* [87] compared pressure-pulsations estimated by CFD simulations based on the SAS-SST model to measured values in a volute pump. A decent agreement was observed when the sampling point of the pressure pulsations was located on the volute spiral-casing. The SAS-SST model is adopted in the present work for unsteady CFD simulations.

Boundary Layer Treatment

The no-slip boundary condition on a solid surface generates a steep velocity-gradient in the near-wall region. Since boundary-layer thickness decreases with increasing Reynolds number, flows with high Reynolds number often require very fine grids to resolve the velocity profile near the wall.

Lauder and Spalding [88] suggested a numerical method to handle the boundary layer, called *wall-function*. This approach locates the first near-wall grid-point at some distance away from the wall, and estimates its velocity boundary condition based on the log-law relation: $c^+ = 1/\kappa \ln(y^+) + B$. Since the velocity profile below the first node is not explicitly computed, the number of grid points in the boundary layer is significantly reduced. The wall-function has been widely used in many industrial applications. However, for flows under a strong pressure-gradient or separation, this method is known to be inaccurate [65, 70].

If computational resources are sufficient, the velocity distribution in the boundary layer may be directly solved with a large number of mesh nodes. However, in the $k - \epsilon$ model, a higher mesh resolution does not always

guarantee a better accuracy. In the viscous sub-layer, the viscous shear-stress dominates the total stress and the Reynolds stresses are negligible [64]. The $k - \epsilon$ model often over-estimates the turbulent-viscosity ($\nu_T = C_\mu k^2/\epsilon$) because the constant coefficient C_μ is too large for the near-wall region. Various modifications were suggested, e.g. an introduction of a damping function f_μ in a form of $\nu_T = f_\mu C_\mu k^2/\epsilon$ [89]. However, the damping function is dependent on each flow type, and its applicability is limited only for a certain range of specifications [65]. Wilcox [70] proposed an analytic solution for the viscous sub-layer in the $\omega -$ equation, called *$k - \omega$ based low-Re model*. This method does not require an arbitrary damping function, and thus usually yields an accurate prediction of the near-wall velocity profile as long as the mesh resolution is sufficiently fine ($y^+ < 2.5$). The $k - \omega$ based low-Re model was slightly modified by Menter [71] in his SST model as (Gl. 3-18):

$$Gl. 3-18 \quad \omega_{\text{Wilcox}} \sim \frac{6\nu}{\beta_1 y^2} \quad \rightarrow \quad \omega_{\text{Menter}} = 10 \frac{6\nu}{\beta_1 (\Delta y)^2}$$

where $\beta_1 = 0.075$, Δy = the distance to the next grid-point away from the wall

Later, Menter [90, 91] suggested *automatic near-wall treatment*. It blends the wall-function and $k - \omega$ based low-Re model depending on a local near-wall mesh quality. If a local mesh resolution is sufficiently fine, the velocity profile in the boundary layer is directly computed using the $k - \omega$ based low-Re model. For a coarse mesh, the wall-function is activated. The automatic blending of two near-wall models is achieved as (Gl. 3-19, 3-20, 3-21) [82, 90]. The present study adopts the automatic near-wall treatment for the boundary-layer calculation.

$$Gl. 3-19 \quad \omega_{\text{blended}} = \sqrt{\omega_{\text{vis}}^2 + \omega_{\text{log-law}}^2}$$

$$\text{where } \omega_{\text{vis}} = \frac{6\nu}{\beta_1 (\Delta y)^2}, \quad \omega_{\text{log-law}} = \frac{c^*}{0.3\kappa\Delta y},$$

$$c^* = \left(\left(\sqrt{\nu \left| \frac{c}{\Delta y} \right|} \right)^4 + (\sqrt{a_1 k})^4 \right)^{0.25}, \quad a_1 = \frac{5}{9}, \quad B = 5.2, \quad \kappa = 0.41$$

Gl. 3-20 $F_c = -\rho c_\tau c^*$: flux for the momentum equation

Gl. 3-21 $F_k = 0$: flux for the k – equation

where $c_\tau = (c_{\tau,\text{vis}}^4 + c_{\tau,\text{log-law}}^4)^{0.25}$, $c_{\tau,\text{vis}} = \sqrt{\nu \left| \frac{c}{\Delta y} \right|}$, $c_{\tau,\text{log-law}} = \frac{c}{\frac{1}{\kappa} \ln(y^+) + B}$

Numerical Discretization Method

ANSYS CFX discretizes the governing equations using a finite-element based finite-volume method [82]. The governing equations in the conservation form are as follows [92]:

Gl. 3-22 $\int_S c_i n_i dA = 0$

Gl. 3-23
$$\begin{aligned} & \frac{\partial}{\partial t} \int_V \rho c_i dV + \int_S \rho c_i c_j n_j dA \\ & = - \int_S p \delta_{ij} n_j dA + \int_S \mu \left(\frac{\partial c_i}{\partial x_j} + \frac{\partial c_j}{\partial x_i} \right) \delta_{ij} n_j dA + \int_V f_i dV \end{aligned}$$

where V and S indicate volume and surface integral, respectively.

A 2D schematic drawing for the spatial discretization is depicted in Fig. 3.2 [82]. The simulation domain is spatially divided into a large number of mesh elements (left in Fig. 3.2), and each mesh element into a small number of sectors (right in Fig. 3.2). Vertices of the mesh elements are called mesh nodes that store flow-field solutions such as velocities and pressure. Integration points are

defined at each surface center of adjacent sectors. Control volumes are constructed around each mesh node using surrounding sectors.

The volume integrals are discretized within each sector and then accumulated to the control volume to which the sector belongs. The surface integrals are discretized at the integration points. The present study treats the advection term in (Gl. 3-23) with *high resolution scheme* [82]. This method is a blending of 1st and 2nd order upwind scheme. It determines a blending factor β at each node and tries to make it as close to 1 as possible depending on the numerical stability of local solution where $\beta = 0$ for 1st order and $\beta = 1$ for 2nd order upwind scheme [74, 82]. The temporal discretization is carried out with the 2nd order backward Euler scheme that is robust and stable regardless of the selection of calculation time step [93].

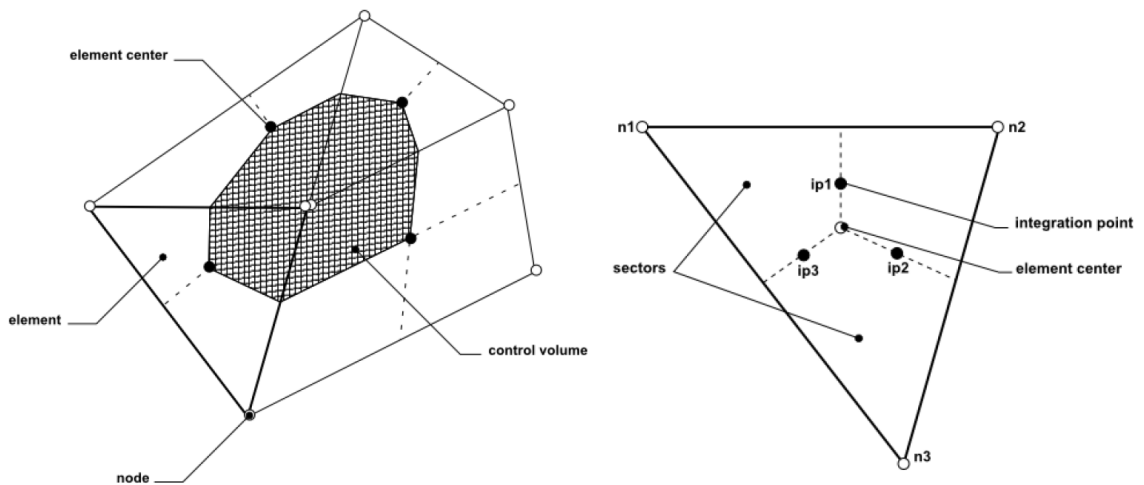


Figure 3.2: Schematic drawing of spatial discretization in ANSYS CFX [82]

3.2 Near-wall Mesh Dependency Study

The influence of near-wall mesh quality on the prediction accuracy of CFD simulations was investigated. Since the project model pump with 4-stage was too large for this purpose, a single-stage model pump having the same impeller and diffuser was designed. The computation domain consisted of an impeller with one blade, a diffuser with 12 guide-vanes and return-vanes, a straight suction pipe and a simple conical-discharge pipe as shown in Fig. 3.3. Annular seals and shroud and hub plates of the impeller are not included in the computation domain. The Reynolds number was identical with that of the 4-stage model pump as $Re = r_2 u_2 / \nu = 6.3 \times 10^6$. The inlet boundary condition was specified as the mass flow rate with 5% turbulence and outlet boundary condition as the average static pressure. Each impeller rotation was computed during 360 calculation time-steps ($=1^\circ$ rotation/calculation time-step). After five impeller-rotations, the head and efficiency reached quasi-periodic status. The analysis data was collected at 6th and 7th rotation.

The mesh dependency study was carried out by varying y^+ of hydraulic surfaces in the impeller from the viscous sub-layer to log-law region. Table 3.1 presents the total number of mesh nodes in the impeller and achieved average y^+ at BEP for each simulation case. The grid expansion ratio in the wall-normal direction was limited below 1.3. Some efforts were made to maintain mesh sizes of mean-flow passages in a similar level while the near-wall mesh resolution varied. Figure 3.4 depicts velocity profiles and mesh shapes near the impeller leading edge at different y^+ . The grid density in the boundary layer is clearly different between $y^+ = 48.5$ and 2.0, but mesh sizes in the mean-flow passages are similar. At $y^+ = 48.5$, the velocity boundary condition at the first grid-point is specified by the log-law relation and velocity profile below it is not estimated

Table 3.1: Near-wall mesh dependency study

Case	I	II	III	IV	V
Total number of mesh nodes in the impeller [$\times 10^6$]	1.9	2.0	2.3	2.6	2.9
Achieved average y^+ at BEP	48.5	24.7	9.0	4.0	2.0

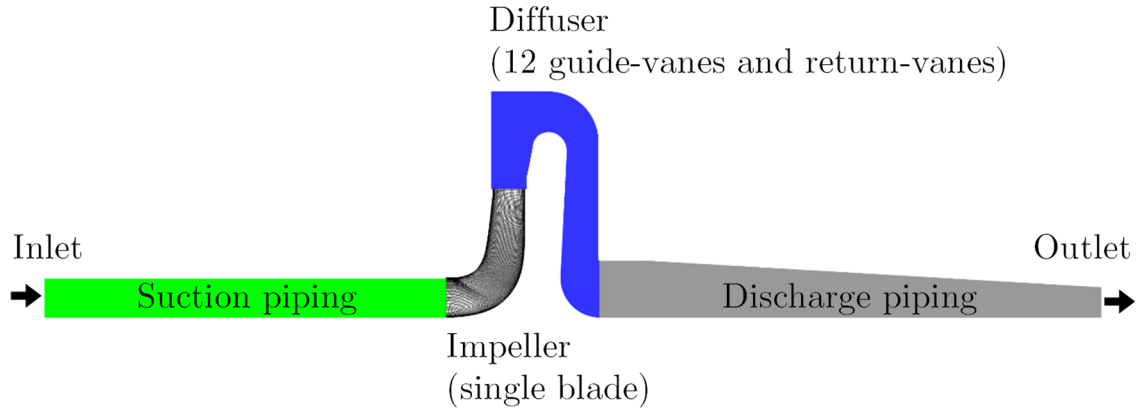


Figure 3.3: Computation domain of the single-stage pump for the near-wall mesh dependency study

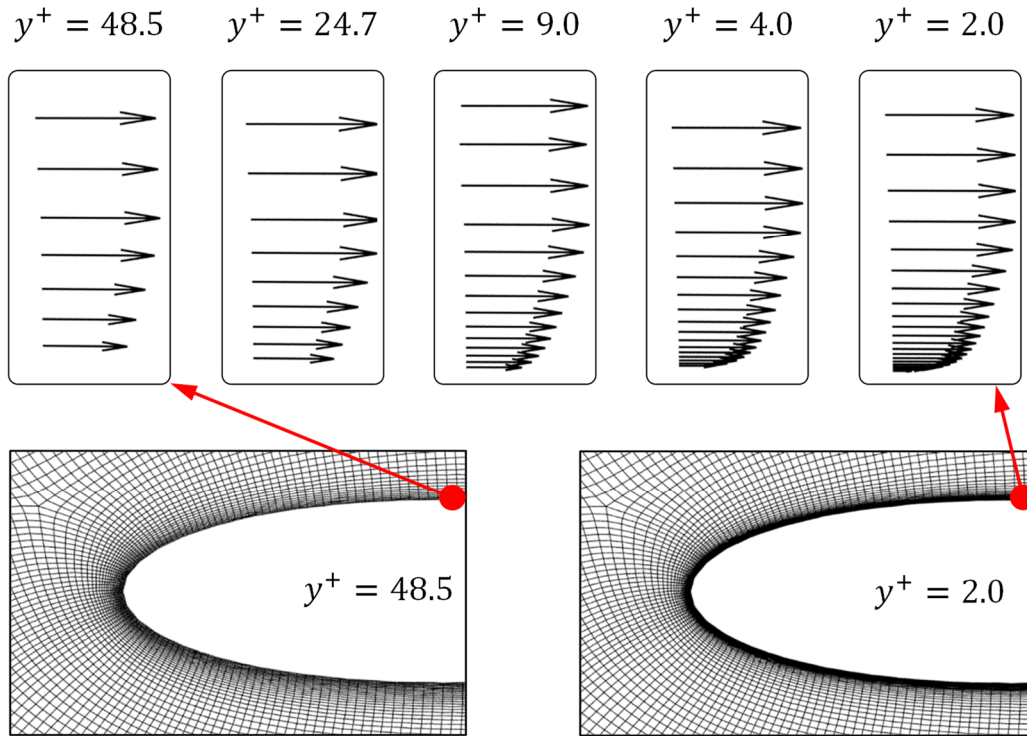


Figure 3.4: Top – predicted velocity-profiles in the boundary layer depending on y^+ , Bottom – mesh shapes around the impeller leading edge at $y^+ = 48.5$ and 2.0 ($q_b^* = 1.0$)

by the numerical simulation. When the first node lies in the viscous sub-layer ($y^+ < 5$), the boundary-layer solution is directly computed by the $k - \omega$ based low-Re model, and thus the steep velocity-gradient is predicted. At $y^+ = 24.7$ and 9.0, part of the near-wall velocity distribution is estimated by the blending of the wall-function and $k - \omega$ based low-Re model.

Figure 3.5 shows predicted pump-performances at different y^+ . ψ_{ove} , ψ_{La} , λ , and η_{La} indicate the dimensionless pump-head, impeller-head, power and impeller-hydraulic efficiency, respectively. The abscissa is y^+ , and the ordinate is a percentage deviation of a predicted performance at each simulation compared to that at $y^+ = 2$. A higher head and power is estimated with decreasing y^+ in an almost monotonic manner. The prediction deviation between $y^+ = 48.5$ and 2.0 are more than 2% for the head and power. The impeller efficiency is marginally affected by the near-wall mesh quality.

Span-wise velocity distribution at the impeller outlet are depicted in Fig. 3.6. The velocity components were time-averaged during the last two revolutions of the impeller, and circumferentially area-averaged at each span position. The meridional velocity was non-dimensionalized by u_2 , and the circumferential

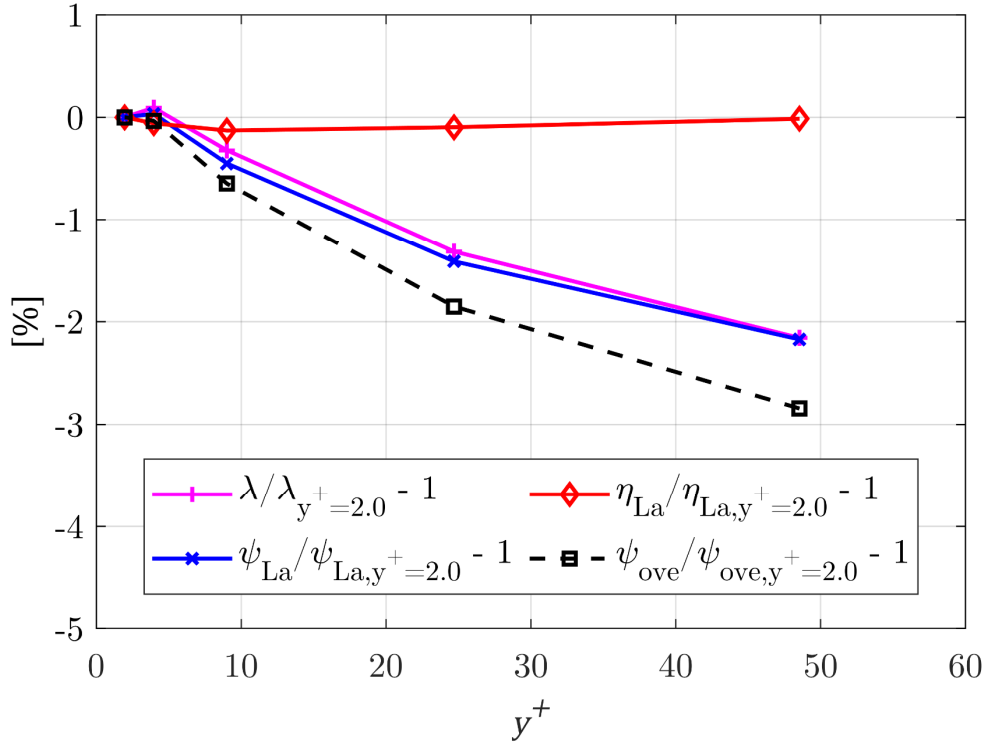


Figure 3.5: Variation of pump performances depending on y^+ ($q_b^* = 1.0$)

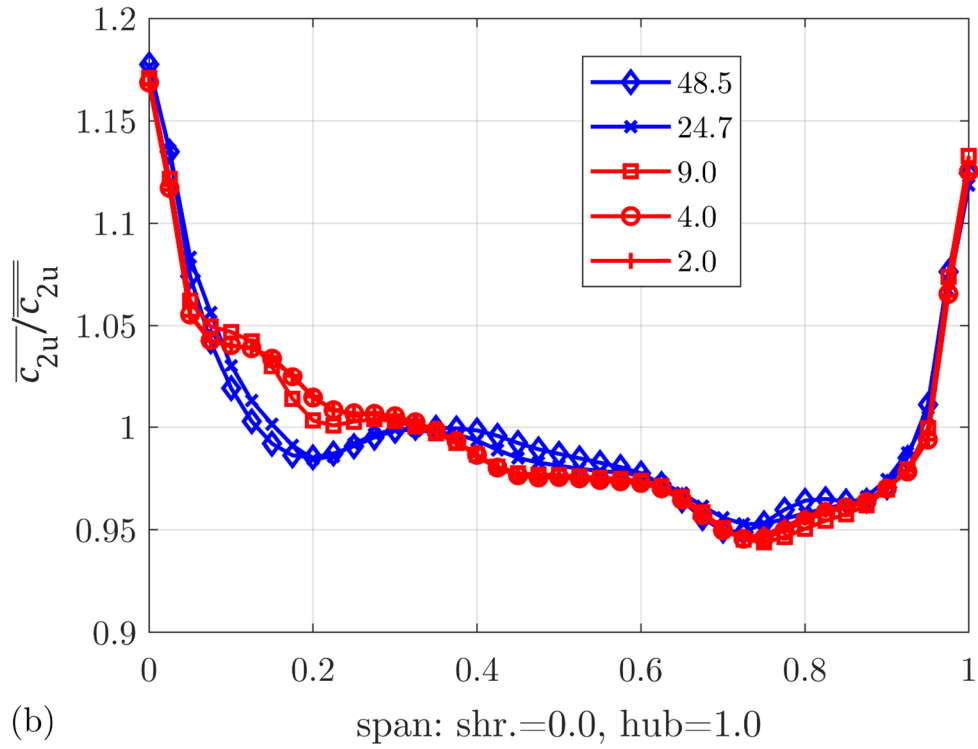
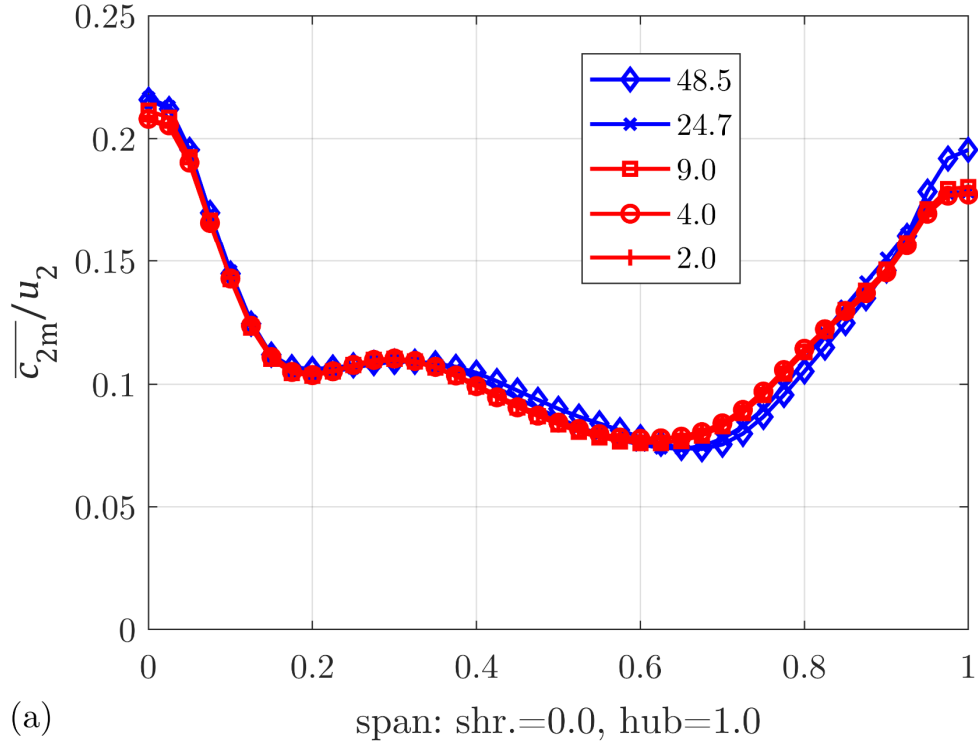


Figure 3.6: Span-wise distribution of dimensionless meridional and circumferential-velocity components at the impeller outlet for different y^+ ($q_b^* = 1.0$)

velocity by a spatial average over the width ($\overline{c_{2u}} = 1/b_2 \int_0^{b_2} \overline{c_{2u}} db$). The near-wall mesh quality generates little differences in the meridional-velocity distribution except the near-wall region. A slight deviation is observed in the circumferential-velocity profile depending on y^+ .

When the operating flow-rate is reduced to $q_b^* = 0.75$, the impact of y^+ on predicted pump-performances and velocity-distributions increases. The head and power deviation between $y^+ = 41.5$ and 1.7 are more than 2.5% in Fig. 3.7. The different y^+ produces some quantitative deviations in outlet-velocity profiles in Fig. 3.8, but the overall shape of the meridional-velocity distribution are still qualitatively similar. It is noticeable that the velocity profiles tend to converge when y^+ is below 10 (except the near-wall region). Figure 3.9 shows relative-velocity contours near the impeller leading edge at $y^+ = 41.5$ (top) and 1.7 (bottom). An increased incidence-angle at the reduced flow-rate causes flow-separation (=blue color) on the suction side of the blade inlet. The size of the predicted separation is different between $y^+ = 41.5$ and 1.7. The $k - \omega$ based low-Re model ($y^+ = 1.7$) estimates a thin and long separation along the blade, but the wall-function ($y^+ = 41.5$) a blunt and short one. As explained in the

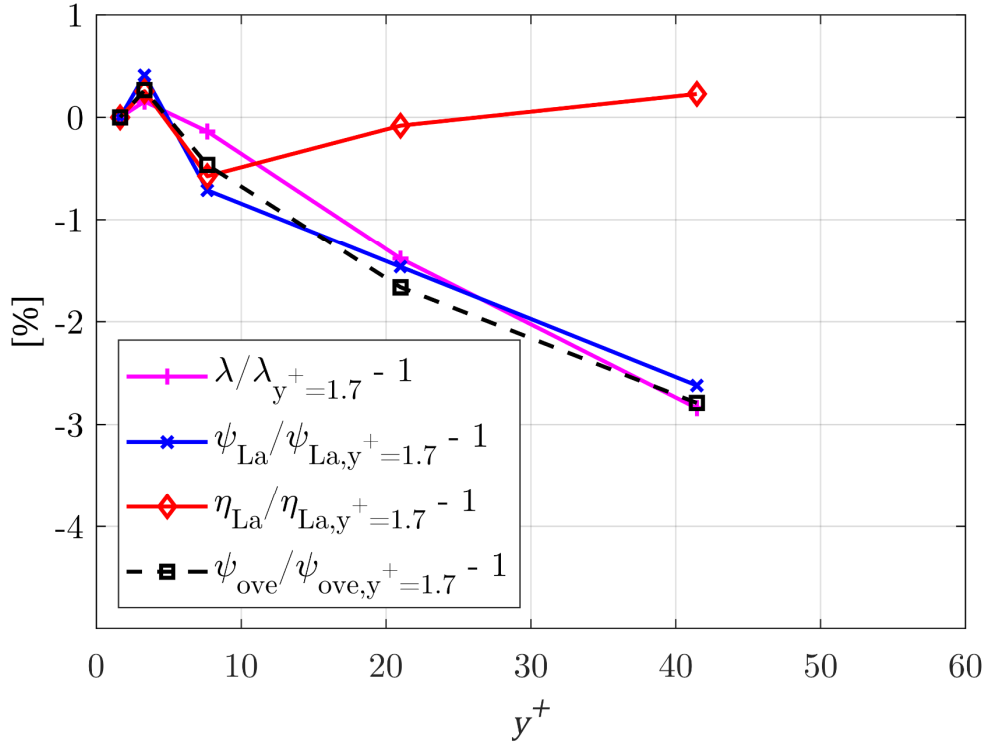


Figure 3.7: Variation of pump performances depending on y^+ ($q_b^* = 0.75$)

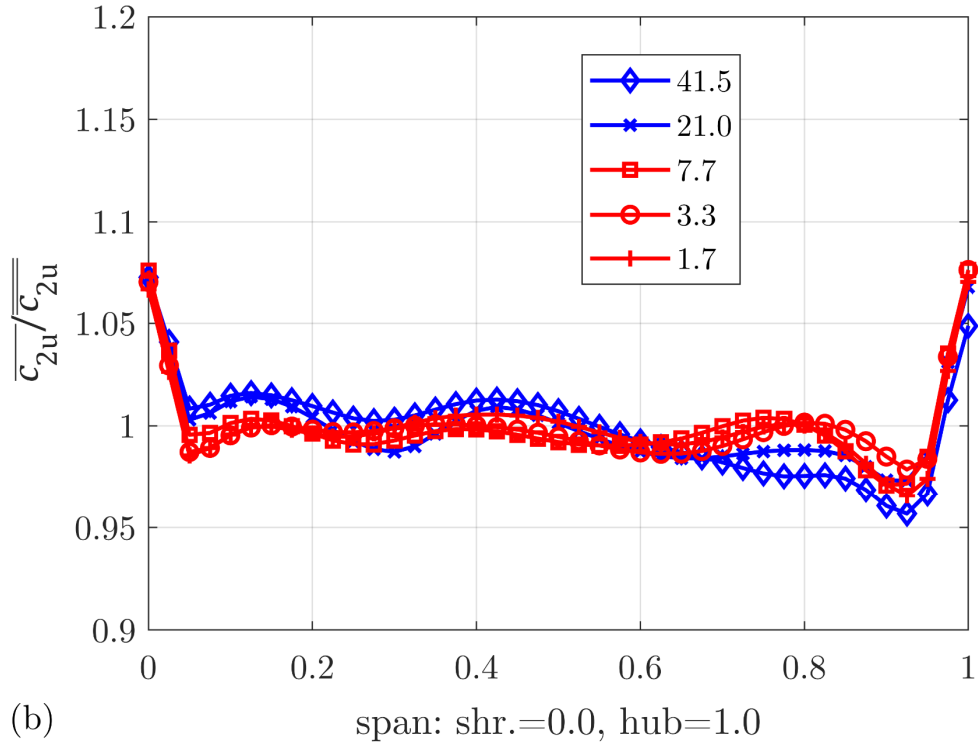
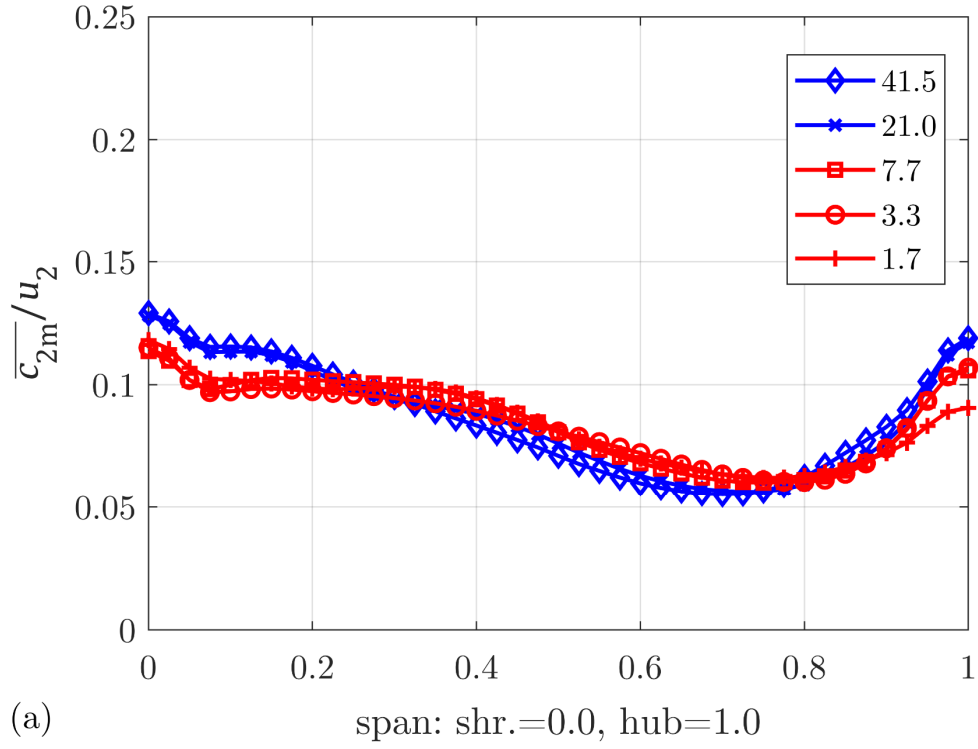


Figure 3.8: Span-wise distribution of dimensionless meridional and circumferential-velocity components at the impeller outlet for different y^+ ($q_b^* = 0.75$)

previous chapter, the $k - \omega$ based low-Re model is known to give a more accurate solution for boundary-layer flows under strong pressure-gradient or separation than the wall-function. Then, Figs. 3.5 ~ 3.9 suggest that it is recommendable to locate the first grid-points in the viscous sub-layer for numerical simulations for the 4-stage model pump to improve the solution accuracy in the current project.

However, the available computational resources could not meet such a requirement. Computational domain of the 4-stage model pump includes all hydraulic passages from the suction casing to the discharge casing. The required total number of grid points to achieve $y^+ < 5$ for the whole flow-passage easily exceed 300 million. Despite the importance of near-wall mesh quality, the first near-wall nodes could not be placed in the viscous sub-layer.

Then, how can the current simulation results be used to investigate flow patterns in the model pump? The author carried out the CFD simulations *after* experimental measurements were finished. Therefore, it was possible to compare predicted and measured performances. Some important common features were found that:

- (1) The head-curve instability was observed in both measurements and CFD

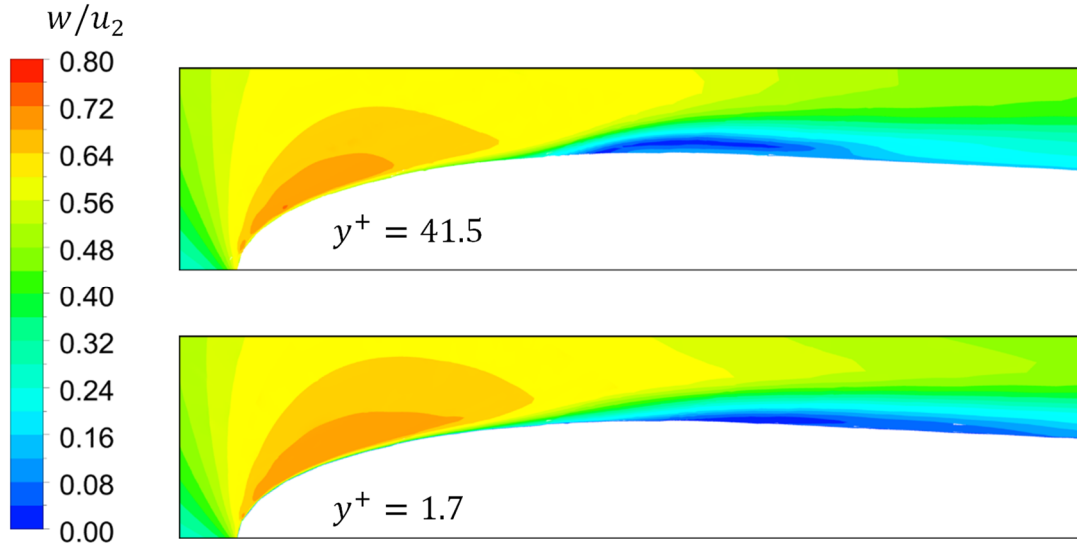


Figure 3.9: Dimensionless relative-velocity contours on the suction side of the impeller blade leading edge; span-position is near hub (span = 0.95) ($q_b^* = 0.75$)

simulations even though its onset flow-rate was slightly different.

- (2) A sudden change of the pressure distribution in the impeller side room was observed in both of them when the pump operated near the onset of the instability.

As will be explained in Chapter 5 and 6, the cause of a sudden variation of pressure profile in the ISR is closely related to a change of flow patterns at the impeller outlet. Since both the numerical simulation and experiment show the head-curve instability and a similar trend of pressure variation in the ISR, the current CFD method presumably can estimate some major flow-behaviors linked to the instability. Moreover, Figs. 3.6 and 3.8 show that a qualitative analysis of flow patterns is likely to be possible even with an insufficient near-wall mesh quality. However, it is obvious that the absolute accuracy in the current CFD simulations is not satisfactory.

3.3 Numerical Setup

The computational domain of the 4-stage model pump includes a suction casing, a suction impeller with 7 blades, three series-impellers with 7 blades, three series-diffusers with 12 guide-vanes and return-vanes, a last diffuser with 12 vanes, a discharge casing, a balance drum, all ISRs with annular seals as shown in Fig. 3.10. The hydraulic geometry in the simulation domain is almost identical to that of the constructed model pump except: (1) a smaller radial clearance of all annular seals because the seal pattern and surface roughness are not taken into account in the numerical simulation, and (2) a simplified leakage outlet piping of the balance drum instead of returning it back to the suction nozzle. Leakage flow-rate at the balance drum outlet was compared between the CFD result and measurement, and the difference was less than $\pm 4\%$ for $q_b^* = 0.5 \sim 1.0$. It implies that the flow rate through the impeller, diffuser and ISRs of the numerical simulation approximately matches that of the experiment.

Hexahedral meshes were applied for the impeller, diffuser, ISR, annular seal and balance drum. Tetrahedral meshes with prism layer near the wall were used to the suction and discharge casing. ANSYS Turbogrid and ICEM software were utilized for the mesh generation. The total number of grid nodes for the whole

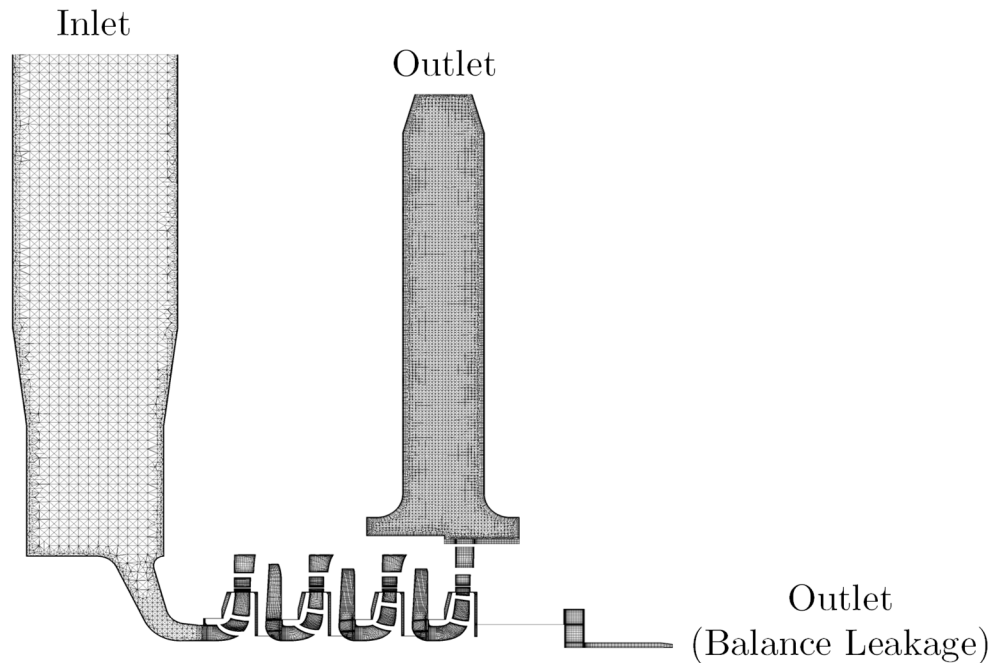


Figure 3.10: Computational domain for the 4-stage model pump

domain should not exceed 30 million considering the computational capacity. Therefore, the average y^+ of hydraulic surfaces for the impeller and diffuser were selected as 25 and 73, respectively. The mesh expansion ratio in the wall normal direction was limited below 1.3. Figure 3.11 shows the influence of mesh quality in the mean-flow passages on performances of the single-stage model pump used in Chapter 3.2. Some efforts were made to adjust mesh resolution in the mean-flow passages with maintaining the near-wall mesh quality at $y^+ = 24.7$. The abscissa indicates the total number of grid points in one blade passage of the impeller and the ordinate is a percentage deviation of a predicted performance at each simulation compared to that at the finest mesh. (The “fine+” mesh was used in Chapter 3.2.) When the mesh quality of the mean-flow passages is better than the “medium”, the estimated pump-performances deviate less than 0.25% compared to the “fine+”. Therefore, the “medium” mesh resolution was adopted for simulations of the 4-stage model pump. The number of grid points in the computational domains is summarized in Table 3.2.

Inlet boundary condition was specified as the static pressure with 5%

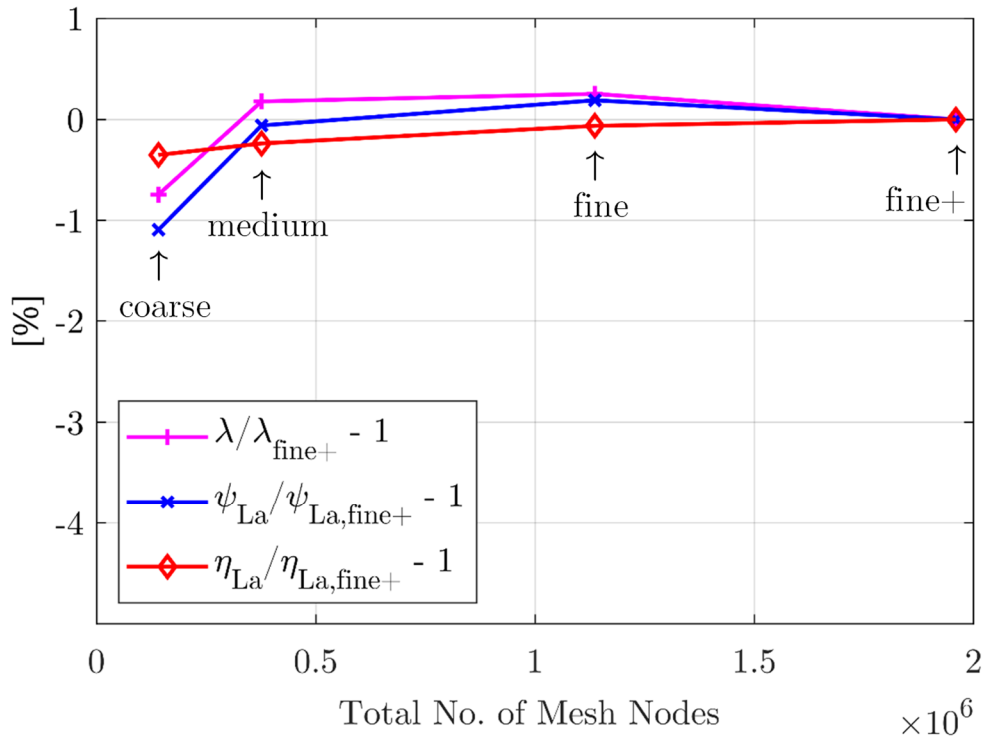


Figure 3.11: Variation of pump performances at different mesh resolutions in the mean-flow passages ($q_b^* = 1.0$, $y^+ = 24.7$)

turbulence intensity and outlet boundary condition as the mass flow rate. At the outlet of the balance drum, the static pressure was specified equal to the suction inlet.

Computational domains and interfaces in the 2nd stage are depicted in Fig. 3.12. The impeller, impeller outblock, front ISR and rear ISR were set as the rotating frame of reference. All other components in the model pump were set as the stationary frame of reference. Sliding interface (=frame change interface) was applied between rotating and stationary components and general grid interface (GGI) between components in the same frame [82]. The no-slip condition was imposed to all wall boundaries. A counter rotating wall condition was applied on the casing walls in the front and rear ISR.

Transient simulations were carried out using the SAS-SST model, and their initial flow-fields were obtained from steady simulations using RANS with SST. After 7 impeller revolutions, the head and power of the 4-stage model pump reached quasi-periodic status. The analysis data was collected from 8th to 12th rotation. Braun [74] investigated various calculation time-steps and convergence-

Table 3.2: Number of mesh nodes

Component	Nodes / each stage	Nodes / whole pump
Suction casing with inlet piping	→	1,155,943
Discharge casing with outlet piping	→	868,511
Suction stage impeller	→	1,785,168
Series stage impeller	2,067,352	6,202,056
Suction and series stage diffuser	2,855,616	8,566,848
Last stage diffuser	→	1,687,668
Suction stage front ISR	→	709,488
Series and last stage front ISR	961,464	2,884,392
Suction stage rear ISR	→	702,592
Series stage rear ISR	720,272	1,440,544
Last stage rear ISR with balance drum	→	2,885,696
Total number of mesh nodes	-	28,888,906

criteria of numerical simulations in a double suction pump. A reasonable compromise between the computational cost and numerical accuracy was achieved at: time step = 0.86° rotation/calculation, internal coefficient loops = 5, RMS residuals = 10^{-4} . In the present study, the following calculation time-step and convergence-criteria was applied: time step = 1.0° rotation/calculation, internal coefficient loops = minimum 3 to maximum 7, RMS residuals = 10^{-4} . The computation was carried out using Intel Xeon Gold 6126 CPU processors with 24 threads/12 cores and 128 GB memory, which were provided by the high-performance cluster Elwetritsch at TU Kaiserslautern as a part of the Alliance of High-Performance Rheinland-Pfalz (AHRP).

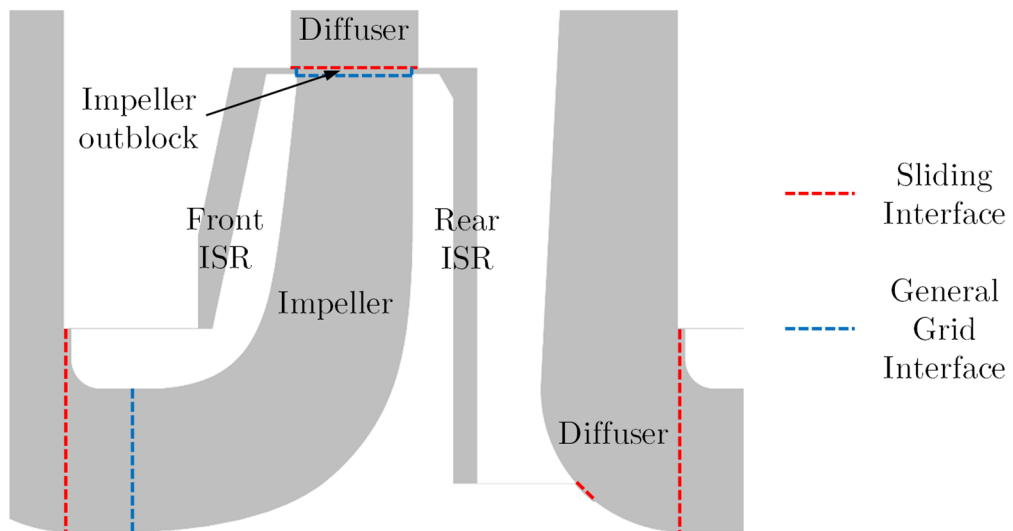


Figure 3.12: Computational domains and interfaces in the 2nd stage

4 Data Analysis Method

When a data variable ϕ is recorded at a sampling rate of f_s during a total sampling time of T to obtain a discrete number of samples of K , its mean, root-mean-square (RMS) and peak-to-peak value can be calculated according to Table 4.1.

Table 4.1: Mean, RMS and peak-to-peak definitions

	formula	remark
<i>Gl. 4-1</i>	$\bar{\phi} = \frac{1}{K} \sum_{j=1}^K \phi(j)$	mean value: time average
<i>Gl. 4-2</i>	$\phi_{\text{RMS}} = \sqrt{\frac{1}{K} \sum_{j=1}^K \phi^2(j)}$	RMS (root-mean-square) value
<i>Gl. 4-3</i>	$\phi_{\text{p-p}} = \phi_{\text{max}} - \phi_{\text{min}}$	peak-to-peak value

Most variables in this work are presented in dimensionless form to analyze measurement results independent of test configurations (e.g. rotational speed and model pump sizes). Table 4.2 summarizes non-dimensionalization methods and variable definitions. Specific speed of a pump in (*Gl. 4-10*) is not completely dimensionless, but is a common definition in European pump industries. Reynolds number is defined as $Re = r_2 u_2 / \nu$ (except Chapter 2 that the Reynolds number dependence of head curves were evaluated with $Re_{\text{IEC}} = u_{1a} d_{1a} / \nu$ according to IEC60193). Physical properties of the test condition such as gravitational acceleration, density of the water, and kinematic viscosity are determined according to [60].

Table 4.2: Non-dimensionalization and variable definitions

	formula	remark
Gl. 4-4	$q_b^* = \frac{Q}{Q_{\text{baseline BEP}}}$	dimensionless flow-rate $Q_{\text{baseline BEP}} = 0.09064 \text{ [m}^3/\text{s]}$
Gl. 4-5	$\psi = \frac{2gH}{u_2^2 z_{st}}$	head coefficient ; for pump-head coefficient $z_{st}=4$, H =overall head ; for stage-head coefficient $z_{st}=1$, H =stage head
Gl. 4-6	$\lambda = \frac{2P}{\rho z_{st} d_2^2 u_2^3}$	power coefficient
Gl. 4-7	$\eta_n = \frac{\eta}{\eta_{\text{BEP of Test 05}}}$	efficiency coefficient
Gl. 4-8	$c_{\bar{p}} = \frac{2(\bar{p} - \bar{p}_{\text{stage inlet}})}{\rho u_2^2}$	static-pressure coefficient
Gl. 4-9	$\overline{k_{shr}} = \sqrt{\frac{2(\bar{p}_2 - \bar{p}_{s1})}{\rho u_2^2 (1 - r_{s1}^2/r_2^2)}}$	average rotation factor in the impeller side room (see Fig. 2.2 for measurement positions)
Gl. 4-10	$n_q = \frac{N\sqrt{Q}}{(H_{ove}/z_{st})^{3/4}}$	specific speed [m ³ /s, m, rpm]
Gl. 4-11	$Re = \frac{r_2 u_2}{\nu}$	Reynolds number
Gl. 4-12	$\Delta p^* = \frac{2}{\rho u_2^2} (p - \bar{p})$	dimensionless pressure-pulsation
Gl. 4-13	$\Delta \widetilde{p^*}(k) = \sum_{j=1+N_R \cdot (k-1)}^{N_R \cdot k} \frac{1}{N_R} \Delta p^*(j)$	dimensionless pressure-pulsation averaged over each shaft rotation ; N_R = number of samples per rotation ; $k = k^{th}$ rotation of the shaft

<i>Gl. 4-14</i>	$\Delta p_{\text{RMS}}^* = \frac{2}{\rho u_2^2} \sqrt{\frac{1}{K} \sum_{j=1}^K (p(j) - \bar{p})^2}$	RMS value of dimensionless pressure-pulsation
-----------------	---	---

Fourier Transform

A continuous data in the time domain $\phi(t)$ can be analyzed in the frequency domain using Fourier transformation as follows:

$$\text{Gl. 4-15} \quad \Phi(f) = \int_{-\infty}^{\infty} \phi(t) e^{-i2\pi f t} dt$$

Because the acquired signal has a finite number of samples, a discrete Fourier transform (DFT) needs to be applied [94]:

$$\text{Gl. 4-16} \quad \Phi(k) = \frac{1}{K} \sum_{j=0}^{K-1} \phi(j) e^{-i2\pi jk/K}$$

A commercial programming language Matlab is used in the present study to perform DFT. Data index in Matlab starts from one instead of zero, and thus the DFT definition in Matlab is slightly different:

$$\text{Gl. 4-17} \quad \Phi_M(k) = \sum_{j=1}^K \phi(j) e^{-i2\pi(j-1)(k-1)/K}$$

Here, $\phi(j)$ corresponds to the real-time data measured at a specific time of $(j - 1)/f_s$ after beginning of the measurement and $\Phi_M(k)$ the transform output at a frequency of $(k - 1)f_R$. Here, f_R is the frequency resolution calculated by $f_R = 1/T$. The amplitude spectrum can be calculated as follows:

$$\text{Gl. 4-18} \quad \Phi_A(k) = \frac{1}{K} |\Phi_M(k)|$$

$\Phi_A(1)$ indicates 0 Hz component that equals the mean value of the signal in the time domain. Φ_A is two-sided amplitude spectrum, and the second half of the spectrum (=from $f_s/2$, which is the Nyquist frequency, to f_s) is always a mirror of the first half in a physical signal. By discarding the redundant second-half of the spectrum and correcting the amplitude of the first-half, single-sided spectrum $\Phi_{A,s}$ can be obtained:

$$Gl. 4-19 \quad \Phi_{A,s}(1) = \Phi_A(1) \quad \text{and} \quad \Phi_{A,s}(k) = 2\Phi_A(k) \quad \text{where} \quad k = 2, 3 \dots K/2$$

Evaluation of Pressure Pulsations

Pressure pulsations generated in a pump usually contain various peaks at discrete frequencies and broadband excitations. Therefore, it is often convenient to use the RMS value of dimensionless pressure-pulsations since the energy content can be evaluated over a defined frequency bandwidth [40]. If the whole frequency range from f_R to $f_s/2$ is of interest, the RMS value of pressure pulsations can be calculated both in the time domain by (Gl. 4-14) and frequency domain. Rayleigh's theorem (or Parseval's theorem) describes that the sum of the square of a signal in the time domain is equal to the sum of the square of its spectrum since the total energy content must be the identical in both domains. The RMS value of dimensionless pressure-pulsations for a specific frequency range from f_{BL} to f_{BH} can be calculated as follows:

$$Gl. 4-20 \quad \Delta p_{\text{RMS,BB}}^* = \frac{1}{\sqrt{2}} \sqrt{\sum_{j=k_{BL}}^{k_{BH}} \Phi_{A,s}^2(j)}$$

$$\begin{aligned} \text{where} \quad k_{BL} &= \frac{f_{BL}}{f_R} + 1 \quad \text{for} \quad f_{BL} > 0 \text{ Hz}, \\ k_{BH} &= \frac{f_{BH}}{f_R} + 1 \quad \text{for} \quad f_{BH} < \frac{f_s}{2} \end{aligned}$$

A sum of multiple RMS values of different bandwidths can be calculated by the square root of the sum of the squares (SRSS) method:

$$Gl. 4-21 \quad \Delta p_{\text{RMS, BB, sum}}^* = \sqrt{\sum_{j=1} (\Delta p_{\text{RMS, BB, } j}^*)^2}$$

The *overall* RMS value of dimensionless pressure-pulsations can be calculated by defining a frequency bandwidth that captures all *meaningful* hydraulic excitations generated by a pump:

$$Gl. 4-22 \quad \Delta p_{\text{ove}}^* = \frac{1}{\sqrt{2}} \sqrt{\sum_{j=k_{\text{ove,L}}}^{k_{\text{ove,H}}} \Phi_{A,s}^2(j)}$$

$$\text{where } k_{\text{ove,L}} = \frac{f_{\text{ove,L}}}{f_R}, \quad k_{\text{ove,H}} = \frac{f_{\text{ove,H}}}{f_R}$$

The low-frequency limit for the overall RMS value ($f_{\text{ove,L}}$) should be sufficiently smaller than the slowest meaningful flow-motion. Sinha *et al* [56] detected a slow rotating stall at 0.93 Hz ($=0.0627 f_n$) in a single stage pump. Wang and Tsukamoto [95] reported a rotating stall at 0.24 Hz ($=0.0096 f_n$). There are even slower flow-motions for a vertical pump installed in sump structures at below 0.1 Hz, but it is not of interest in the current project. Therefore, the low-frequency limit can be set as:

$$Gl. 4-23 \quad f_{\text{ove,L}} = \min(0.005 f_n, 0.1 \text{ Hz})$$

The high-frequency limit ($f_{\text{ove,H}}$) must capture all important super-harmonics of the vane passing frequency, but *not* include cavitation noise that usually appears over several kHz range. Then, $f_{\text{ove,H}}$ must be larger than $3 \times \text{VPF}$, but preferably larger than $5 \times \text{VPF}$. Since VPF in the current project is 280 Hz, $f_{\text{ove,H}}$ can be set as:

$$Gl. 4-24 \quad f_{\text{ove,H}} = 2000 \text{ Hz}$$

Figure 4.1 shows typical spectra of dimensionless pressure-pulsations at the diffuser inlet (refer to PT31 in Fig. 2.2). Dominant peaks are observed at VPF and its integer multiples. Even though the measurement position is in the 2nd stage of the multistage pump, a weak broadband-excitation is detected at around 3.6 kHz that is induced by the cavitation in the suction stage. It is because $NPSH_{av}$ was slightly lower than $NPSH_i$ of the suction stage during the model pump test. The selected $f_{ove,H}$ is sufficiently smaller than frequencies caused by the cavitation noise, but high enough to capture all important hydraulic-excitations produced by the model pump. The selected $f_{ove,L}$ is small enough to detect a very slow rotating-stall in the diffuser as will be discussed in Fig. 6.8.

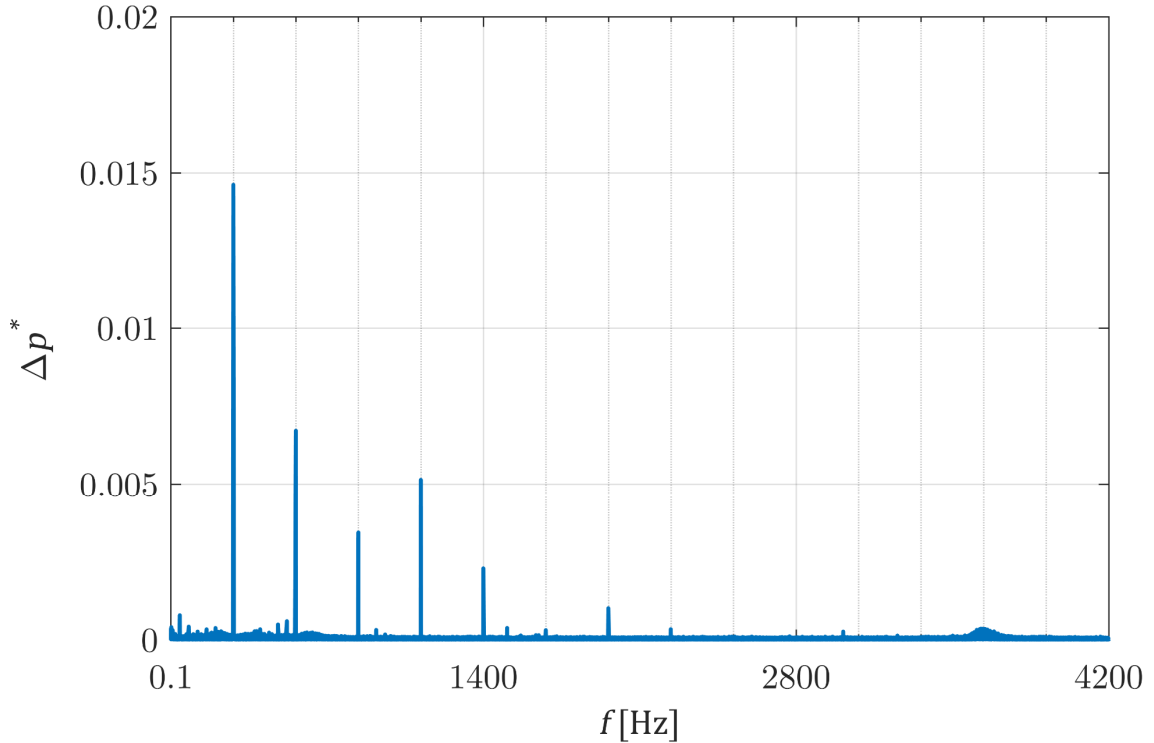


Figure 4.1: Spectra of dimensionless pressure-pulsations measured at the diffuser inlet in the 2nd stage of the model pump ($q_b^* = 1.0$) (ordinate = zero-to-peak amplitude)

Data Window

Since the data acquisition is carried out during a limited sampling time, some periodicities in the original signal may be truncated at the end of the data samples. It causes a leakage error in the spectrum and a peak amplitude at a single frequency leaks into its adjacent bands [58, 96]. The leakage error can be suppressed by multiplying a window function into the original real-time signal. One of the most common window-functions in engineering applications is the Hanning window [58]:

$$Gl. 4-25 \quad w(t) = \frac{1}{2} \left(1 - \cos \left(\frac{2\pi t}{T} \right) \right) \quad \text{for } t = 0 \sim T$$

It removes the discontinuity of the beginning and end of the original signal, which gives a smooth transition at both ends.

However, an introduction of the Hanning window results in a reduction of the amplitude and energy in the spectrum since the real-time data is distorted. Correction factors are necessary to compensate the losses. The zero-to-peak amplitude of spectrum can be corrected by a multiplication factor of 2 to improve the accuracy of the peak amplitude at discrete frequencies such as VPF, its super-harmonics, and rotating stall. The RMS amplitude can be corrected by a multiplication factor of $\sqrt{8/3}$ to estimate an accurate energy-level over a defined frequency bandwidth. The present study adopts the Hanning window and above correction factors for the post-processing of the DFT output.

5 Investigation of Head-Curve Instability in a Multistage Pump

5.1 Performance Curve

Figure 5.1 shows performance curves of the 4-stage model pump with hydraulic configuration of Test-05 (see Table 1.1). The blue dotted lines represent measured data and the black solid lines numerically predicted data. ψ , η_n and λ are dimensionless overall-head, efficiency and power coefficient, respectively. Because the CFD simulations estimated only the inner power, mechanical losses of the rotor that had been measured in a separate test were added to the numerically predicted power in order to obtain the efficiency and

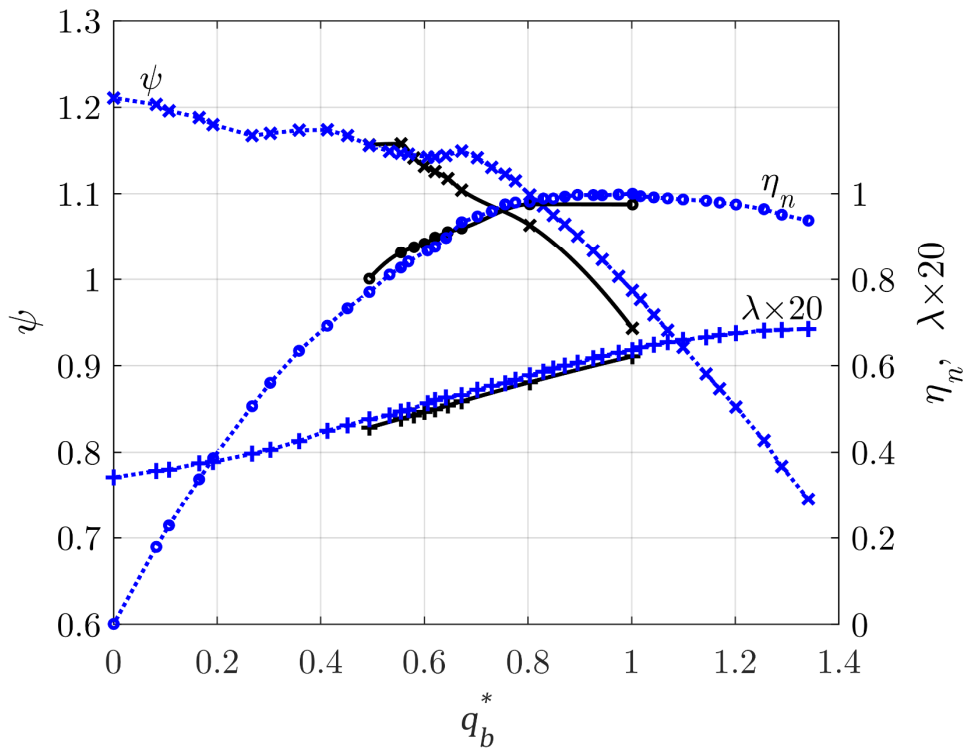


Figure 5.1: Overall-performance curves of Test-05; blue dotted line – test, black solid line – CFD

power curves in Fig. 5.1. The measured n_q of the pump is 29.6. Two instabilities are observed in the measured head-curve with weak head-drop of 0.6% at $q_b^* = 0.67$ and 0.41. The instability is also detected in the CFD simulation, but its onset flow-rate is somewhat delayed compared to the experiment. The numerical simulation under-predicts head and power at most flow-rates. The performance deviation at BEP between the prediction and measurement is -4.6% for head, -2.5% for efficiency, and -2.2% for power.

Figure 5.2 shows measured stage-head curves together with overall-head curve. Head curves in the individual stages are distinctly different from each other. The 1st stage produces a very unstable head-curve. A large head-drop below $q_b^* = 0.41$ plays a decisive role to generate the instability in the overall-head curve at this flow-rate. The suction impeller has a large inlet-diameter considering cavitation performance, and thus a strong inlet-recirculation and pre-rotation is expected for reduced flow-rates [3, 31]. The pre-swirl is not well suppressed due to the long distance between the impeller leading edge and flow-guide ribs in the suction casing as shown in Fig. 2.1. This is a unique characteristic in the 1st stage since impellers in the other stages are positioned as close as possible to return vanes of the previous stage that act like swirl brakes and weaken the pre-rotation. The strong pre-swirl in the 1st stage results in a decrease of Euler head as $H_{th} = (u_2 c_{2u} - u_1 c_{1u})/g$ and causes the excessive head-drop below $q_b^* = 0.41$. A sudden rise in the head curve is observed below $q_b^* = 0.25$. This head rise may be caused by increasing recirculation towards shut-off as explained in Chapter 1 in the context with $\Delta H_{Rec} = u_2^2(d_{1a}^2 - d_{1eff}^2)/(2gd_2^2)$. The series stages (=2nd and 3rd stages) have a direct impact on the instability in the overall-head curve at $q_b^* = 0.67$. Internal-head curves and flow patterns in the 2nd stage will be analyzed later in this work. Note that both 2nd and 3rd stages are equipped with the same impeller and diffuser, but the shut-off head are distinguishably different. It may have something to do with flow patterns at the impeller inlet and/or alternating stall in the diffuser. The 2nd stage impeller receives incoming-flow from return vanes of the suction stage. Thus, its inlet-velocity profiles cannot be the same with those in the other stages, especially below the onset flow-rate of inlet recirculation. The stage-head curves were measured at two or three out of twelve

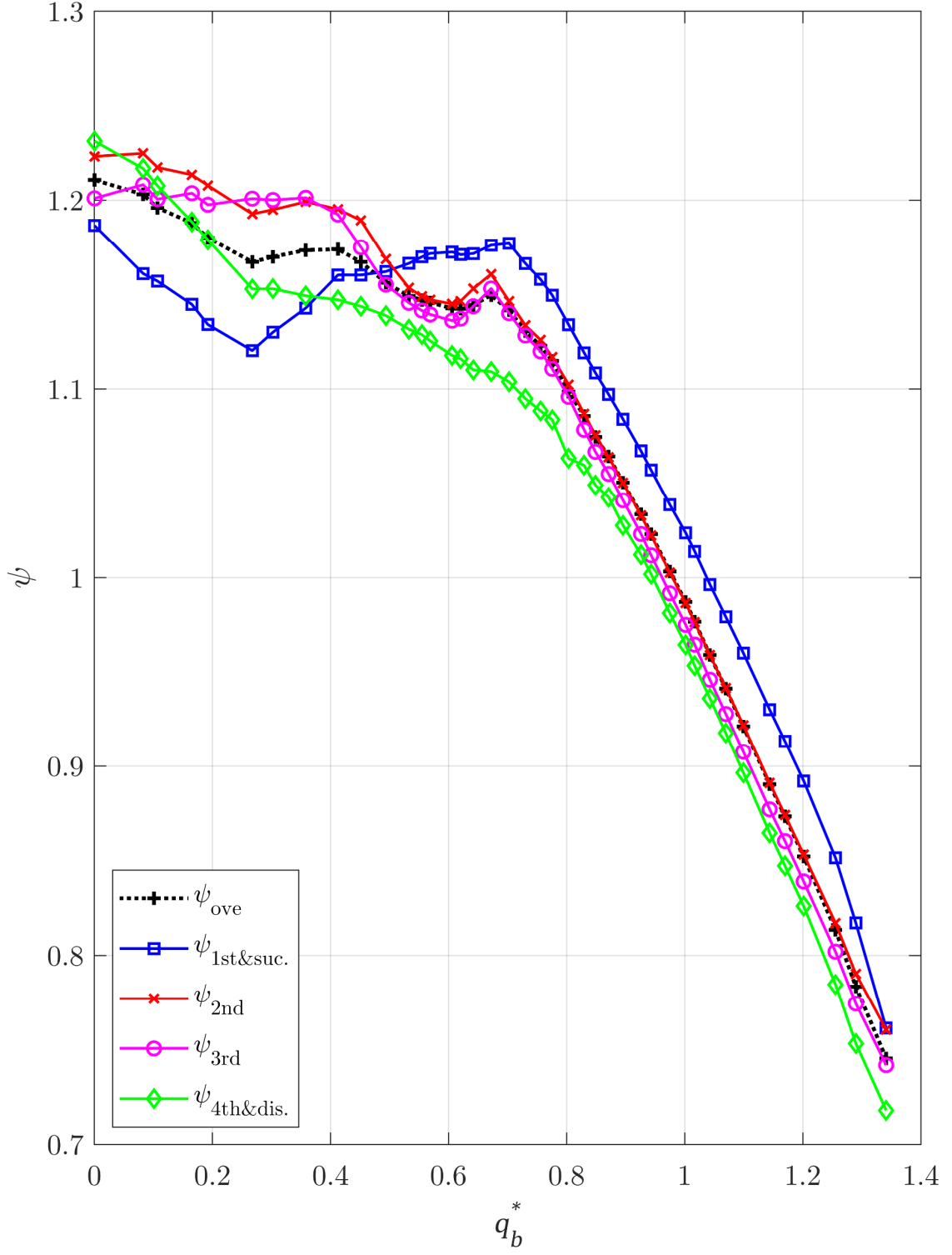


Figure 5.2: Stage-head curves of Test-05 from the measurement

return-vane channels in each stage (refer to the evaluation section 6 in Fig. 2.2). If flow in one stage was stalled in the measuring channel(s) while that in the other stage was normal, the alternating stall might contribute to the differences in the head curve between the 2nd and 3rd stage. The last stage produces a stable head-curve over the whole flow-range. Noticeably, it gives a flat head-rise near $q_b^* = 0.67$ while the other stages have the instability. The last-stage diffuser is connected to the annular chamber and discharge casing that generates non-uniform pressure distribution over the circumference at the diffuser outlet. This unique characteristic seems to cause a different head-loss mechanism in the last stage compared to the other stages. Flow patterns in the last diffuser will be further discussed in Chapter 5.3.

Figure 5.3 presents a measured loss-coefficient in the suction casing that shows the onset of inlet recirculation in the 1st stage. Static pressures were measured on the pipe at 2D away from the suction flange and on the casing wall in front of the 1st impeller inlet (marked R in Fig. 2.1). The difference between them indicates a static-head loss in the suction casing as $\Delta H_s = \zeta c^2 / (2g)$. Here, ΔH_s is the static-head loss, ζ the loss coefficient in the suction casing, and c the

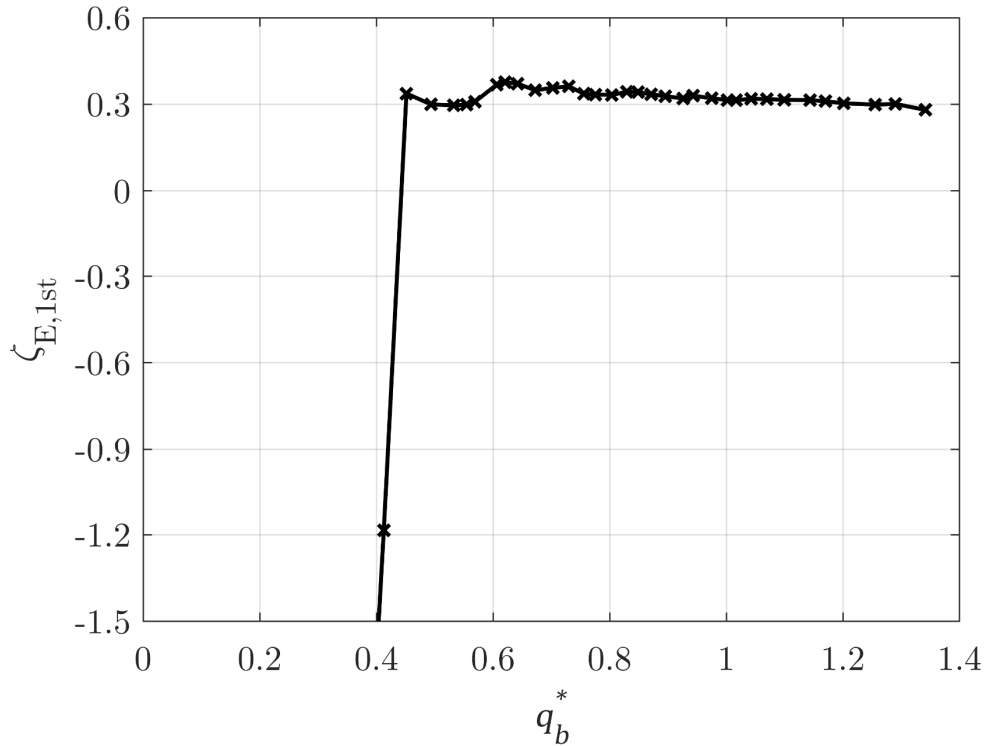


Figure 5.3: Loss coefficient in the suction casing and the onset flow-rate of inlet recirculation of Test-05 from the measurement

mean-velocity at the measuring section. $Q - \Delta H_s$ curve tends to follow a parabola until inlet recirculation occurs. Once the recirculation induces pre-rotation, a quadratic pressure-distribution is generated in the approach flow perpendicular to the shaft axis. Then, the pressure-difference reading becomes negative, and $Q - \Delta H_s$ curve starts to deviate from the parabola. An example to detect the onset flow-rate of recirculation by drawing $Q - \Delta H_s$ curve can be found in [97]. In the present study, inlet recirculation is detected in a slightly different manner using a total-head loss coefficient in the suction casing ($\zeta_{E,1st}$) as:

$$Gl. 5-1 \quad \zeta_{E,1st} = \frac{2gZ_{E,1st}}{c_{1m}^2}$$

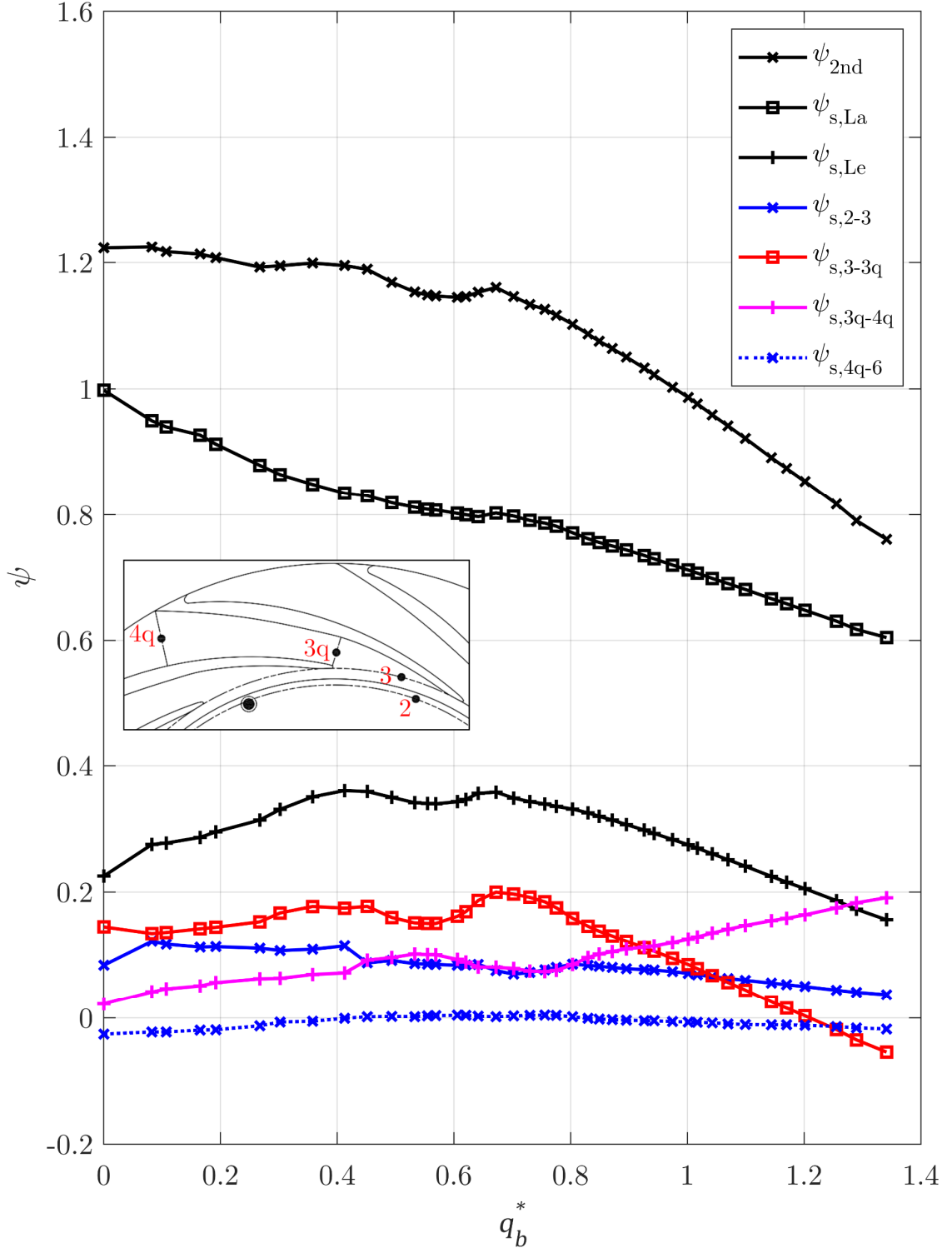
$$\text{where } Z_{E,1st} = \frac{p_{\text{suction nozzle}} - p_{1st \text{ stage inlet}}}{\rho g} + \frac{c_{\text{suction nozzle}}^2 - c_{1m}^2}{2g},$$

$$c_{1m} = \frac{4Q}{\pi(d_1^2 - d_n^2)}$$

Since the influence of flow rate on the head loss is offset in (Gl. 5-1), $Q - \zeta_{E,1st}$ curve can stay roughly constant independent on the operating point until the recirculation occurs. Figure 5.3 shows measured output that provides two information: (a) the loss coefficient of the present suction-casing is around 0.3, and (b) the onset of recirculation is clearly detected at around $q_b^* = 0.41$. The large head-loss in the 1st stage (Fig. 5.2) and the onset of inlet recirculation (Fig. 5.3) occurs at the same flow-rate ($q_b^* = 0.41$), which suggests a close correlation between them.

The 2nd stage head curve is further analyzed based on internal-head curves in Fig. 5.4. Static pressures were measured at various positions in the impeller and diffuser, and then the differences between each evaluation section were calculated (see Fig. 2.2. for position definition of the evaluation sections.) The contribution of each hydraulic section to the head generation and instability in the 2nd stage is shown in this figure.

- (1) The head rise in the 2nd stage (ψ_{2nd}) is equal to a sum of the static-head rise in the impeller and diffuser as $\psi_{2nd} = \psi_{s,La} + \psi_{s,Le}$. The instability with 1.4%

Figure 5.4: 2nd stage internal-head curves of Test-05 from the measurement

head drop at $q_b^* = 0.67$ is of main interest in the present analysis.

- (2) The static-head rise in the impeller ($\psi_{s,La}$) exhibits a tiny instability at $q_b^* = 0.67$. Below this flow-rate, $\psi_{s,La}$ steeply increases and helps to stabilize the stage-head curve.
- (3) The pressure recovery in the diffuser ($\psi_{s,Le}$) increases with decreasing flow-rate above $q_b^* = 0.67$. There is a large loss at $q_b^* = 0.67 \sim 0.57$ that is the main cause of the instability in the stage-head curve. A steep positive-gradient $d\psi_{s,Le}/dQ$ is observed below $q_b^* = 0.41$, which results in a mild-slope of the stage-head curve. Based on flow observations in a diffuser-type single-stage pump in [1, 3], this low pressure-recovery at deep part-load is related to excessive flow-separation in the diffuser. At shut-off, the diffuser contributes to 18% of the head rise. The pressure recovery in the diffuser can be further analyzed based on $\psi_{s,Le} = \psi_{s,2-3} + \psi_{s,3-3q} + \psi_{s,3q-4q} + \psi_{s,4q-6}$.
- (4) The pressure rise between the impeller outlet and diffuser inlet ($\psi_{s,2-3}$) tends to show a mild negative-gradient $d\psi_{s,2-3}/dQ$ at most flow-rates. This section

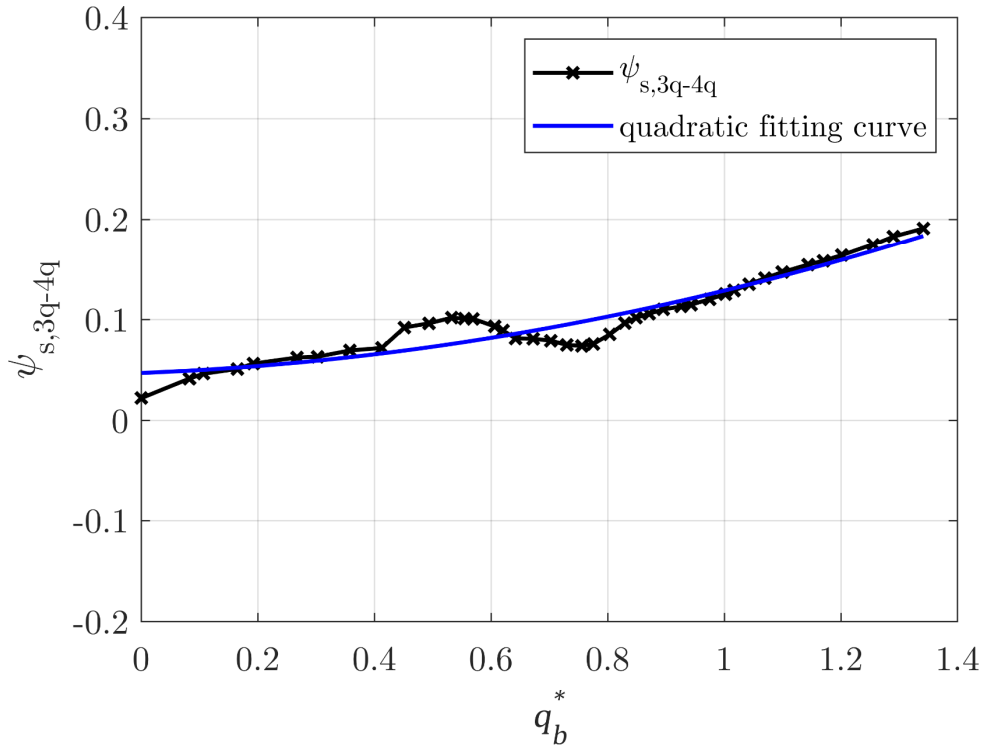


Figure 5.5: Pressure recovery in the diffusing channels of Test-05 from the measurement and its quadratic fitting curve by the least-squares-method

(=Gap B) acts like a vaneless diffuser with the pressure recovery largely governed by conservation of angular momentum.

- (5) The pressure recovery between the diffuser inlet and inlet throat ($\psi_{s,3-3q}$), which is called as the inlet triangular section, strongly stabilizes the head curve above $q_b^* = 0.67$. However, at $q_b^* = 0.67 \sim 0.57$, it becomes very unstable and has the largest impact on the instability of the stage-head curve. Therefore, to understand flow patterns generating the excessive loss in the inlet triangular section at these flow-rates is a key to identify the origin of the head-curve instability. Another noticeable point is that this small-section generates the largest pressure-recovery among all hydraulic sections in the diffuser below $q_b^* = 0.93$. Above $q_b^* = 1.2$, flow is strongly accelerated and $\psi_{s,3-3q}$ becomes negative due to increasing friction-losses.
- (6) The pressure recovery in the diffusing channels ($\psi_{s,3q-4q}$) is generally destabilizing over the whole flow-range – except at $q_b^* = 0.76 \sim 0.57$. Since this section works in a similar way as a conical diffuser in a pipe (=a gradual expansion of channel area along the streamline to convert kinetic energy into a rise in static pressure), it is expected that $Q - \psi_{s,3q-4q}$ curve roughly follows a parabola. Figure 5.5 shows that this assumption is partly correct, indicating that the diffusing channel is, by nature, a *destabilizing* component for the stage-head curve. It is interesting that $\psi_{s,3q-4q}$ *stabilizes* the head curve near the onset of the instability. Some possible reasons will be discussed in Chapter 5.2 based on flow patterns estimated by CFD simulations.
- (7) The loss in the return vanes ($\psi_{s,4q-6}$) is quite small. $Q - \psi_{s,4q-6}$ curve is mostly flat over the whole flow-range.

Figures 5.6 and 5.7 compare internal-head curves in the 2nd stage estimated by numerical simulations and measured by the test. The instability in ψ_{2nd} curve is detected by the CFD simulation, but at a smaller flow-rate compared to the measurement. It is interesting that a decent agreement is observed in $\psi_{s,La}$ between the prediction and experiment above $q_b^* = 0.67$ (where is most likely the onset flow-rate of outlet recirculation in the measurement). The numerical simulation largely under-estimates $\psi_{s,Le}$ in the whole operating-point, which accounts for most of the deviation of the stage-head curve between the

prediction and test above $q_b^* = 0.67$. Figure 5.7 shows that the excessive loss in $\psi_{s,3-3q}$ at the instability is not correctly predicted by the CFD. Presumably, the current numerical simulation method cannot accurately estimate mixing losses in separated flows. The CFD simulation under-estimates $\psi_{s,3q-4q}$ at the whole flow-range. Figures 5.6 and 5.7 indicate that the quantitative accuracy of the present CFD output is not satisfactory.

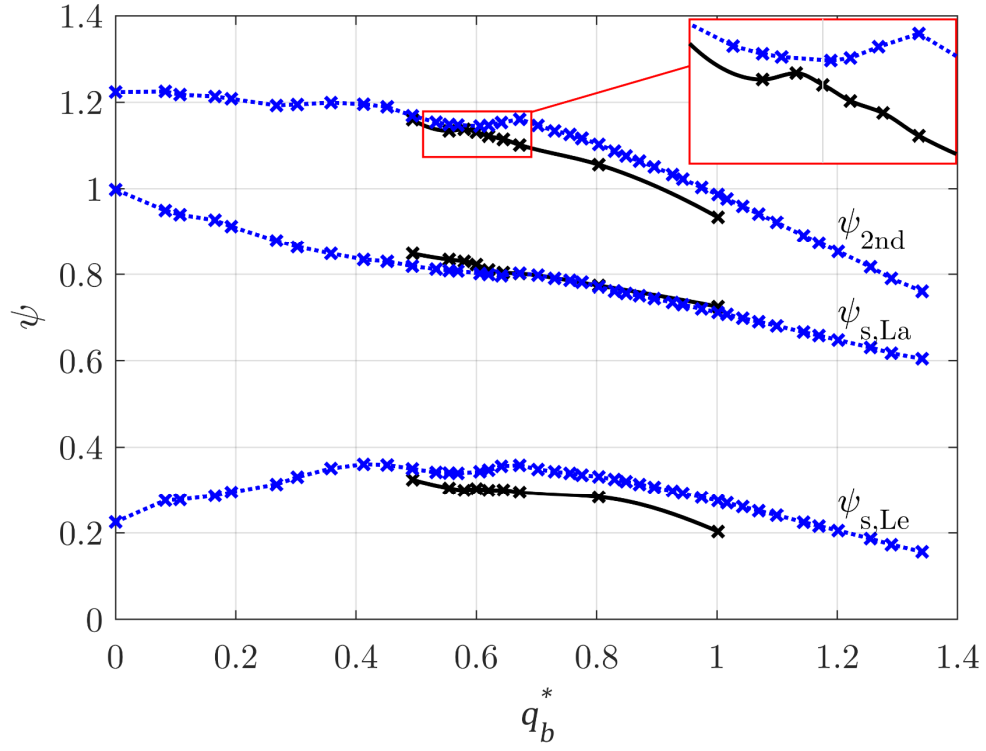


Figure 5.6: 2nd stage internal-head curves of Test-05; blue dotted line – test, black solid line – CFD

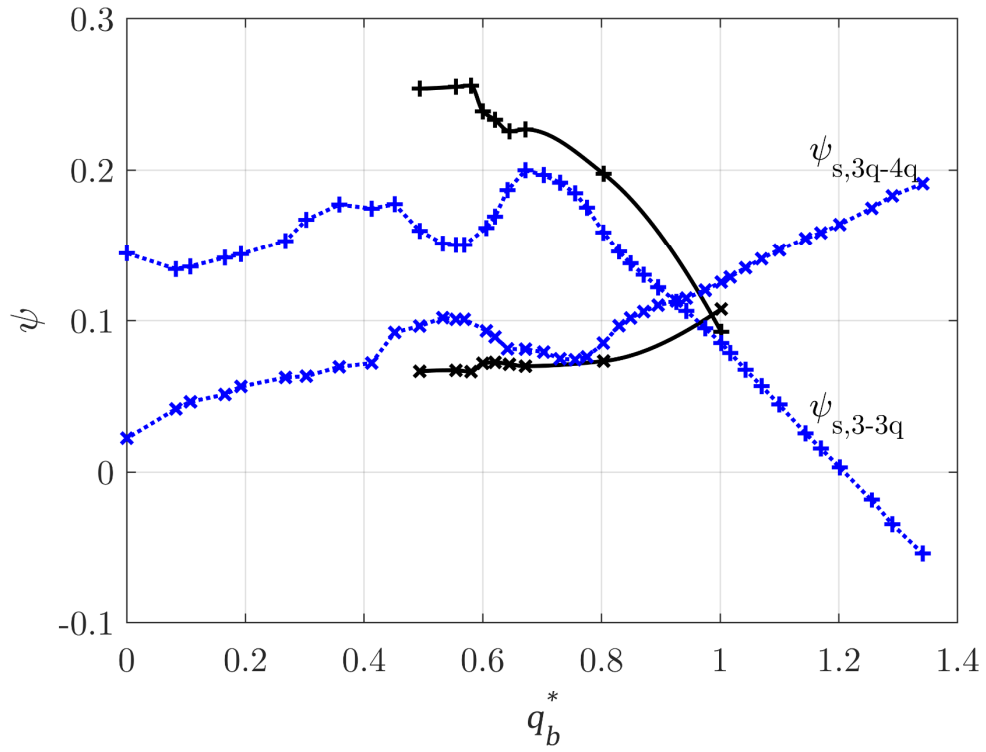


Figure 5.7: Static-head curves in the inlet triangular section and diffusing channels in the 2nd stage of Test-05; blue dotted line – test, black solid line – CFD

5.2 Flow Pattern Switching

Flow patterns in the impeller and diffuser are investigated to understand the cause of the head-curve instability. Figure 5.8 presents average rotation factors ($\overline{k_{shr}}$) on the front ISR in the 2nd stage for different flow-rates. The blue dotted line indicates measured data and the black solid line numerically predicted data. $\overline{k_{shr}}$ were calculated by (Gl. 4-9) using static pressures sampled at two different radii in the ISR (position s1 and 2 in Fig. 2.2). Both predicted and measured output show a similar trend: $\overline{k_{shr}}$ begins to drop below $q_b^* = 0.8$, reaches the minimum near the onset flow-rate of the head-curve instability, and then sharply rises at a further reduced flow-rate.

Pressure decay in the ISR can also be appreciated in Fig. 5.9. The ordinate indicates dimensionless radius. $r/r_2 = 1$ corresponds to the radius of the impeller blade outlet and $r/r_2 = 0.67$ the radius of the annular seal. The abscissa is pressure coefficient determined by (Gl. 4-8). Measured and numerically estimated output are presented at the upper and lower figure, respectively. It is noticeable that the slope of pressure distribution in the ISR significantly varies

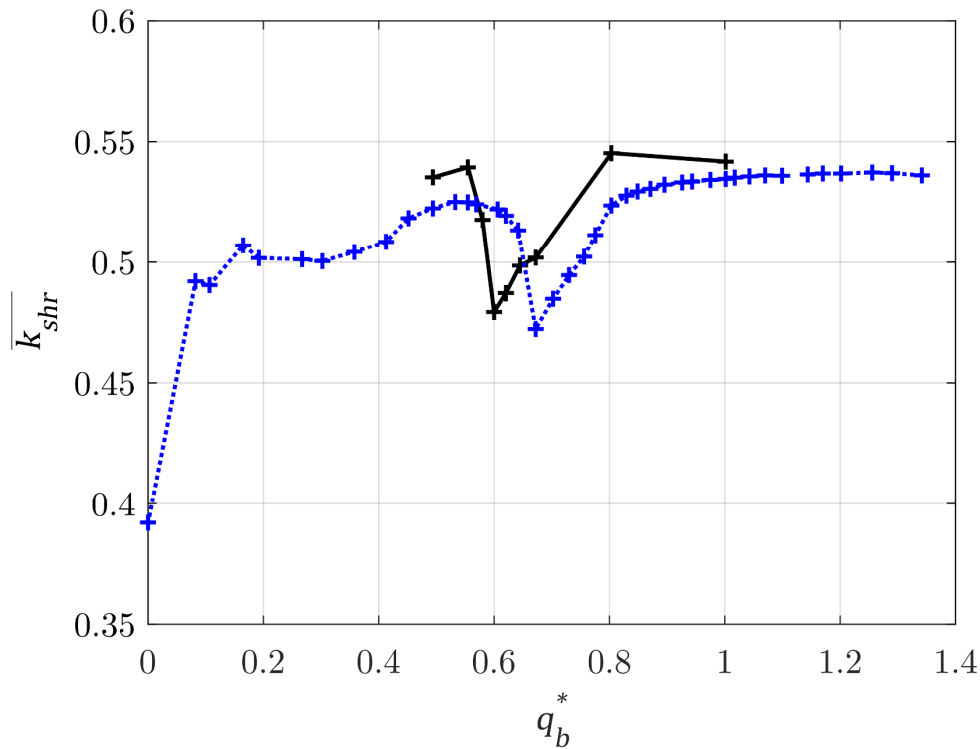


Figure 5.8: Average rotation factors on the front ISR in the 2nd stage of Test-05; blue dotted line – test, black solid line – CFD

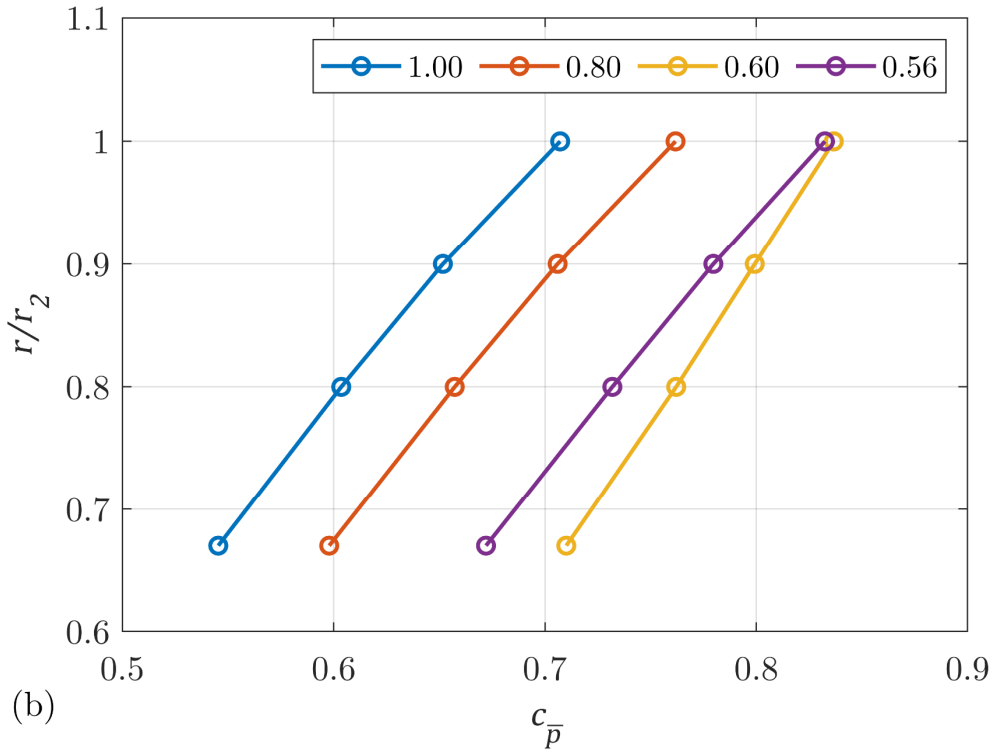
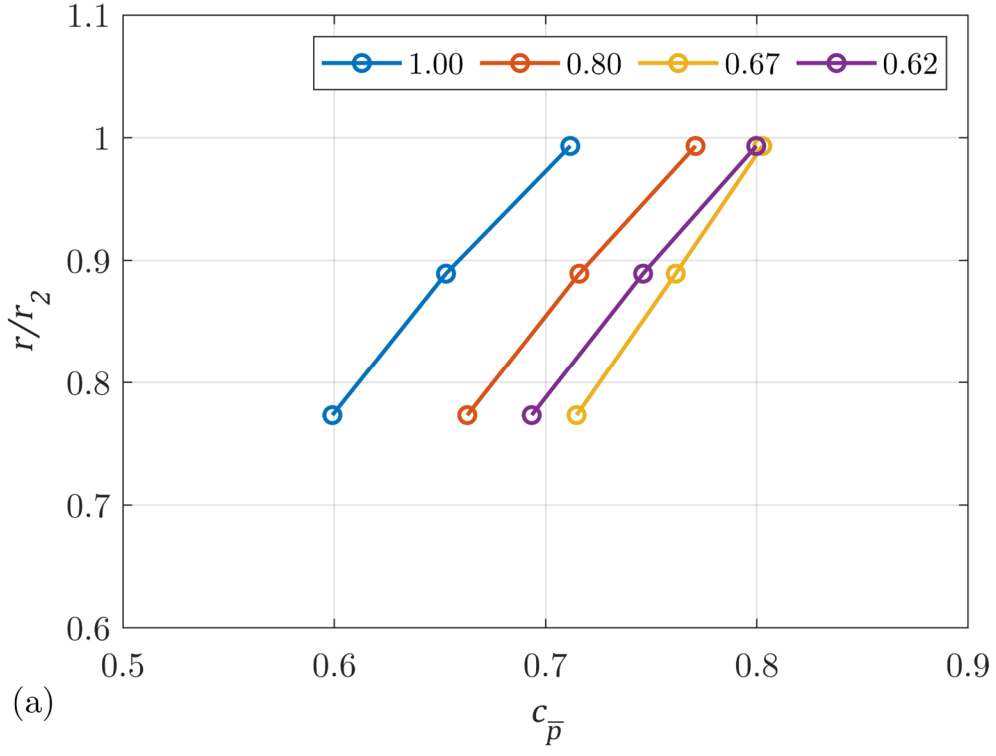


Figure 5.9: Pressure-coefficient distribution on the front ISR in the 2nd stage of Test-05; (a) test, (b) CFD; legend indicates the flow rate

when the pump operates near the onset of the instability (see $q_b^* = 0.67$ for the test and $q_b^* = 0.60$ for the CFD). Fluid at the impeller outlet enters the front ISR through a small gap between shroud plates of the impeller and diffuser and moves radially inwards along the casing wall from the outer radius to annular seal. Therefore, the circumferential velocity component of the main flow has a significant effect on the pressure profile in the ISR [3]. The sudden change of $\overline{k_{shr}}$ and $c_{\bar{p}}$ near the onset of the instability indicates that:

- (1) there is an abrupt variation of flow patterns at the impeller outlet, and
- (2) flow phenomenon causing the instability in the test and CFD is likely to be similar (even though the onset flow-rate is different).

Figure 5.10 shows span-wise velocity distributions at the impeller outlet for different flow-rates. The left and right figure is dimensionless meridional and circumferential velocity component, respectively, that were estimated by the CFD simulations. Both velocity components were time-averaged during the last five revolutions of the impeller, and then circumferentially area-averaged at each

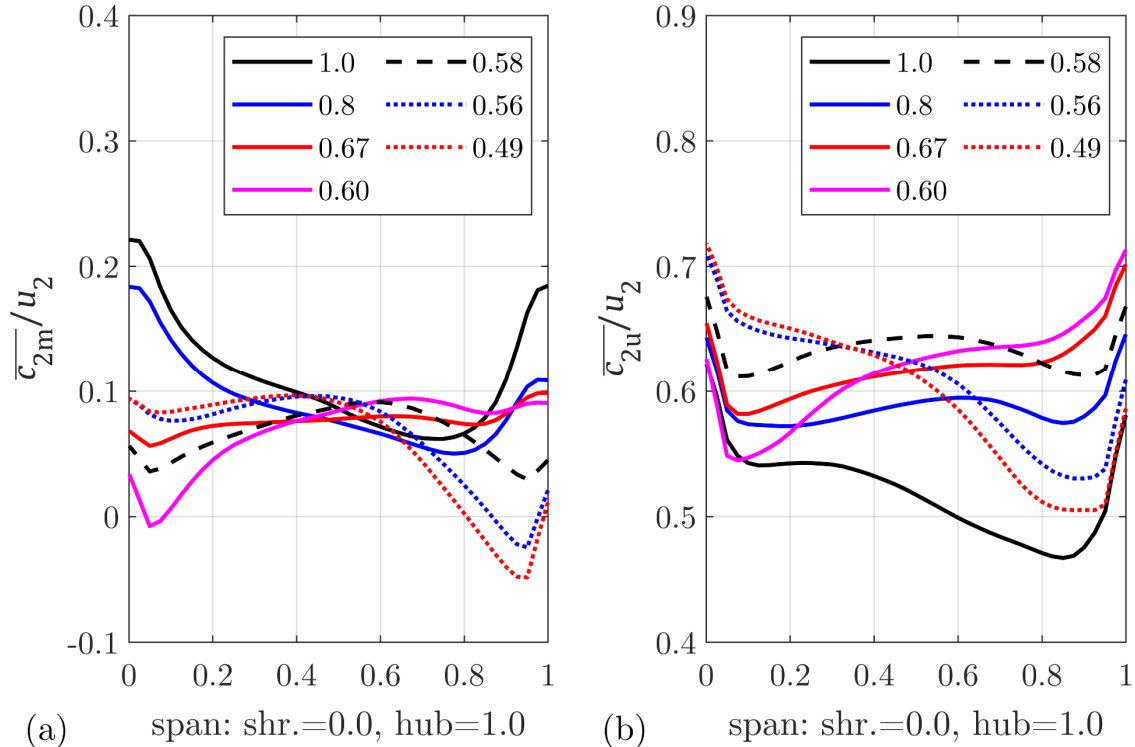


Figure 5.10: Span-wise velocity distribution at the impeller outlet in the 2nd stage from the CFD of Test-05 (legend indicates q_b^*); (a) dimensionless meridional-velocity, (b) dimensionless circumferential-velocity

span position.

- (1) At BEP, two major streamlines appear near the shroud and hub. The meridional-velocity profile is similar like “M”-shape. According to some 2D diffuser studies [98, 99], the “M”-shaped velocity distribution, which the velocity at the mid-height is low and that near walls is high, tends to give very high pressure-recovery in the diffuser compared to other inlet-velocity profiles such as a uniform, skewed, jet, or stepped shape.
- (2) With decreasing flow-rate, the meridional velocity at the impeller outlet also decreases but not uniformly along the span. At $q_b^* = 0.80$, $\overline{c_{2m}}/u_2$ largely drops near the hub. At $q_b^* = 0.67$, a huge decrease of $\overline{c_{2m}}/u_2$ occurs near the shroud.
- (3) Outlet recirculation begins to appear at $q_b^* = 0.60$ near the shroud ($\overline{c_{2m}}/u_2 < 0$). Since the recirculation brings fluid with low c_{2u} from the diffuser into impeller, a drop in $\overline{c_{2u}}/u_2$ is also observed near the shroud. At $q_b^* = 0.58$, no backflow is observed in any span position, and $\overline{c_{2u}}/u_2$ distribution becomes relatively flat over the span. At $q_b^* = 0.56$, the flow recirculation suddenly moves to the hub, resulting in a large drop in $\overline{c_{2u}}/u_2$ near the hub. At $q_b^* = 0.49$, the flow recirculation stays near the hub and becomes stronger.

While the operating flow-rate is reduced by just 4% from $q_b^* = 0.60$ to 0.56, the outlet recirculation abruptly moves from the shroud to hub. This phenomenon is called the *flow pattern switching* [1, 2]. Figure 5.10 demonstrates the occurrence of the flow pattern switching at the instability by means of numerical simulations.

The sudden movement of recirculation explains why $\overline{k_{shr}}$ and $c_{\bar{p}}$ in the front ISR abruptly vary in Figs. 5.8 and 5.9. At the onset of the instability, outlet recirculation appears near the shroud and fluid with low c_{2u} enters the outer radius of the front ISR. Flow rotation in the side room becomes slow, changing the slope of the pressure profile along the radii. At a slightly reduced flow-rate, the outlet recirculation moves to the hub. The main flow exiting the impeller blades with high c_u can enter again the front ISR, and it recovers $c_{\bar{p}}$ distribution and $\overline{k_{shr}}$ into the normal level.

Figure 5.11 depicts meridional velocity contours and vectors in the 2nd stage impeller for different flow-rates. The thick arrow lines and dashed circle are

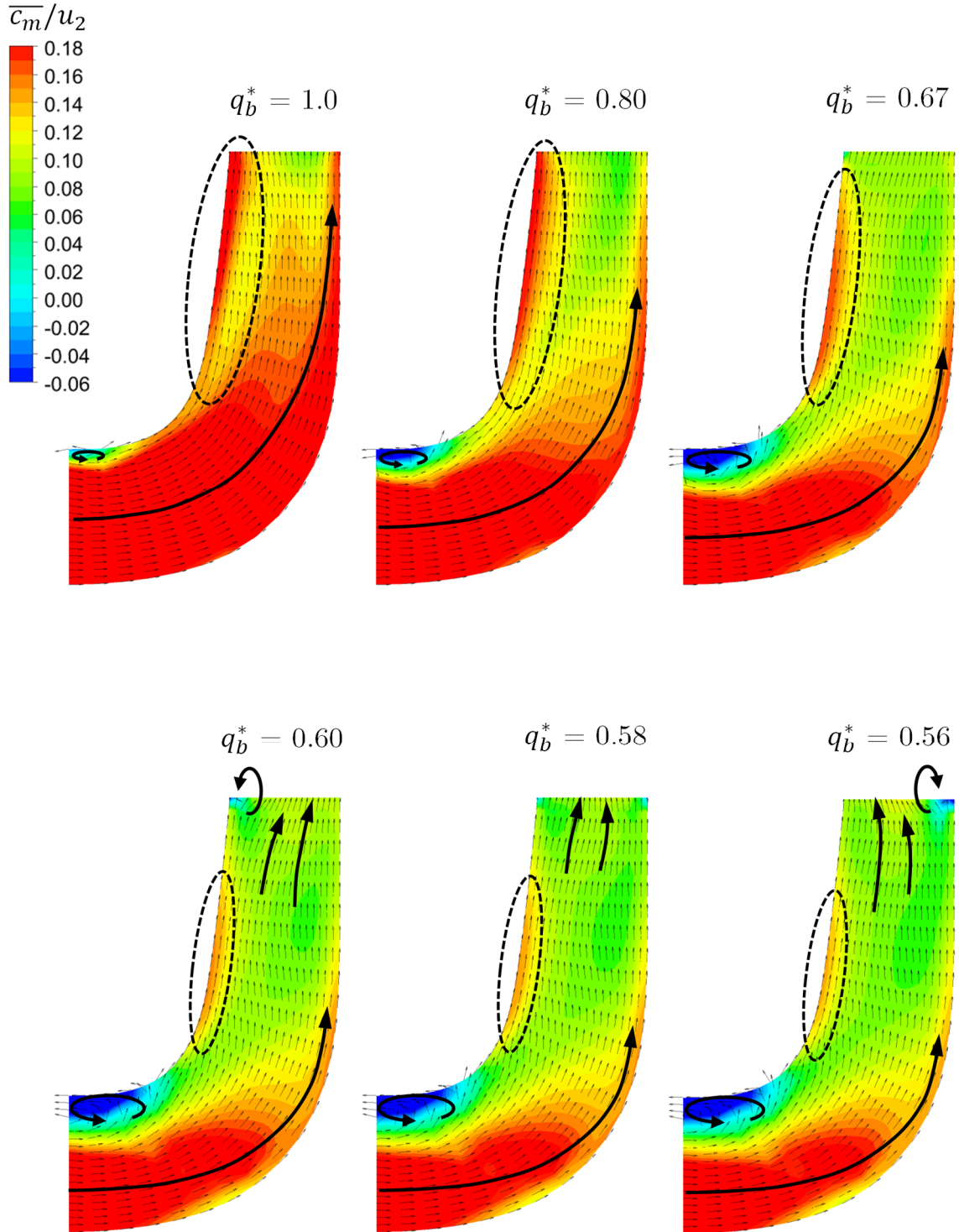


Figure 5.11: Dimensionless meridional-velocity contours with vectors in the 2nd stage impeller from the CFD of Test-05

added to ease the interpretation of flow patterns. The meridional velocity component was time-averaged during the last five revolutions of the shaft, and then circumferentially area-averaged at each sampling position. At BEP, two major streamlines (red color) are observed at the impeller outlet. One streamline follows from the impeller inlet to outlet-hub and another along the shroud meridional-curvature. There is a small inlet-recirculation even at BEP because the incoming fluid turns 90° from the return vane outlet of the previous stage to the impeller inlet. At $q_b^* = 0.80$, the streamline from the inlet to outlet-hub is quickly weakened. At $q_b^* = 0.67$, the inlet recirculation becomes large enough to push the inlet streamline toward the hub. Below $q_b^* = 0.60$, the flow pattern switching occurs at the impeller outlet. Flow recirculation (deep-blue color) appears near the shroud ($q_b^* = 0.60$), disappears ($q_b^* = 0.58$), and moves to the hub ($q_b^* = 0.56$).

The flow pattern switching has a strong impact on velocity distributions in the diffuser. Figure 5.12 and 5.13 present dimensionless velocity contours at the shroud (dimensionless span = 0.05), mid (span = 0.5) and hub (span = 0.95) for various flow-rates. The velocity component was time-averaged during the last five revolutions of the rotor. The dimensionless span position is defined based on the impeller outlet width as depicted in Fig. 5.14 in order to directly correlate flow patterns between the impeller and diffuser at the same span. Velocity profiles in the diffuser vary with the operating point as follows:

- (1) at BEP: Flow patterns in the diffuser are almost axisymmetric. Small separations are observed on the vane pressure-side.
- (2) at $q_b^* = 0.80$: Each vane channel shows a slightly different flow-pattern.
- (3) at $q_b^* = 0.67$: There are discernible flow-separations in three vane passages (3, 7 and 11 o'clock position). Based on an observation of transient flow motions during the calculation time (not depicted in this work), these stalls were not rotating, but formed and subsequently washed out in quasi-periodic manner similar like a transitory stall in 2D diffusers [98, 100]. However, the total calculation-time for the flow observation was too short (= five revolutions of the rotor = 0.125 s), and thus it was not possible to analyze the stall characteristics more in detail.
- (4) at $q_b^* = 0.60$ and 0.56: The flow pattern switching occurs at the impeller

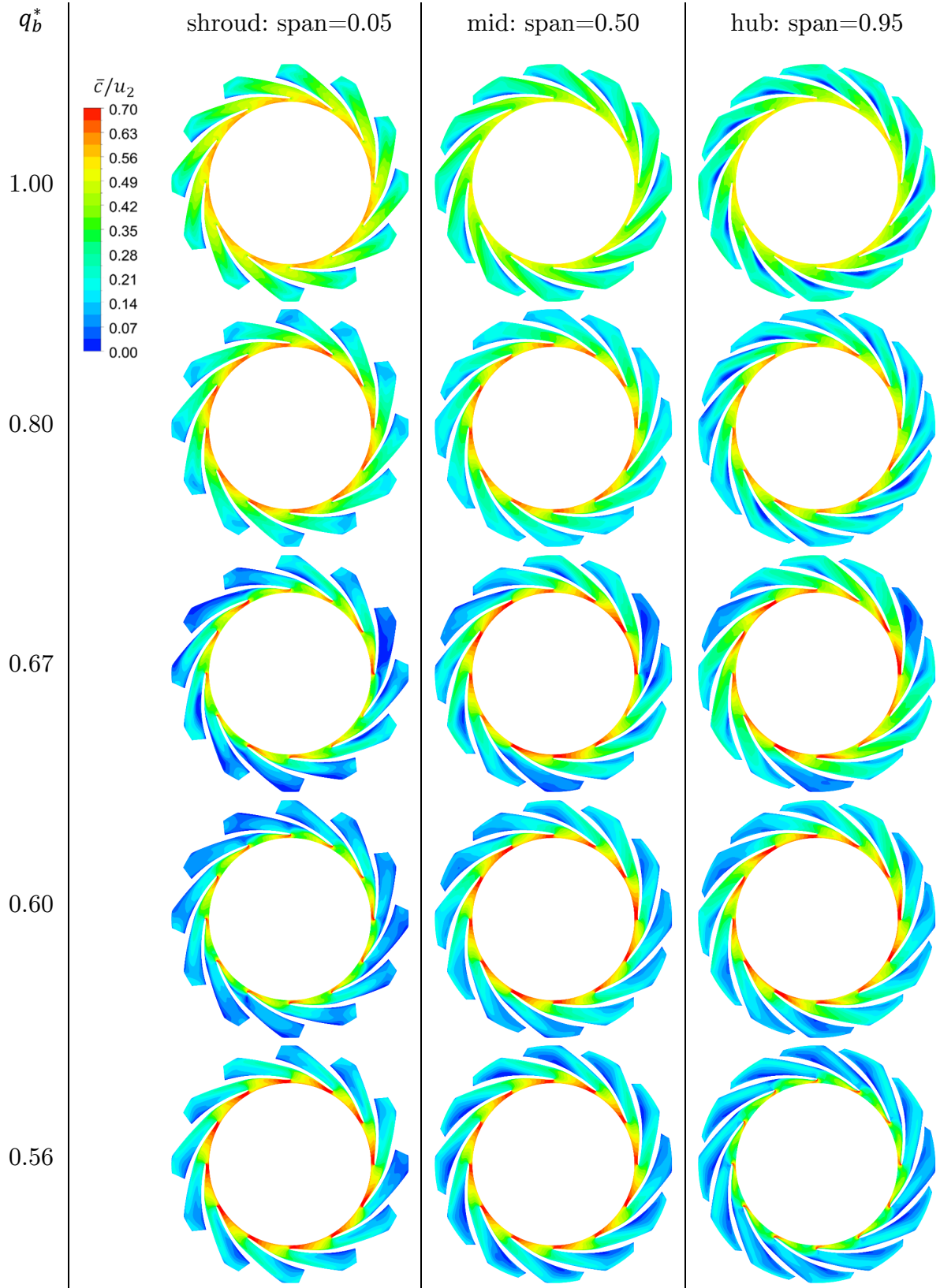


Figure 5.12: Dimensionless velocity contours in the 2nd stage diffuser of Test-05 from the CFD

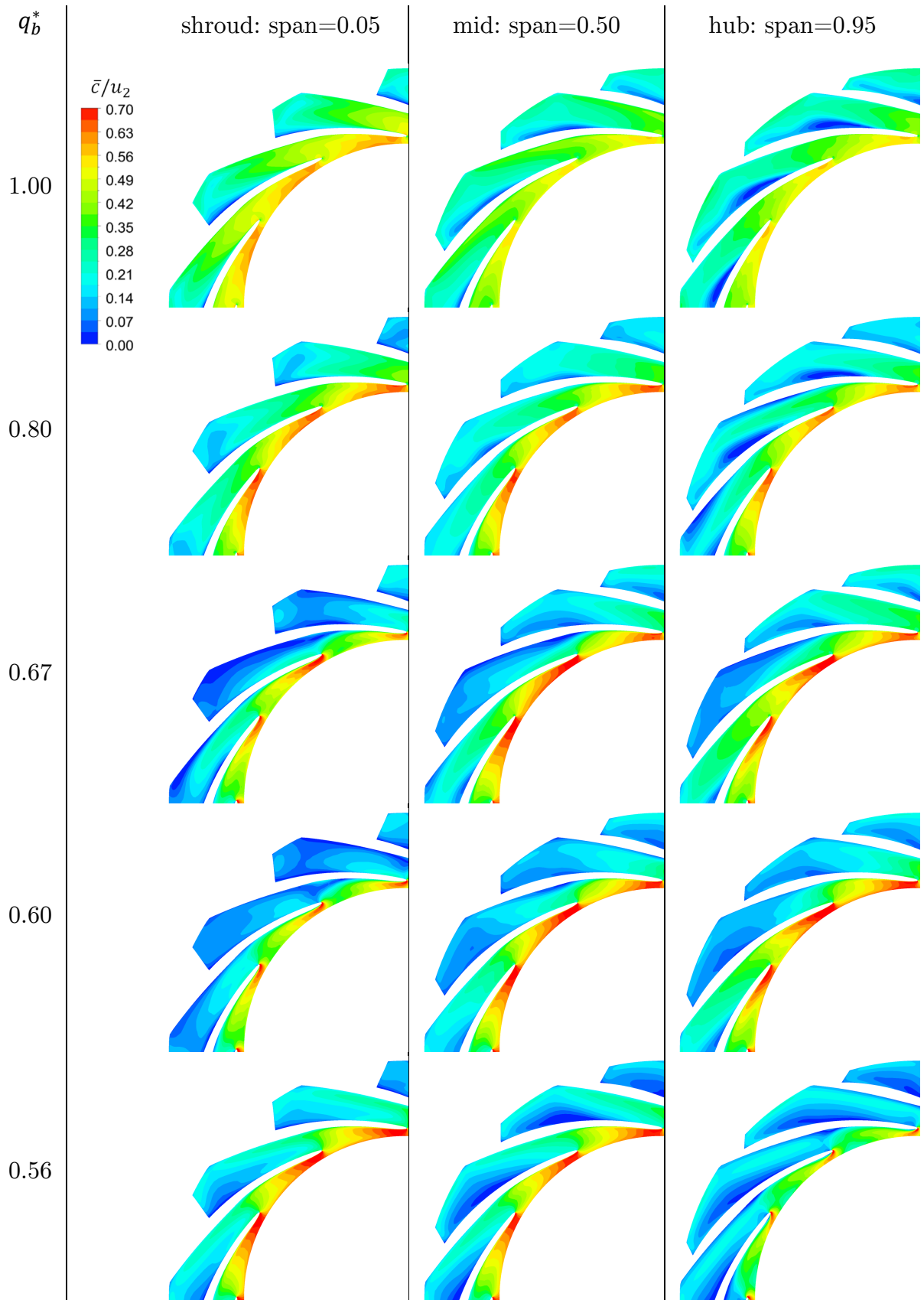


Figure 5.13: Close-up view of Fig. 5.12 between 9 and 12 o'clock position

outlet, which significantly affects velocity distributions in the diffuser. A sudden shift of the streamline is observed in the inlet triangular section. The highest velocity zone (red color) moves from the hub at $q_b^* = 0.60$ to the shroud at $q_b^* = 0.56$. In the same time, the major separation in the diffusing channels (deep blue color) occurs on the shroud at $q_b^* = 0.60$ and the hub at $q_b^* = 0.56$.

Based on a 2D diffuser study in [99], the stall position in the diffuser is largely affected by an inlet-velocity profile. When an inlet velocity with a stepped shape was provided in a 2D diffuser, stall always appeared on the low-velocity side wall. In the present study, the same tendency is observed from Figs. 10(a) and 5.13. The major stall in the diffusing channels (Fig. 5.13) always appears at the span position where the meridional velocity is low at the impeller outlet (Fig. 5.10(a)): shroud at $q_b^* = 0.60$ and hub at $q_b^* = 0.56$.

Figure 5.15 shows velocity contours at the diffuser inlet throat for different flow-rates. The transparent vane-passages indicate the shroud position (span = 0.05). Backflow zone (deep-blue color) is observed near the shroud at $q_b^* = 0.60$ and hub at $q_b^* = 0.56$. The flow patterns over the span at the inlet throat are qualitatively quite similar with those at the impeller outlet in Fig. 5.10(a), i.e. the skewed velocity-distributions at the impeller outlet reach the inlet throat and become inlet-velocity conditions for the diffusing channels.

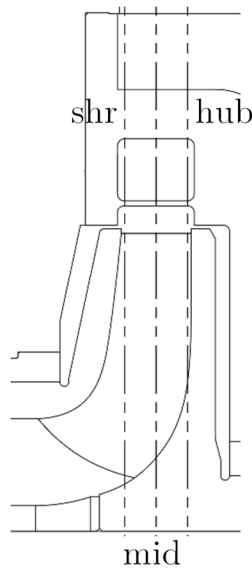


Figure 5.14: Span position definition for Fig. 5.12 and 5.13

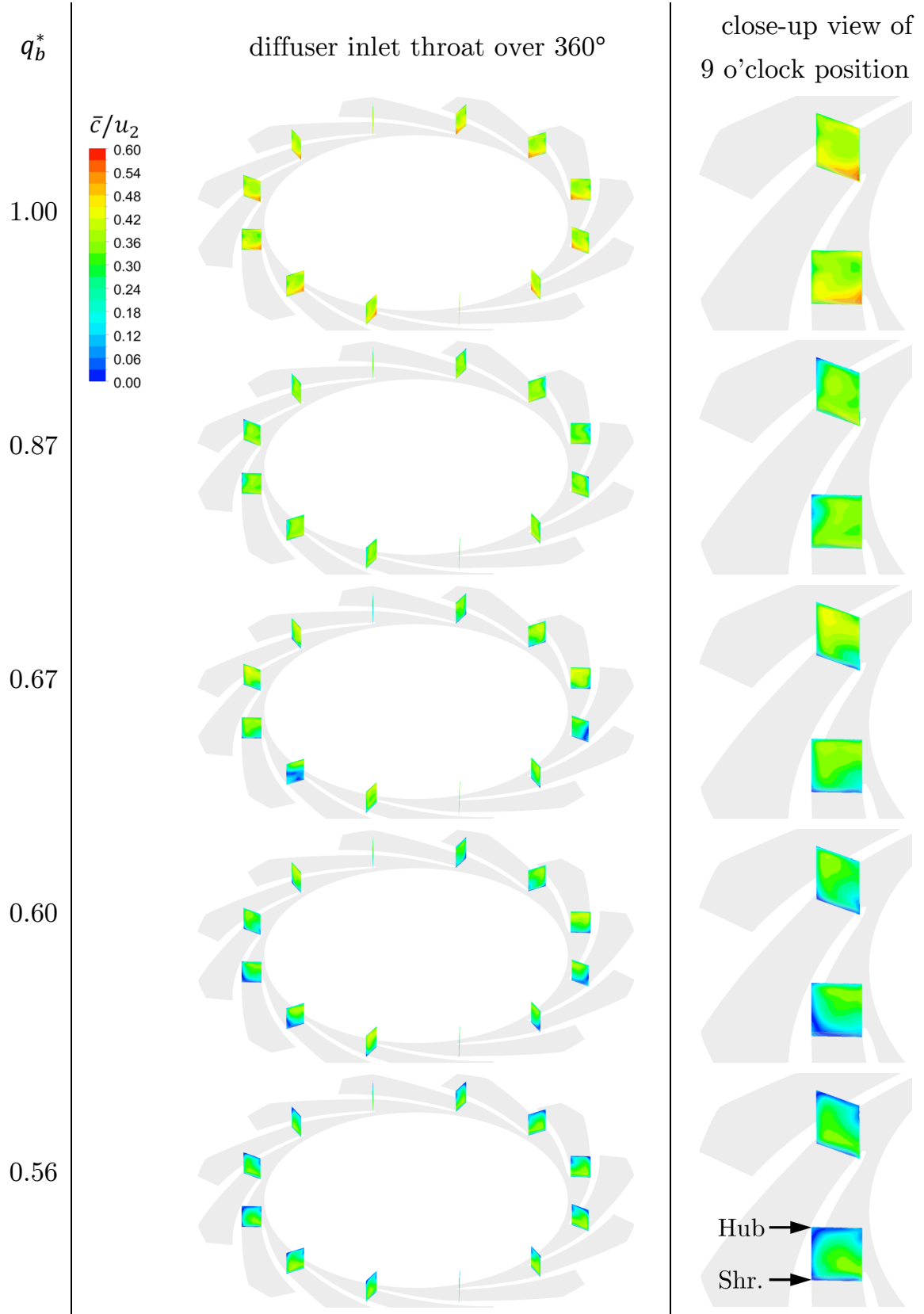


Figure 5.15: Dimensionless velocity contours at the diffuser inlet throat in the 2nd stage from the CFD of Test-05 (transparent light-grey color indicates the diffuser flow-passage near the shroud: span = 0.05)

5.3 Discussion

The previous chapters show that a flow phenomenon, which triggers the head-curve instability, is the flow pattern switching. However, the instability is a consequence of excessive head-loss at a certain flow-rate. Then, the correlation between the flow pattern switching and large head-loss needs to be explained.

The measured internal-head curves in Fig. 5.4 show that the influence of the flow pattern switching on head-loss in the impeller is limited. It is because the impeller experiences the streamline movement across the span only at the last small section (Fig. 5.11). The shifting streamline enters the inlet triangular section of the diffuser, resulting in a large momentum-exchange between streamlines (Figs. 5.12 and 5.13) and massive mixing-loss ($\psi_{s,3-3q}$ in Fig. 5.4). Eventually, it makes the stage-head curve unstable (ψ_{2nd} in Fig. 5.4). Note that the flow pattern switching has also a significant impact on velocity distributions in the diffusing channels (Figs. 5.12, 5.13 and 5.15), but $\psi_{s,3q-4q}$ continuously rises with decreasing flow-rate near the onset of the instability (Fig. 5.4). How can the same flow-phenomenon cause the *head-loss* in the inlet triangular section, but the *head-rise* in the diffusing channels? Some hints can be found in 2D diffuser studies [100–102]:

- (1) The optimal pressure-recovery in 2D diffusers occurs after the first *appreciable (intermittent or transitory) stall* appears on the diffuser wall [100, 101].
- (2) A higher turbulence-intensity at the diffuser inlet improves pressure-recovery in 2D diffusers [100, 102].

Figures 5.12 and 5.13 show that transitory flow-separation starts to appear in the diffusing channels at a (slightly) higher flow-rate than the onset of the instability. According to [8], the turbulence-intensity at the diffuser inlet tends to increase with decreasing flow-rate. These two mechanisms, the appreciable stall in the diffusing channels as well as the increased turbulence-intensity at the diffuser inlet, may be the reason why the pressure recovery in the diffusing channels increases at $q_b^* = 0.76 \sim 0.57$ in Figs. 5.4 and 5.5 while the flow pattern switching and head-curve instability occur.

It is worthwhile to discuss the stable head-curve in the last stage to understand the flow pattern switching and head-loss mechanism. Figure 5.2

shows that the series stages have the instability at $q_b^* = 0.67$, but the last stage gives a flat head-rise. The series and last stage are equipped with the same impeller, but different diffuser. Figure 5.16 depicts span-wise velocity distributions at the impeller outlet of the 2nd and 4th stage that were numerically estimated. The outlet-velocity profiles in both stages tend to vary in a similar manner along the operating points. The flow pattern switching is clearly detected in both. There is no measured internal-head curves in the last stage, and thus the occurrence of the flow pattern switching cannot be experimentally proved. However, if one assumes that the outlet-velocity profiles estimated by the numerical simulations are qualitatively reliable, Figs. 5.2 and 5.16 suggest that head-curve instability *does not* appear even though the flow pattern switching occurs in the last stage, i.e. the flow pattern switching is *not* a sufficient condition to produce the unstable head-curve. The head curve is likely to be unstable *only when* (1) the flow pattern switching occurs at a certain flow-rate *and* (2) the consequential head-loss in the inlet triangular section is larger than all head-rise generated by other hydraulic components at the same flow-rate. Then, why is the head-loss in the 4th stage smaller than that in the 2nd stage during the flow pattern switching? It is probably because of:

- (1) the larger Gap B ($\text{Gap B}_{\text{last stage}}/r_2 = 0.08$, and $\text{Gap B}_{2\text{nd}}/r_2 = 0.06$), and
- (2) a complex influence of the discharge casing on performance of the last stage diffuser.

Figure 5.17 shows velocity contours in the last diffuser, annular chamber and discharge casing at BEP. The velocity component was time-averaged during the last five revolutions of the shaft. The flow patterns in the last diffuser is very different with those in the 2nd stage in Figs. 5.12 and 5.13. The annular chamber collects fluid from the last-diffuser outlet over 360° and discharges it through the single discharge-nozzle located at 12 o'clock position. It creates non-axisymmetric pressure and velocity distribution around the circumference not only in the annular chamber, but also in the diffuser channels (and the impeller channels). As a result, pressure recovery and stall development in the last diffuser are different from those in the 2nd stage diffuser. In Fig. 5.17, fully developed separations are observed in some vane passages even though the operating flow-rate is BEP. It indicates that the loss mechanism in the last stage

cannot be explained only by the flow pattern switching at the impeller outlet. A further analysis of the last-stage performance is not carried out in the current work because experimental data of internal-head curves is not available and the quantitative accuracy of the present simulation results is not sufficient for this purpose.

In conclusion, Chapter 5 can be summarized as below:

- (1) The flow pattern switching at the impeller outlet is a trigger for the head-curve instability. It generates a large momentum-exchange between streamlines across the span in the inlet triangular section of the diffuser.
- (2) If the mixing-loss in the inlet triangular section is larger than all head-rise generated by other hydraulic components at the same flow-rate, the head curve becomes unstable.
- (3) However, if the loss is *not* large enough, the head-curve instability may not appear despite the occurrence of the flow pattern switching.

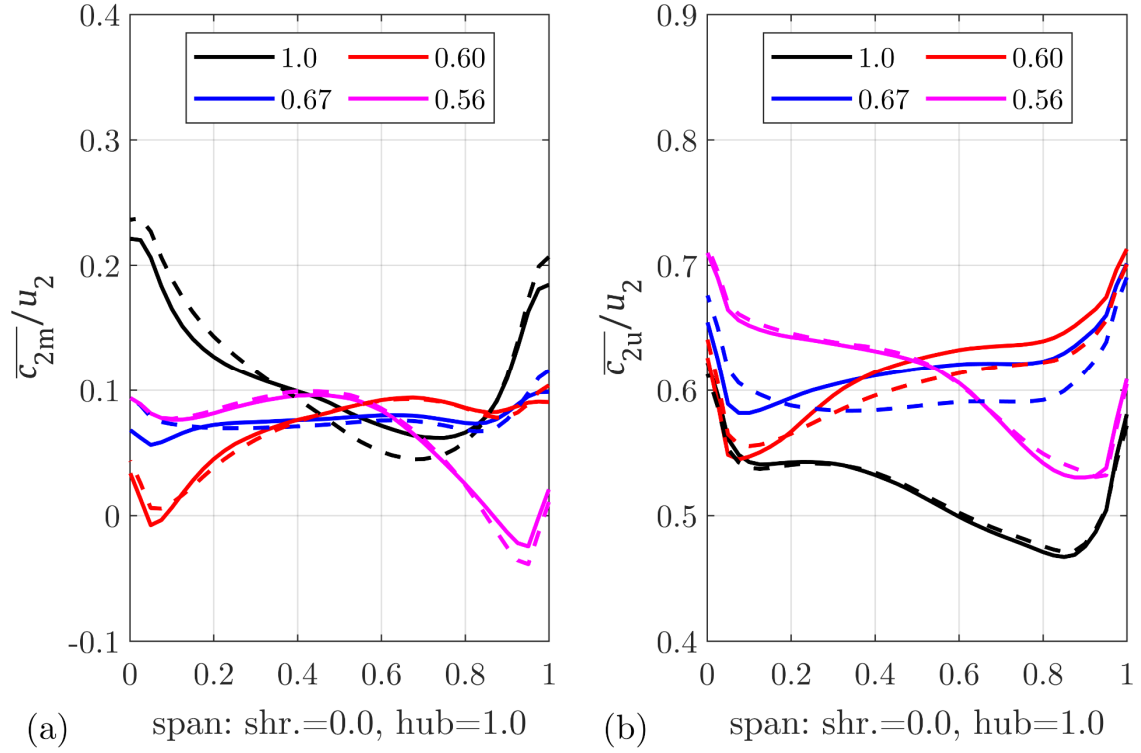


Figure 5.16: Span-wise velocity distribution at the impeller outlet in the 2nd and last stage from the CFD of Test-05; (a) meridional velocity, (b) circumferential velocity; color indicates q_b^* ; solid line – 2nd stage, dashed line – 4th stage

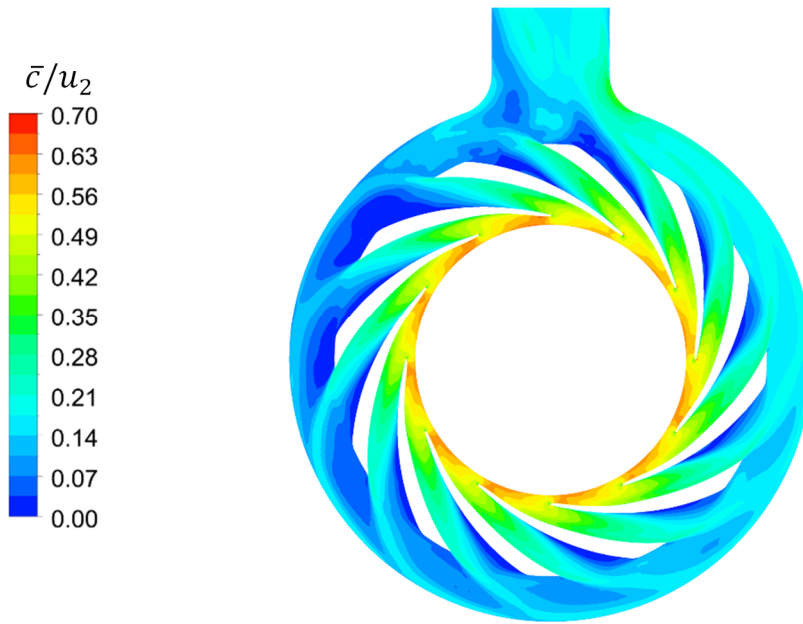


Figure 5.17: Dimensionless velocity contour in the last stage diffuser, annular chamber and discharge casing of Test-05 from CFD; mid-span; at BEP

6 Impact of Meridional Width and Width Ratio on Performance Curve and Pressure Pulsations

6.1 Effect of Meridional Width

The influence of meridional width on pump performances is investigated by varying b_2^* and b_3^* at a constant $b_3/b_2 = 1.1$. The test program and sectional drawings are presented in Fig. 1.2 and Table 1.1. Test-01 corresponds to the largest width with the smallest blade-angle at the impeller outlet and diffuser inlet, and Test-06 the smallest width with the largest angle. Since the interaction between main flow at the impeller outlet and side flow in the ISR affects pump

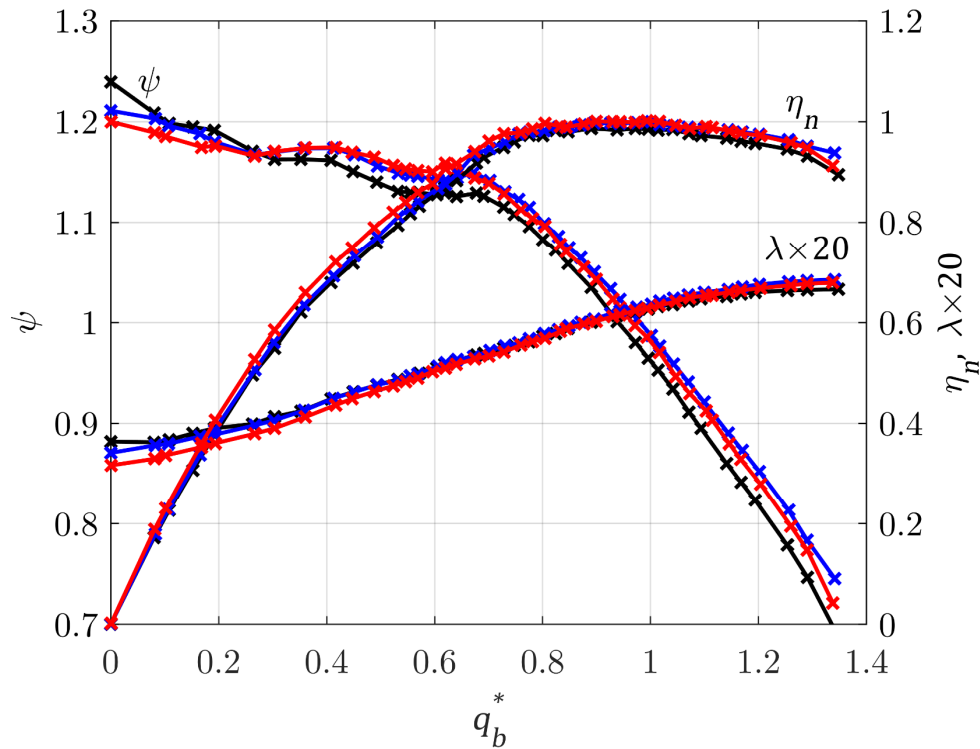


Figure 6.1: Overall-performance curves of different meridional-widths from the measurement; Test-01 – black, Test-05 – blue, Test-06 – red

performances [1, 25, 26], Gap A and x_{ov} were designed to be constant in all test configurations. Figure 6.1 shows measured overall-performance curves of Test-01, 05 and 06. The black, blue and red line represent the largest, middle, and smallest b_2^* , respectively. Three designs have the identical BEP flow-rate, but their n_q are slightly different as 30, 29.6 and 29.5 for the largest, middle and smallest b_2^* , respectively. The largest b_2^* gives around 1% lower efficiency than the others. Table 6.1 summarizes the main performance data of the three tests. It is interesting that the efficiency curve becomes flatter near BEP with decreasing b_2^* , i.e. the pump can run with a higher efficiency over a wider operating-range when the meridional width becomes narrower. In case of the smallest b_2^* , a sudden drop of head and efficiency is observed at $q_b^* = 1.35$, but it has nothing to do with the hydraulic design. The suction pressure during the test was not high enough, and thus the 1st stage impeller ran under a condition of $NPSH_{av} < NPSH_{3\%}$. At shut-off, a larger meridional-width consistently produces a higher head and power, which demonstrates that outlet recirculation becomes stronger with increasing b_2^* [1, 3, 17]. Surprisingly, the meridional width does not have a large effect on the head-curve instability. All tests show the onset flow-rate of the instability in a range of $q_b^* = 0.62 \sim 0.68$.

The influence of b_2^* on the head curve is further analyzed using measured internal-head curves in the 2nd stage in Fig. 6.2:

- (1) The onset of the instability in the 2nd stage head curve (ψ_{2nd}) does not vary

Table 6.1: Main performance data of Test-01, 05 and 06

	Test-01	Test-05	Test-06
$b_{2,series}^*$	0.086	0.078	0.071
$q_{b,opt}^*$	1	1	1
ψ_{opt}	0.97	0.99	0.99
$\eta_{n,opt}$	0.99	1	1
λ_{opt}	0.0314	0.0318	0.0314
n_q	30	29.6	29.5
ψ_0	1.24	1.21	1.20
λ_0	0.018	0.017	0.016

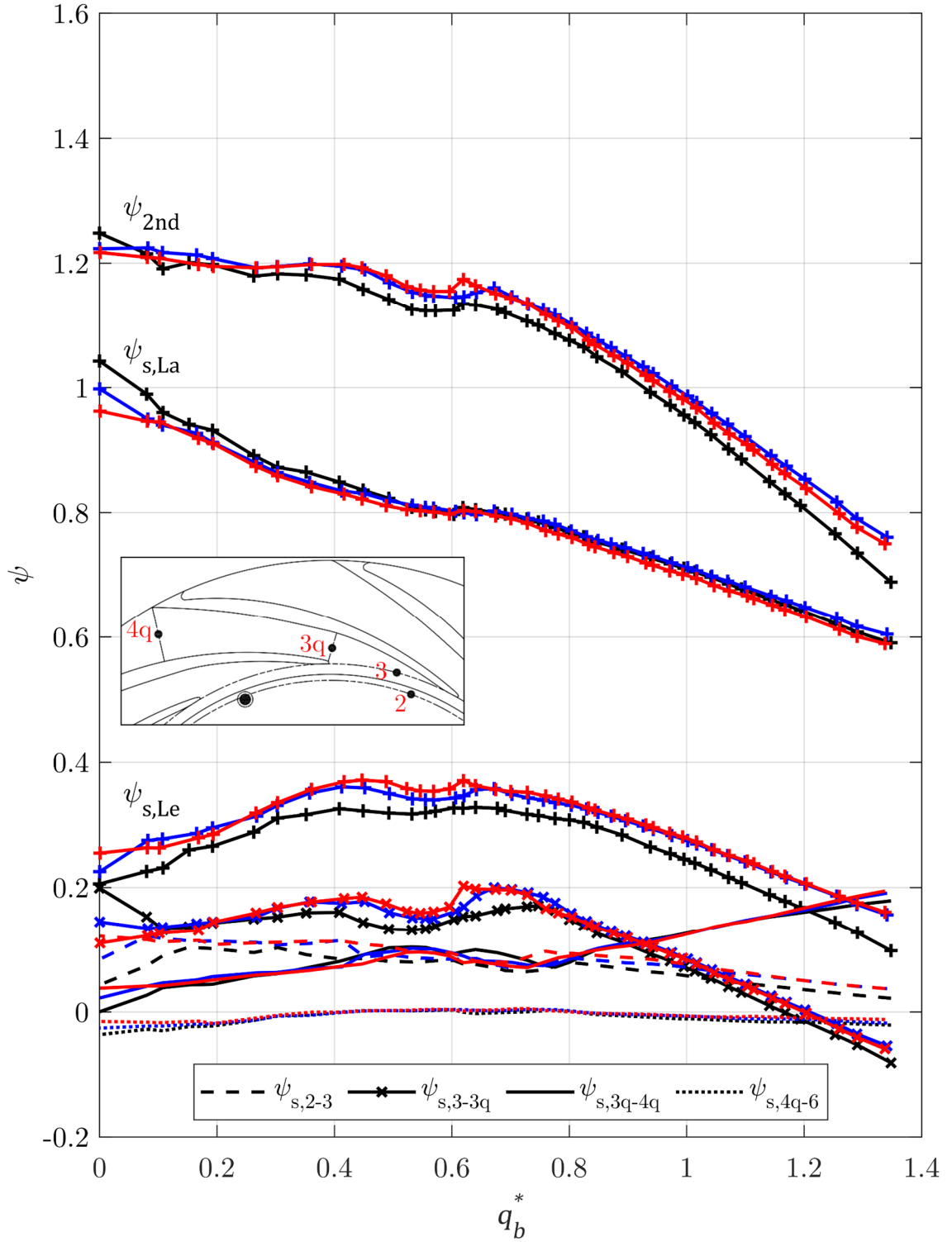


Figure 6.2: 2nd stage internal-head curves of different meridional-widths from the measurement; Test-01 – black, Test-05 – blue, Test-06 – red

systematically with the meridional width. The largest and smallest b_2^* give the instability at $q_b^* = 0.62$, but the middle b_2^* at $q_b^* = 0.67$.

- (2) The static-head rise in the impeller ($\psi_{s,La}$) is similar in all tests above the onset of the instability. However, once flow recirculation appears at the impeller outlet, a larger b_2^* tends to form a stronger recirculation and results in a higher head-generation in the impeller.
- (3) The largest meridional-width gives a noticeably low pressure-recovery in the diffuser ($\psi_{s,Le}$) over the whole flow-range compared to the others. It has something to do with poor flow-quality at the impeller outlet of the largest b_2^* . Details will be discussed following in this chapter.
- (4) The excessive head-loss in the inlet triangular section ($\psi_{s,3-3q}$) is responsible for the instability of the stage-head curve for the smallest and middle b_2^* . However, this tendency is not consistent for the largest b_2^* . Probably, it is due to measurement uncertainty of the internal-head curves. In the current study, the internal pressures were measured at two or three different circumferential-positions at each evaluation station. The measurement

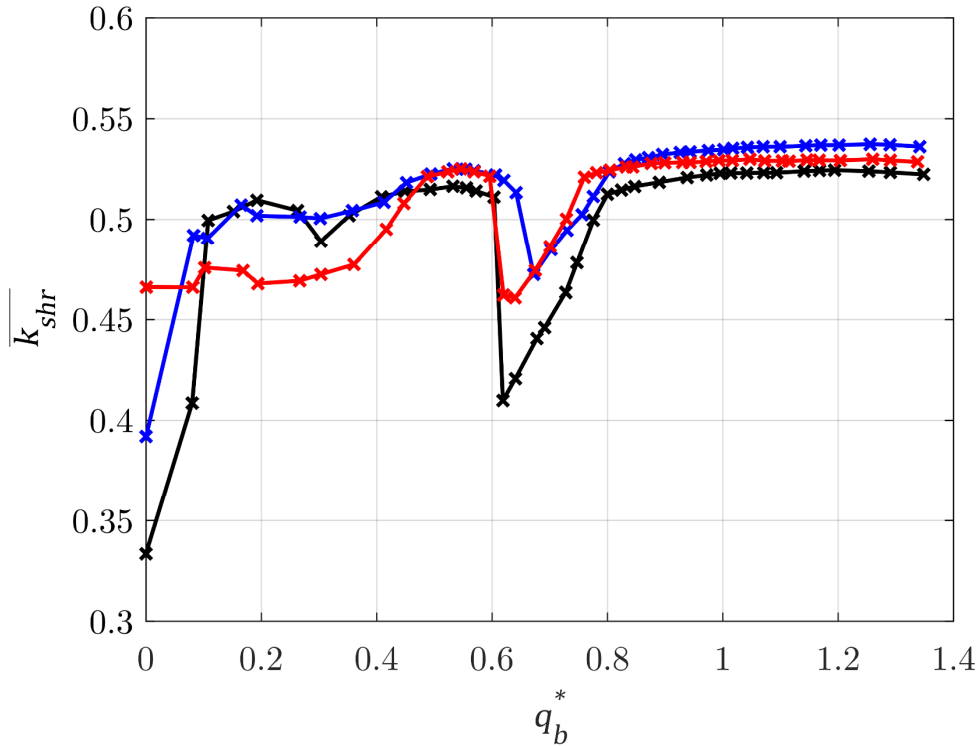


Figure 6.3: Average rotation factors on the front ISR in the 2nd stage from the measurement; Test-01 – black, Test-05 – blue, Test-06 – red

outputs may not be always representative of the performance in the whole channel when the pump runs at reduced flow-rates.

- (5) The pressure recovery in the diffusing channels ($\psi_{s,3q-4q}$) of three meridional-widths is quite similar in most flow-rates – except near the onset of the instability and at shut-off. The same trend is observed for $\psi_{s,4q-6q}$. It may imply that Gap B and inlet triangular section largely smooth out differences of flow patterns at the impeller outlet generated by the different b_2^* . Accordingly, the velocity profile at the inlet throat becomes similar, resulting in a similar $\psi_{s,3q-4q}$ and $\psi_{s,4q-6q}$ in all cases.

Figure 6.3 shows average rotation factors of the three meridional-widths based on the experiments. A systematic trend is observed in all tests: $\overline{k_{shr}}$ drops near $q_b^* = 0.8$, becomes minimum at the onset of the instability, and sharply rises at a further reduced flow-rate. As described in Chapter 5, the sudden change of $\overline{k_{shr}}$ is most likely to indicate the occurrence of the flow pattern switching at the impeller outlet. Outlet recirculation appears near the shroud at the instability, and fluid with very low c_{2u} is drawn from the diffuser to front ISR. It changes the pressure distribution in the side room and leads to the minimum $\overline{k_{shr}}$. At a slightly reduced flow-rate, flow recirculation at the impeller outlet moves from the shroud to hub. Then, fluid with high c_{2u} , which comes out of the impeller blades, enters again the front ISR, and $\overline{k_{shr}}$ is recovered back to the normal level. The flow pattern switching causes an excessive head-loss in the inlet triangular section, and consequently makes the head-curve unstable as seen in Fig. 6.2. These findings suggest that the meridional width is *not* an effective design-parameter to control the flow pattern switching and head-curve instability. It is opposite to the previous suggestion by Schill that a smaller b_2^* may stabilize the head-curve [6]. Figure 6.3 shows that the largest b_2^* generates a deep drop in $\overline{k_{shr}}$ at the onset of the instability. A large variation of pressure profiles in the side room causes a significant fluctuation of the axial thrust of the rotor that is not recommendable for any multistage pump.

Figure 6.4 compares meridional-velocity distributions at the 2nd stage impeller outlet of the different b_2^* . The velocity profiles were estimated by CFD simulations. The black solid, blue dashed and red dotted line represent the largest, middle and smallest b_2^* , respectively. The meridional velocity was time-

averaged during the last five revolutions of the impeller, and then circumferentially area-averaged at each span position. All meridional-widths generate qualitatively similar flow-patterns at the impeller outlet. Two major streamlines are formed near the shroud and hub, and the lowest velocity appears near the dimensionless span = 0.8. A quantitative analysis is carried out based on the normalized standard deviation σ_n (= standard deviation/mean over the span) to evaluate the span-wise uniformity of the velocity profiles. The largest, middle and smallest width give $\sigma_{n,\overline{c_{2m}}/u_2}$ of 0.46, 0.40, and 0.39, respectively. It means that the meridional-velocity uniformity of the largest impeller is not as good as that of the middle and smallest one, which is the reason why the pressure recovery in Gap B and inlet triangular section in the largest b_2^* is so low compared to the others in Fig. 6.2. The middle and smallest b_2^* have the similar $\sigma_{n,\overline{c_{2m}}/u_2}$, which gives a similar level of $\psi_{s,2-3}$ and $\psi_{s,3-3q}$. Figures 6.1 ~ 6.4 suggest that the largest b_2^* is not the optimum design for the present specification.

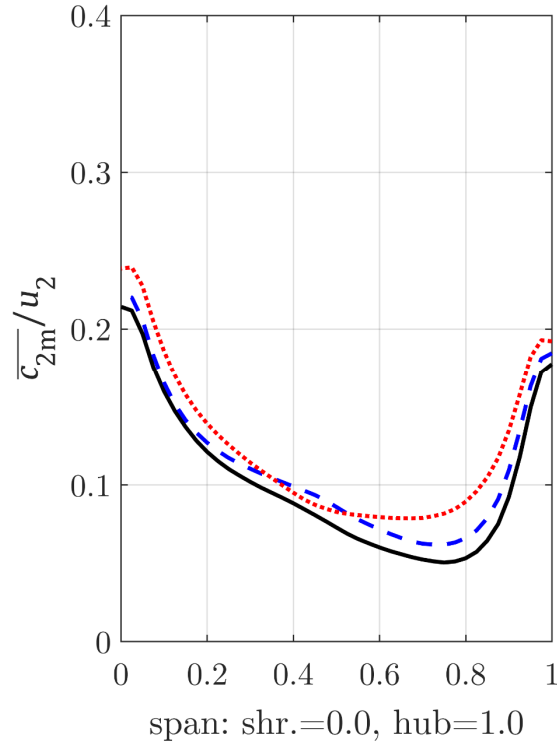


Figure 6.4: Dimensionless meridional-velocity distribution in the span-wise direction at the 2nd stage impeller outlet from the CFD at BEP; Test-01 – black, Test-05 – blue, Test-06 – red

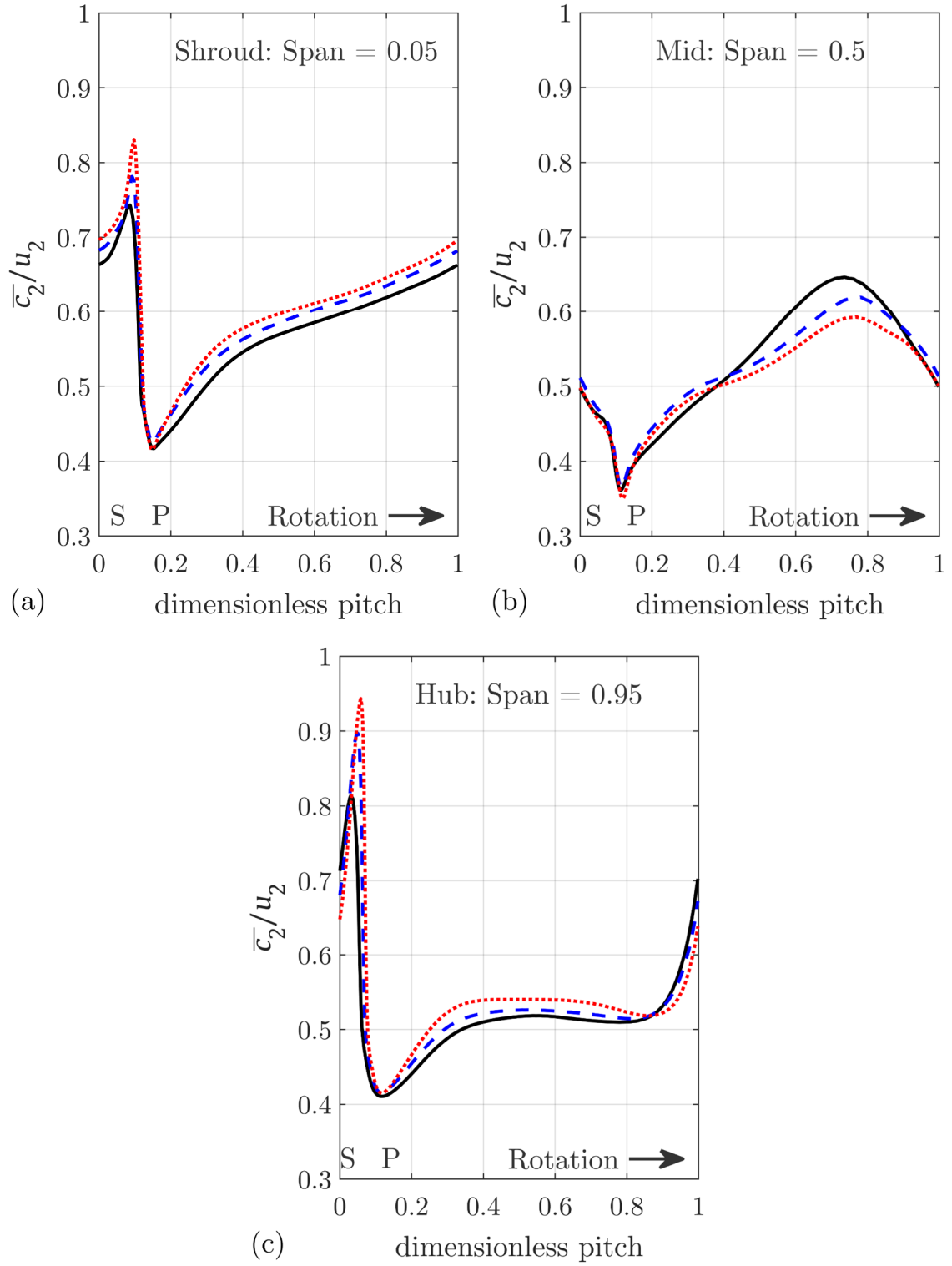


Figure 6.5: Dimensionless absolute-velocity distribution in the pitch-wise direction at the 2nd stage impeller outlet from the CFD at BEP; Test-01 – black, Test-05 – blue, Test-06 – red; P – Pressure side, S – Suction side of the impeller blade trailing edge

Figure 6.5 compares outlet-velocity distributions in the pitch-wise direction of the different b_2^* . Three span positions are depicted. The absolute velocity was time-averaged during the last five revolutions of the shaft. Flow quality over the impeller circumference is quantitatively assessed based on the peak-to-peak value of \bar{c}_2/u_2 by (Gl. 4-3). The impeller with a smaller b_2^* was designed to have a larger β_2 to keep a constant head-coefficient. (Unfortunately, the realized head of the three impellers is slightly different from each other as seen in Fig. 6.1 due to the uncertainty of predicting the hydraulic efficiency and slip factor in the design process.) Therefore, the peak-to-peak value of \bar{c}_2/u_2 is likely to increase with decreasing b_2^* . Figure 6.5 shows that this hypothesis is partly correct. A smaller meridional-width produces a higher peak-to-peak velocity at the shroud and hub in Fig. 6.5(a) and (c), respectively. However, the peak-to-peak velocity *decreases* with decreasing b_2^* at the mid span in Fig. 6.5(b). This inconsistency might have something to do with the fact that the outlet-velocity distributions are affected by many geometric parameters [3, 103]. It would not be always possible to explain all changes of the outlet-flow patterns based on just a single

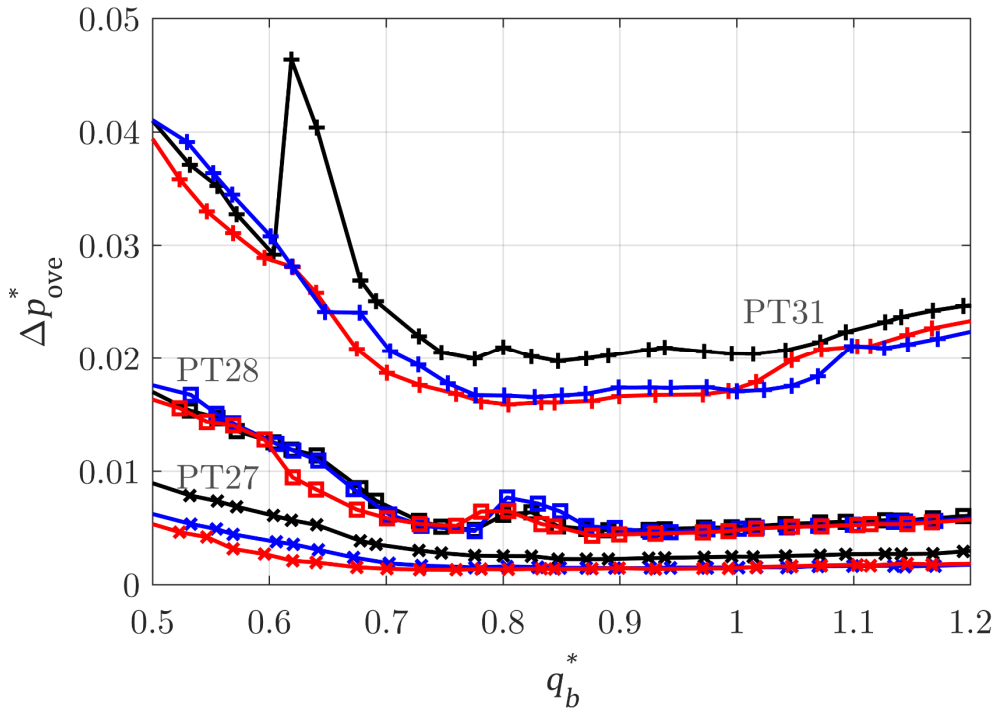


Figure 6.6: Overall RMS values of dimensionless pressure-pulsations measured at the suction nozzle (PT27), discharge nozzle (PT28) and diffuser inlet in the 2nd stage (PT31); black – Test-01, blue – Test-05, red – Test-06

design parameter, i.e. b_2^* .

Figures 6.4 and 6.5 show that flow quality at the impeller outlet tends to vary (in some extent) in a counter-acting manner in the span-wise and pitch-wise direction as the meridional width decreases. Then, there would be an *optimum* b_2^* to minimize pressure-pulsations in a given specification. Figure 6.6 depicts overall RMS values of dimensionless pressure-pulsations for the different b_2^* . All data are from the experiments. The measurement positions are the suction nozzle, discharge nozzle, and diffuser inlet in the 2nd stage (see Fig. 2.2 and Table 2.2 for details). The black, blue and red line indicate the largest, middle and smallest meridional-width, respectively. At the diffuser inlet, the largest b_2^* creates the strongest pressure-pulsations at $q_b^* > 0.6$. Δp_{ove}^* is significantly reduced at the middle and smallest b_2^* (by as much as 16.5% at BEP) above the onset flow-rate of outlet recirculation. At the discharge nozzle, the pressure pulsations are marginally affected by the meridional width. At the suction nozzle, the strongest pressure-pulsations are again observed in the largest width. This result suggests that the pressure pulsations are affected by the

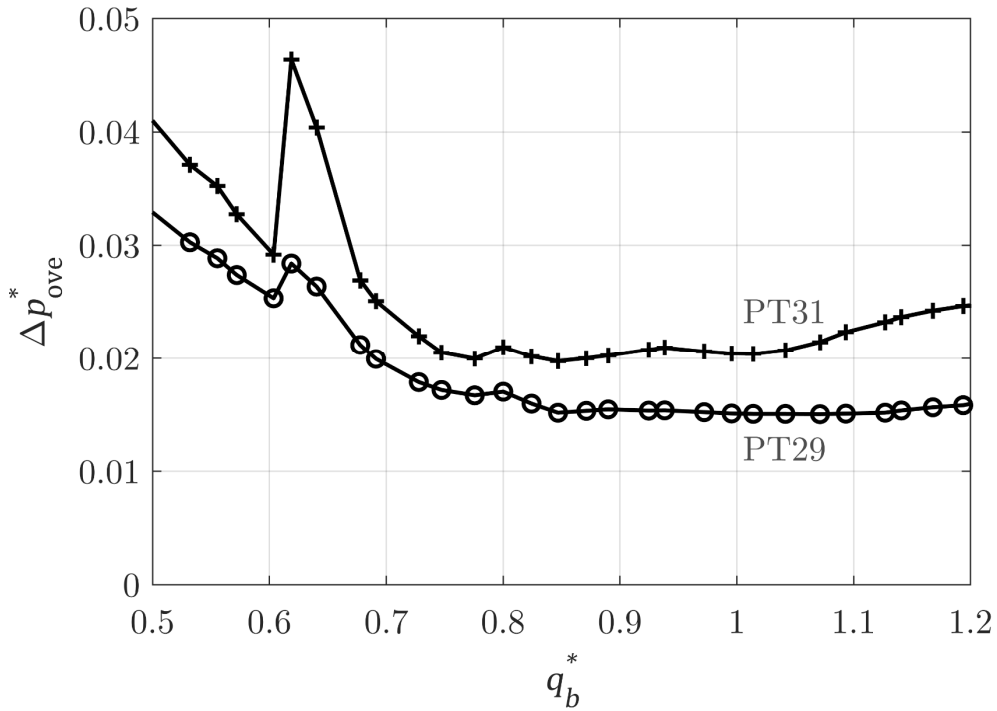


Figure 6.7: Overall RMS values of dimensionless pressure-pulsations measured at the front ISR at d_2 (PT29) and diffuser inlet (PT31) in the 2nd stage of Test-01

meridional width, and the middle and smallest b_2^* is likely to be the optimum design for the current project. It is noticeable that the largest meridional-width produces a sharp rise in Δp_{ove}^* at the onset flow-rate of the head-curve instability. Figure 6.7 shows that the peak in Δp_{ove}^* is also detected in the front ISR. Its intensity is largely reduced in the side room, indicating that (1) a flow motion causing the strong pressure-pulsation at the onset of the instability occurs in the main flow-passage, and (2) the tight Gap A and long x_{ov} (=a small gap passages between shroud plates of the impeller and diffuser) effectively suppress the transmission of the hydraulic excitation from the main flow to side-room flow.

The cause of the abrupt rise in Δp_{ove}^* is investigated in the frequency domain. Figure 6.8 shows spectra of dimensionless pressure-pulsations measured at the diffuser inlet for the largest width. The abscissa of upper figure is $f/f_n = 0.0025 \sim 42$, and that of lower one is $f/f_n = 0.0025 \sim 1.1$. Measurement results at some representative flow-rates are presented. When the pump operates at BEP and $q_b^* = 0.75$, a typical pattern of the pressure-pulsation spectra is observed. There are dominant peaks at VPF and its super-harmonics. At the onset of the instability ($q_b^* = 0.62$), a distinct and strong peak is detected at a very small frequency around $f = 1.17$ Hz ($f/f_n = 0.029$). Its amplitude is even higher than that at VPF and its integer multiples. At a further reduced flow-rate, this unusual peak is not observed any more.

A coherence between PT29 and PT31 is calculated to identify the slow flow-motion that is responsible for the sudden rise in Δp_{ove}^* at the instability. The coherence is determined by $|W_{AB}(f)|^2 / (W_{AA}(f)W_{BB}(f))$ where W is the power spectral density function, the subscript A is PT29, and the subscript B is PT31 [58]. A linear relation between two signals can be assessed by the coherence in a scale from zero (=no relation) to one (=linear system). Figure 6.9 shows that the pressure pulsations measured at PT29 and PT31 have a strong correlation at $f = 1.17$ Hz. Because the two sensors are located in different circumferential positions, this result indicates that a rotating stall appears when the pump with the largest meridional-width runs at the onset of the instability.

The real-time data of the pressure-pulsations at the diffuser inlet was averaged over every rotation of the shaft by (Gl. 4-13), and plotted against the number of shaft revolutions in Fig. 6.10. During the first 400 rotations, 11 cycles

of $\widetilde{\Delta p}^*$ are observed from 4th to 380th revolutions. Considering the mean rotational-frequency of the test of 39.97 Hz, the dominant pressure-fluctuation in Fig. 6.10 is equivalent to 1.17 Hz, i.e. a very slow rotating-stall appears in the diffuser.

Even though the head-curve instability is observed in all meridional-widths in a range of $q_b^* = 0.62 \sim 0.67$, only the largest width generates the diffuser rotating-stall and a sharp rise in Δp_{ove}^* at the onset of the instability. It suggests that:

- (1) The head-curve instability is *not* necessarily accompanied by the rotating stall.
- (2) The instability does not always produce a strong pressure-pulsation.

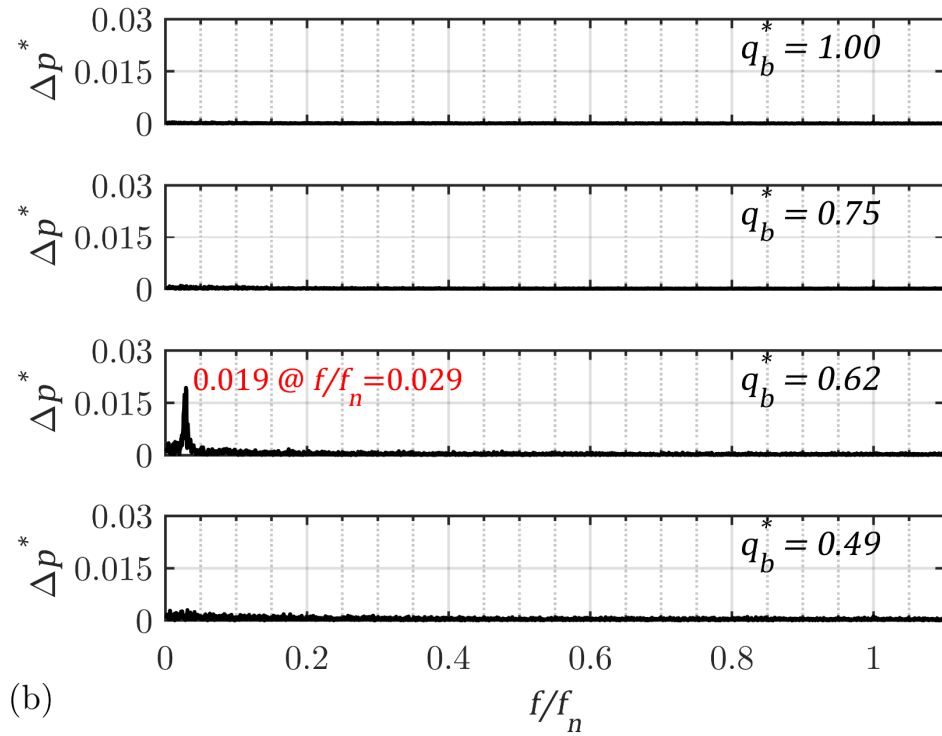
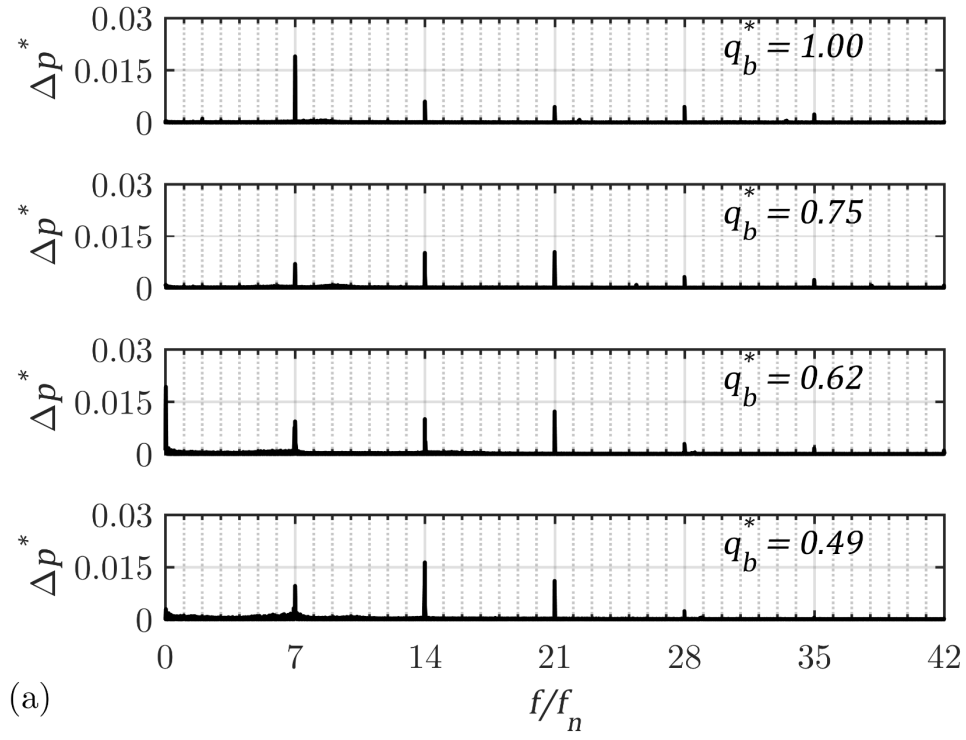


Figure 6.8: Spectra of dimensionless pressure-pulsations measured at PT31 in Test-01 for different flow-rates (ordinate = zero-to-peak amplitude): (a) $f/f_n = 0.0025 \sim 42$, (b) zoom-in $f/f_n = 0.0025 \sim 1.1$

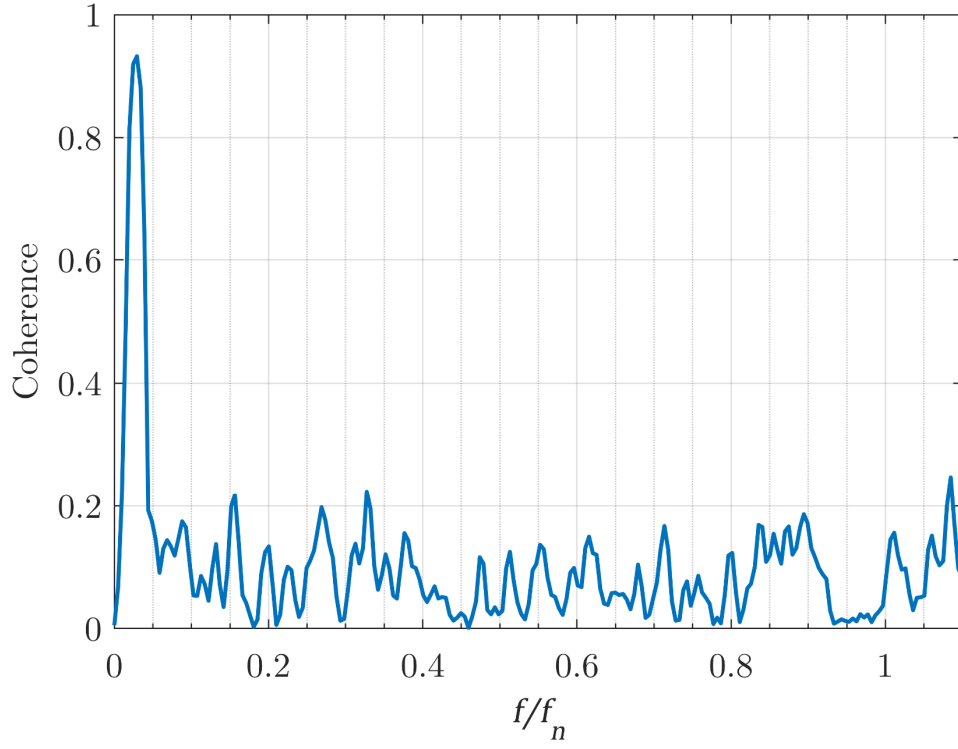


Figure 6.9: Coherence between PT29 and PT31 of Test-01 at $q_b^* = 0.62$

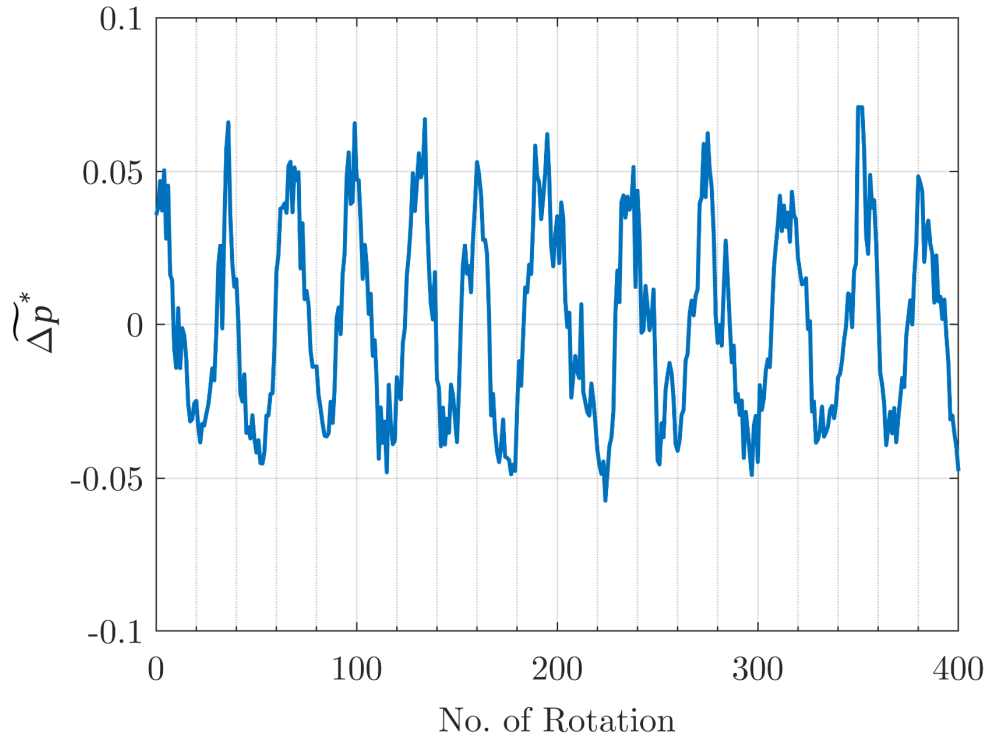


Figure 6.10: Dimensionless pressure-pulsations at PT31 averaged over each impeller revolution of Test-01 at $q_b^* = 0.62$

6.2 Uncertainty in CFD Prediction of Pressure Pulsations

Recently, CFD simulations have been adopted to investigate the effect of a change of geometrical parameters on pressure pulsations [105, 106]. This chapter evaluates the uncertainty in the CFD prediction of pressure pulsations using experimental data and numerically predicted data in the 4-stage model pump.

Figure 6.11 compares measured and predicted Δp_{ove}^* at various positions and different flow-rates. Each sensor is depicted in different colors. The solid line is experimental output and the dotted line is simulation data. The hydraulic configuration of the model pump is Test-05. The prediction uncertainty significantly varies with the sampling position and operating flow-rate:

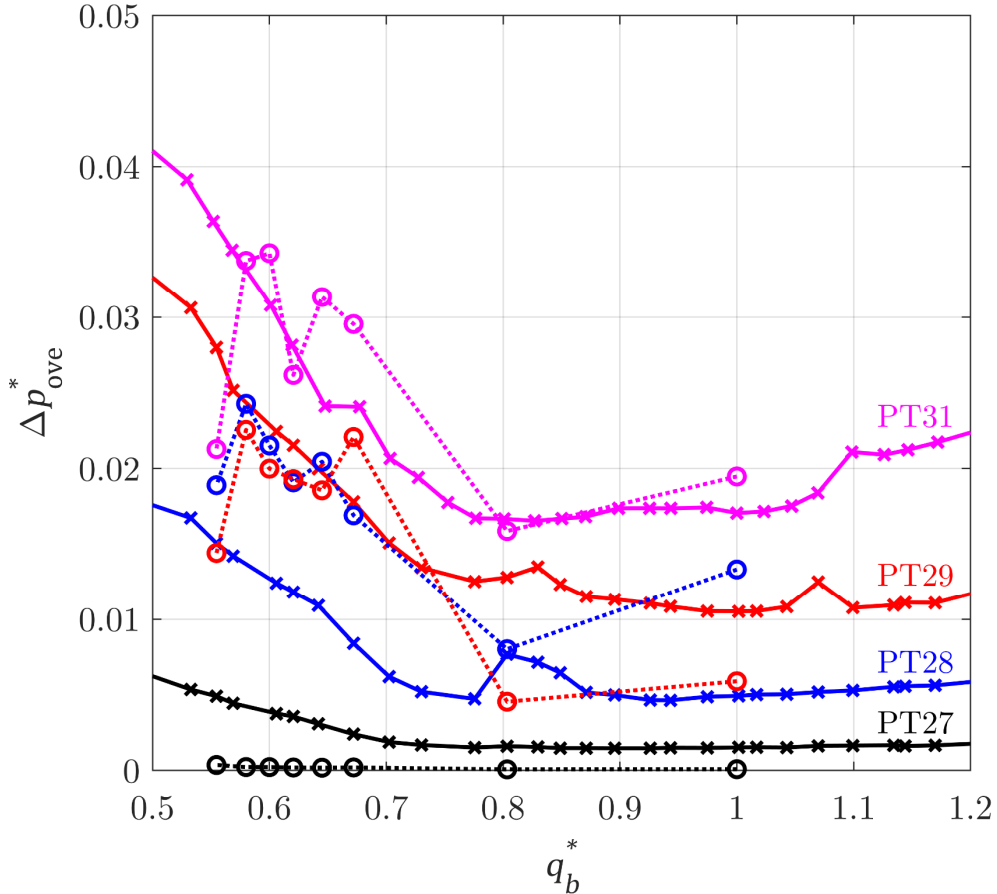


Figure 6.11: Overall RMS values of dimensionless pressure-pulsations of Test-05; measurement – solid line with \times , CFD – dotted line with \circ ; color indicates different sensor-positions in the multistage pump

- (1) At the suction nozzle (PT27): The predicted Δp_{ove}^* are so small over the whole flow-range that has little practical-value.
- (2) At the discharge nozzle (PT28): The pressure pulsations are largely over-predicted for most flow-rates. The deviation between the prediction and measurement is as much as 170% at BEP.
- (3) At the front ISR at d_2 in the 2nd stage (PT29): The prediction accuracy is not satisfactory near BEP ($\Delta p_{\text{ove,CFD}}^* / \Delta p_{\text{ove,Test}}^* - 1 = -43\%$ at BEP), but fairly good near $q_b^* = 0.60$. However, the improved accuracy at part-load seems a coincidence.
- (4) At the diffuser inlet in the 2nd stage (PT31): A decent agreement is observed between the prediction and test. The deviation is only 14% at BEP and does not exceed 30% at $q_b^* > 0.58$.

Similar results can be found in other studies [87, 104, 106] that the prediction uncertainty in pressure pulsations is significantly affected by the sampling location. The best prediction-accuracy is likely to be achieved (1) when the sampling is done in the main flow passage near the impeller outlet and diffuser inlet, and (2) the operating flow-rate is larger than the onset of outlet recirculation. A recent internal study in TU Kaiserslautern showed a substantial impact of the near-wall mesh quality on the prediction accuracy in pressure pulsations. A further investigation is necessary in a future project.

Figure 6.12 shows spectra of dimensionless pressure-pulsations at the diffuser inlet. The blue solid line represents the measured data and the red dotted line the predicted data. The upper figure is at BEP and the lower one at $q_b^* = 0.67$. Despite the decent prediction-accuracy of Δp_{ove}^* at the diffuser inlet (Fig. 6.11), the amplitude of each spectrum is significantly different between the prediction and test. Especially, the CFD simulation largely over-estimates the amplitude at VPF. A poor prediction-accuracy is observed in the sub-synchronous frequency ranges ($f/f_n < 1.0$), which might have something to do with the limited frequency-resolution in the CFD simulation, i.e. the total calculation-time is too short.

Figure 6.13 compares a variation of Δp_{ove}^* depending on the meridional width. The sampling position is the diffuser inlet. The test data (solid lines with empty symbols) are presented for the whole flow-range, and the predicted data (dotted

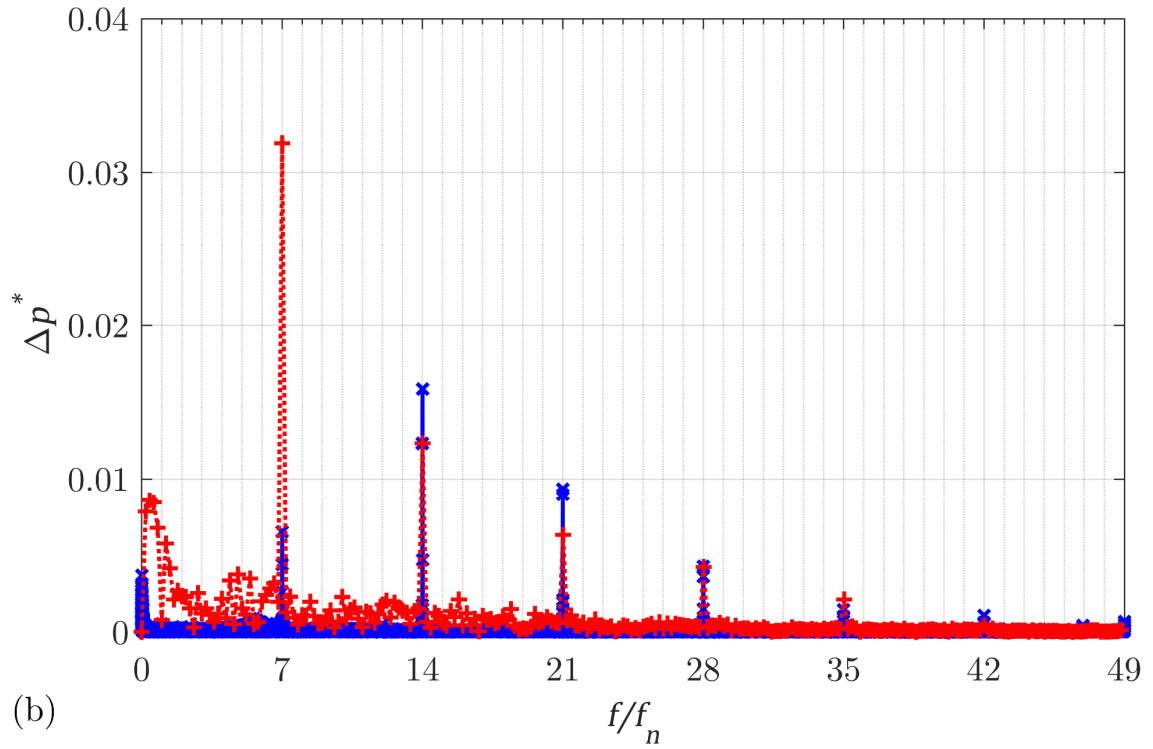
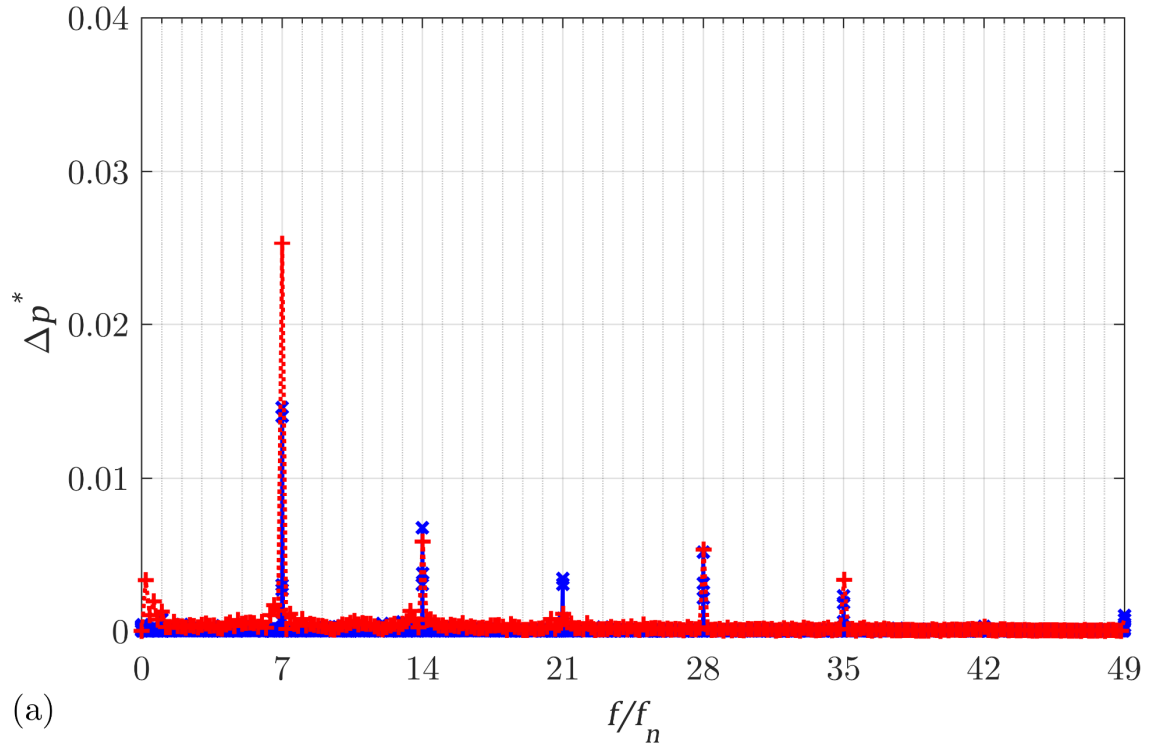


Figure 6.12: Spectra of dimensionless pressure-pulsations at PT31 of Test-05 (ordinate = zero-to-peak amplitude); (a) $q_b^* = 1.0$, (b) $q_b^* = 0.67$; measurement – blue solid line with \times , CFD – red dotted line with $+$

lines with filled symbols) are available only at $q_b^* = 1.0$ and 0.67 . The black, blue and red color indicate the largest, middle and smallest b_2^* , respectively.

- (1) At BEP, the estimated tendency of Δp_{ove}^* variation for the different b_2^* is in an agreement with the measurement results in some extent. The CFD simulation predicts the strongest pressure-pulsations in the largest width, which is correct. It estimates the lowest Δp_{ove}^* in the middle b_2^* , but the measurement output shows the same level of Δp_{ove}^* in the middle and smallest b_2^* . All pressure-pulsations are slightly over-predicted by the numerical simulations, but the maximum deviation is smaller than 20%.
- (2) At part-load ($q_b^* = 0.67$): The CFD simulation estimates a *completely wrong trend* of Δp_{ove}^* variation depending on b_2^* . The measured pressure-pulsations decrease with decreasing meridional-width. However, the predicted results are exactly opposite.

In general, pressure pulsations are more important at part-load than BEP

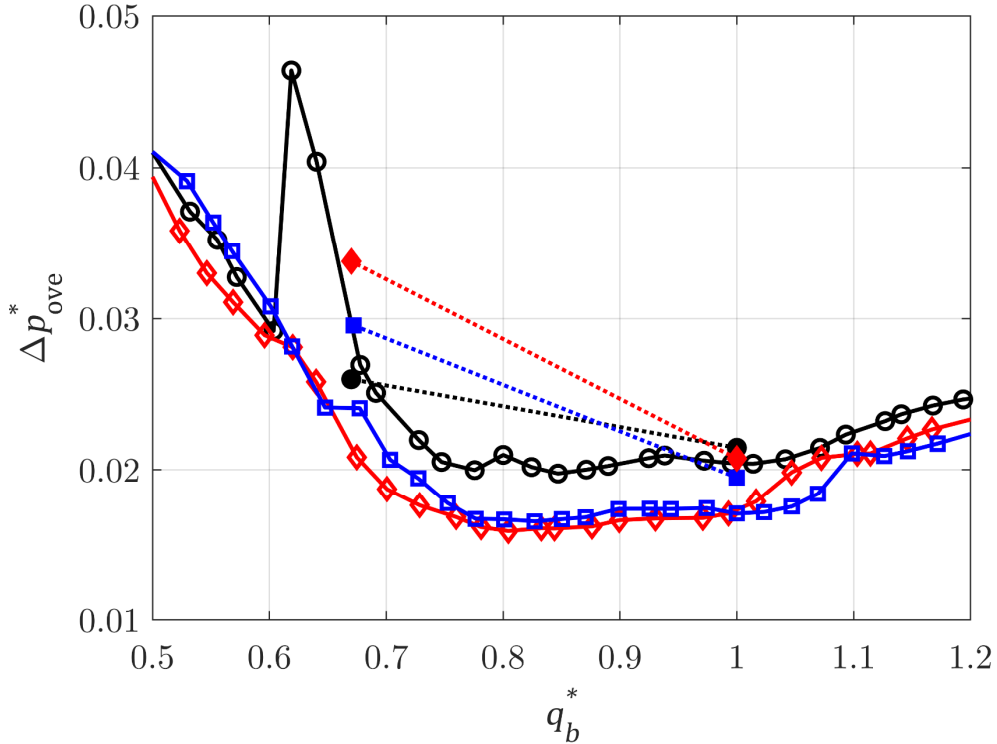


Figure 6.13: Overall RMS values of dimensionless pressure-pulsations at PT31 for the different meridional-widths; Test-01 – black \circ , Test-05 – blue \square , Test-06 – red \diamond ; measurement – solid line with empty symbol, CFD – dotted line with filled symbol

because of its significant impact on vibration level and minimum operable flow-rate of a pump. The findings in this chapter suggest that the current CFD method is not likely to provide reliable information about the influence of a change of hydraulic design parameters on pressure pulsations since the quantitative accuracy of the numerical prediction is not good enough. More importantly, the tendency of Δp_{ove}^* variation for the different meridional-widths is not correctly estimated at part-load.

6.3 Effect of Width Ratio

The influence of b_3/b_2 on the head curve is investigated at a constant b_2^* . The impeller with middle b_2^* , which was used for Test-05 in the previous chapter, was installed in the 2nd, 3rd and 4th stage. Then, the diffuser in these stages was replaced in every test with different b_3^* to achieve $b_3/b_2 = 1.0$ and 1.21 for Test 04 and 07, respectively (see Table 1.2 for the test program).

Figure 6.14 presents overall-head curves and meridional sections of the different b_3/b_2 . The upper figure is for the whole flow-range and the lower figure is a zoomed view in a range of $q_b^* = 0.5 \sim 0.8$. The red, blue and black line indicate the largest, middle and smallest b_3/b_2 , respectively. All data are based on the experiments. The three head-curves are almost identical above $q_b^* = 0.8$ because the diffusers were designed to aim at the same specific-speed and BEP flow-rate. However, once flow recirculation appears at the impeller outlet, the head curves start to differ depending the meridional-width ratio. Noticeably, the smallest b_3/b_2 suppresses the head-curve instability. The middle and largest b_3/b_2 produces the instability at $q_b^* = 0.67$ and 0.64, respectively. The meridional-width ratio also affects the instability near the onset of inlet recirculation ($q_b^* \approx 0.4$). A possible mechanism is that the different b_3/b_2 has an influence on outlet recirculation, which generates different flow-patterns within the impeller and consequently affects inlet recirculation. All width-ratios give almost identical head at shut-off.

As a matter of fact, the overall test-results in Fig. 6.14 are quite different from the expectation. It was presumed that a larger b_3/b_2 generates a stronger flow-separation at a higher flow-rate due to the increased deceleration of meridional velocity from the impeller outlet to diffuser inlet. Therefore, a larger onset flow-rate of the instability as well as a higher shut-off head was expected with increasing b_3/b_2 . Figure 6.14 shows that the correlation between the width ratio and onset of the instability is not systematic. Most of all, the shut-off head is almost same in all b_3/b_2 , which is hard to explain. The inconsistency of test results may be due to interferences from the test conditions:

- (1) The impellers and diffusers were made of Aluminum. After completion of the b_2^* change tests in Chapter 6.1, the wet Aluminum components had been stored more than two months without proper handling until the b_3/b_2 tests

were carried out. As a result, the surface roughness of the hydraulic components for Test-04 and 07 became very high compared to Test-05 due to the Aluminum corrosion.

- (2) The degree of interaction between the main flow and side-room flow is significantly affected by ISR geometries. During the b_3/b_2 change tests, x_{ov} and s_{ax} could not be kept constant (see the right top of Fig. 6.14(a)) since the impellers, diffusers and interstage casings were originally designed for the b_2^* change tests. The smallest b_3/b_2 had 62% longer x_{ov} than the largest b_3/b_2 . According to [1], the long axial-overlap reduces energy transfer from the main flow to side-room flow. Then, it may contribute to an increase of the shut-off head in some extent, i.e. if x_{ov} were the same in all b_3/b_2 tests, a smaller width-ratio may produce a lower shut-off head. The main geometric dimensions and shut-off head of the three tests are summarized in Table 6.2.

The true effect of b_3/b_2 on pump performances could not be clearly appreciated in the present study. At least, Fig. 6.14 shows a meaningful output that the head-curve instability near $q_b^* = 0.67$ is suppressed in the smallest width-ratio. A systematic test-program is necessary in a future project to investigate the impact of b_3/b_2 on pump performances more in detail.

Table 6.2: Geometric dimensions and shut-off head of Test-04, 05 and 07

	Test-04	Test-05	Test-07
b_3/b_2	1.0	1.1	1.21
Gap A/ r_2	0.008	0.008	0.008
x_{ov}/d_2	0.021	0.017	0.013
$s_{ax,hub}/d_2$	0.013	0.016	0.021
ψ_0	1.21	1.21	1.21

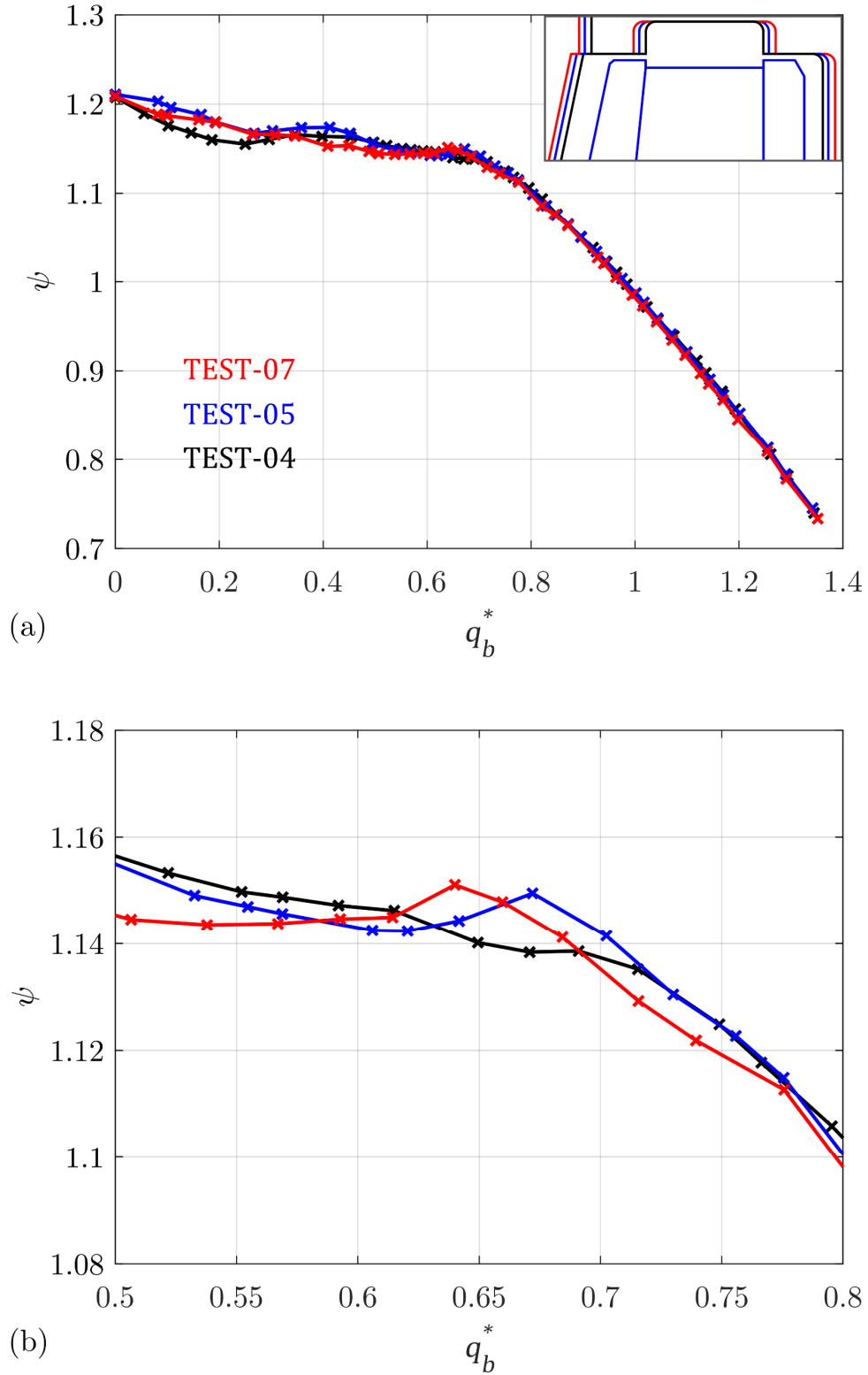


Figure 6.14: Overall-head curves of different b_3/b_2 from the measurement; Test-04 – black, Test-05 – blue, Test-07 – red; (a) the whole operating-range, (b) close-up view in a range of $q_b^* = 0.5 \sim 0.8$

7 Conclusion

The cause of head-curve instability and impact of meridional width on pump performances were investigated in a 4-stage diffuser-type pump at around $n_q = 30$. There were two instabilities in the measured overall-head curve. The internal-pressure measurements showed that a large head-drop occurred in the suction stage at $q_b^* = 0.41$ that was related to flow recirculation and pre-rotation at the impeller inlet. The instability at $q_b^* = 0.67$ was caused by an excessive head-loss in the inlet triangular section of the diffuser. The pressure profiles in the side room and velocity distributions at the impeller outlet showed that outlet recirculation suddenly moved from the shroud to hub when the pump ran at the onset flow-rate of the instability. This flow pattern switching generated a large momentum-exchange between streamlines in the inlet triangular section. The consequent massive mixing-loss was the main cause of the head-curve instability.

Using three impellers and diffusers with different meridional-widths, the impact of meridional width on pump performances was investigated at a constant $b_3/b_2 = 1.1$. A larger meridional-width intensified outlet recirculation, leading to a higher power-consumption and head-generation at shut-off. The efficiency curve became flatter near BEP as the width decreases. However, the onset flow-rate of the instability did not vary systematically with the meridional width. The unstable head-curve was observed in all tests at a range of $q_b^* = 0.62 \sim 0.68$. There was a consistent trend that the average rotation factors in the ISR abruptly varied at the onset of the instability, suggesting that the flow pattern switching occurred in all meridional-widths. Flow quality at the impeller outlet tended to vary (in some extent) in a counter-acting manner in the span-wise and pitch-wise direction as the meridional width decreased. As a result, there was a significant influence of the meridional width on the pressure pulsations and efficiency of the pump. The optimum performances were achieved at the middle and smallest width in the present specification. A sharp rise in Δp_{ove}^* was observed at the diffuser inlet when the pump with the largest

meridional-width operated at the onset of the instability. The coherence between two pressure-pulsation sensors suggested an occurrence of the diffuser rotating-stall at $f = 1.17$ Hz. Even though all three tests showed the head-curve instability, the rotating stall appeared only in the largest meridional-width. It suggests that the head-curve instability is not necessarily accompanied by the rotating stall.

The uncertainty in the CFD prediction of pressure pulsations was investigated based on experimental and numerical-simulation data collected in the 4-stage model pump. The prediction accuracy significantly varied with the sampling position and operating flow-rate. The best prediction-accuracy was observed when the sampling was done at the diffuser inlet and the operating point was larger than the onset of outlet recirculation. The CFD simulations predicted a wrong tendency of Δp_{ove}^* variation at part-load while the meridional-width was changed. The measured Δp_{ove}^* at the diffuser inlet monotonically decreased with decreasing meridional-width, but the predicted outputs were exactly opposite.

Some efforts were made to analyze the influence of the meridional width-ratio on the head curve using the available hydraulic-components. Test results with three different width-ratio at a constant b_2^* were presented. However, true effect of b_3/b_2 on pump performances could not be clearly assessed in the current study due to interferences from the test conditions: corrosion of the hydraulic components and different ISR geometries. A systematic test-program is necessary in a future project for b_3/b_2 study.

References

- [1] Gülich, J. F., and Egger, R., 1992, “Part-Load Flow and Hydraulic Stability of Centrifugal Pumps,” Final Report EPRI TR-100219.
- [2] Gülich, J. F., 1995, “Untersuchungen zur sattelförmigen Kennlinien-Instabilität von Kreiselpumpen,” *Forschung im Ingenieurwesen*, 61, pp. 93-105.
- [3] Gülich, J. F., 2014, *Centrifugal Pumps*, Springer.
- [4] Hergt, P., and Starke, J., 1985, “Flow Patterns Causing Instabilities in the Performance Curves of Centrifugal Pumps with Vaned Diffusers,” *Proc. 2nd Int. Pump Symp.*, Houston, Texas, pp. 67-75.
- [5] Hergt, P., and Jaberg, H., 1990, “Die Abströmung von Radiallaufrädern bei Teillast und ihr Zusammenhang mit der Volllastinstabilität,” *KSB Technische Berichte No. 26*, pp. 29-39.
- [6] Schill, J. H., 1998, “Turbine-Driven High-Powered Boiler Feed Pumps,” *Proc. 3rd Int. Conf. Pumps and Fans*, Tsinghua University, Beijing, pp. 20-35.
- [7] Kanki, H., Kawata, Z., and Kawatani, T., 1981, “Experimental Research on the Hydraulic Excitation Force on the Pump Shaft,” *ASME Paper*, 81DET-71.
- [8] Eisele, K., Zhang, Z., Casey, M. V., Gülich, J. F., and Schachenmann, A., 1997, “Flow Analysis in a Pump Diffuser - Part1: LDA and PTV Measurements of the Unsteady Flow,” *ASME J. Fluids Eng.*, 119, pp. 968-977.

- [9] Ardizzon, G., and Pavesi, G., 2004, “Analysis of Unsteady Impeller Diffuser Interaction in a Centrifugal Pump,” Proc. 22nd IAHR Symp. on Hydraulic Machinery and Systems, June 29-July 2, Stockholm, Sweden.
- [10] Kaupert, K. A., 1997, “Unsteady Flow Fields in a High Specific Speed Centrifugal Pump,” Doctoral Dissertation, ETH Zürich.
- [11] Agostinelli, A., Nobles, D., and Mockridge, C. R., 1960, “An Experimental Investigation of Radial Thrust in Centrifugal Pumps.” ASME J. Eng. for Power, 82, pp. 120-126.
- [12] Hergt, P., and Krieger, P., 1969, “Radial Forces in Centrifugal Pumps with Guide Vanes,” Proc. the Institution of Mechanical Engineers, 184, Issue 14, pp. 101–107.
- [13] Gülich, J. F., 1987, “Influence of Interaction of Different Components of Hydraulic Pump Performance and Cavitation,” Proc. Power Plant Pumps Symp., New Orleans, EPRI CS-5857.
- [14] Van Esch, B. P. M., 2009, “Performance and Radial Loading of a Mixed-Flow Pump Under Non-Uniform Suction Flow,” ASME. J. Fluids Eng., 131(5), 05110.
- [15] Lewis, R. I. 1996, Turbomachinery Performance Analysis, Elsevier Science & Technology Books.
- [16] Van der Schoot, M., and Visser, F. 2015, “Efficiency Upgrade of a Double-Case Pump using CFD-Based Design Optimization and Scaled Model Tests,” Proc. ASME-JSME-KSME Joint Fluids Eng. Conf., July 26-31, Seoul, Korea, AJKFluids2015-33379.
- [17] Karassik, I. J., Messina, J. P., Cooper, P., and Heald, C. C., 2008, Pump Handbook, McGraw-Hill.
- [18] Baun, D. O., and Flack, R. D., 2003, “Effects of Volute Design and Number of Impeller Blades on Lateral Impeller Forces and Hydraulic Performance,” Int. J. Rotating Machinery, 9(2), pp. 145-152.

- [19] Riegger, H. and Nicklas, A., 1995, "Modern Manufacturing of Advanced Impeller and Diffuser Vane Profiles," Proc. 12th Int. Pump Users Symp., Houston, Texas, pp. 37-46.
- [20] Gülich, J. F., 2001, "Selection Criteria for Suction Impellers of Centrifugal Pumps," World Pumps, Parts 1, 2 and 3.
- [21] Balasubramanian, R., Sabini, E., and Bradshaw, S., 2011, "Influence of Impeller Leading Edge Profiles on Cavitation and Suction Performance," Proc. 27th Int. Pump Users Symp., September 12-15, Houston, Texas, pp. 1-11.
- [22] Visser, F. C., Backx, J. J. M., Geerts, J., Cugal, M., and Torres, D. M. M., 1998, "Pump Impeller Lifetime Improvement through Visual Study of Leading-Edge Cavitation," Proc. 15th Int. Pump Users Symp., Houston, Texas, pp. 109-117.
- [23] Cooper, P., Ungewitter, R., Farooqi, R., McKenzie, J., Schiavello, B., and Robinson, W., 2011, "Reduction of Cavitation Damage in a High-Energy Water Injection Pump," Proc. ASME-JSME-KSME Joint Fluids Eng. Conf., July 24-29, Hamamatsu, Japan, pp. 515-529, AJK2011-06092.
- [24] Van den Berg, N., Bastiaansen, T., and Elebiary, K., 2015, "Predicting, Improving and Visualizing Cavitation Characteristics of First-Stage Impellers in High-Speed, High-Energy Pumps," Proc. ASME-JSME-KSME Joint Fluids Eng. Conf., July 26-31, Seoul, Korea, pp. 2503-2510, AJKFluids2015-33420.
- [25] Gülich, J. F., Florjancic, D., and Pace, S. E., 1989, "Influence of Flow between Impeller and Casing on Part-Load Performance of Centrifugal Pumps," ASME FED, 81, pp. 227-235.
- [26] Makay, E., and Barret, J. A., 1984, "Changes in Hydraulic Component Geometries Greatly Increased Power Plant Availability and Reduced Maintenance Cost: Case Histories," Proc. 1st Int. Pump Symp., Houston, Texas, pp. 85-97.

- [27] Kneip, B., 2008, "Beeinflussung der Kennliniensteigung von Gliederpumpen," Doctoral Dissertation, Technical University Kaiserslautern.
- [28] Yamashita, T., Watanabe, S., Hara, Y., Watanabe, H., and Miyagawa, K., 2015, "Measurements of Axial and Radial Thrust Forces Working on a Three-Stages Centrifugal Pump Rotor," Proc. ASME-JSME-KSME Joint Fluids Eng. Conf., July 26-31, Seoul, Korea, AJKFluids2015-33515.
- [29] Yedidiah, S., 1972, "Some Causes of Unstable Performance Characteristics of Centrifugal Pumps," ASME 17th Int. Gas Turbine Conf., San Francisco, California, pp. 5-14.
- [30] Breugelmans, F. A. E., and Sen, M., 1982, "Prerotation and Fluid Recirculation in the Suction Pipe of Centrifugal Pumps," Proc. 11th Int. Pump Users Symp., Houston, Texas, pp. 165-180.
- [31] Hergt, P., Nicklas, A., Mollenkopf, G., and Brodersen, S., 1994, "The Suction Performance of Centrifugal Pumps Possibilities and Limits of Improvements," Proc. 13th Int. Pump Users Symp., Houston, Texas, pp. 13-25.
- [32] Zangeneh, M., Goto, A., and Takemura, T., 1996, "Suppression of Secondary Flows in a Mixed-Flow Pump Impeller by Application of Three-Dimensional Inverse Design Method: Part 1 – Design and Numerical Validation," ASME J. Turbomachinery, 118, pp. 536-543.
- [33] Goto, A., Takemura, T., and Zangeneh, M., 1996, "Suppression of Secondary Flows in a Mixed-flow Pump Impeller by Application of Three-Dimensional Inverse Design Method: Part 2 – Experimental Validation," ASME J. Turbomachinery, 118, pp. 544-551.
- [34] Zangeneh, M., Goto, A., and Harada, H., 1998, "On the Design Criteria for Suppression of Secondary Flows in Centrifugal and Mixed Flow Impellers," ASME J. Turbomachinery, 120, pp. 723-735.

- [35] Goto, A., Nohmi, M., Sakurai, T., and Sogawa, Y., 2002, "Hydrodynamic Design System for Pumps Based on 3-D CAD, CFD and Inverse Design Method," *ASME J. Fluid Eng.*, 124, pp. 329-335.
- [36] Benra, F.-K., Dohmen, H. J., and Sommer, M., 2006, "Experimental Investigation of Hydrodynamic Forces for Different Configurations of Single-Blade Centrifugal Pumps," *Proc. 11th Int. Symp. on Transport Phenomena and Dynamics of Rotating-Machinery*, February 26-March 03, Honolulu, Hawaii, ISROMAC-11_2006-011.
- [37] Van den Braembussche, R. A., 2006, "Optimization of Radial Impeller Geometry," In *Design and Analysis of High Speed Pumps*, Educational Notes RTO-EN-AVT-143, Paper 13. Neuilly-sur-Seine, France: RTO.
- [38] Gottschalk, M., 1974, "Untersuchung der Kennlinienstetigkeit von Radialventilatoren," *Institute of Fluid Mechanics and Hydraulic Machinery, Karlsruhe University*, Report Nr. 17, pp. 1-40.
- [39] Florjancic, S., and Frei, A., 1993, "Dynamic Loading on Pumps – Causes for Vibrations," *Proc. 10th Int. Pump Users Symp.*, Houston, Texas, pp. 171-184.
- [40] Robinett, F. L., Gülich, J. F., and Kaiser, T., 1999, "Vane Pass Vibration – Source, Assessment and Correction – A Practical Guide for Centrifugal Pumps," *Proc. 16th Int. Pump Users Symp.*, Houston, Texas, pp. 121-138.
- [41] Schiavello, B., Smith, D. R., and Price, S. M., 2004, "Abnormal Vertical Pump Suction Recirculation Problems due to Pump-System Interaction," *Proc. 21th Int. Pump Users Symp.*, Houston, Texas, pp. 18-47.
- [42] Berten, S., 2010, "Hydrodynamics of High Specific Power Pumps for Off-Design Operating Conditions," *Doctoral Dissertation*, EPFL.
- [43] Berten, S., Hentschel, S., Kieselbach, K., and Dupont, P., 2011, "Experimental and Numerical Analysis of Pressure Pulsations and Mechanical Deformations in a Centrifugal Pump Impeller," *Proc.*

ASME-JSME-KSME Joint Fluids Eng. Conf., July 24-29, Hamamatsu, Shizuoka, Japan, AJK2011- 06057.

- [44] Kikuyama, K., Minemura, K., Hasegawa, Y., Asakura, E., and Murakami, M., 1987, "Unsteady Pressure Distributions on the Impeller Blades of a Centrifugal Pump-Impeller Operating Off-Design.", Proc. Gas Turbine Conference and Exhibitions, Anaheim, California, ASME-87-GT-144.
- [45] Arndt, N., Acosta, A. J., Brennen, C. E. and Caughey, T. K., 1988, "Rotor-Stator Interaction in a Diffuser Pump," Proc. Gas Turbine and Aeroengine Congress and Exposition, Amsterdam, The Netherlands, ASME-88-GT-55.
- [46] Wang, H., and Tsukamoto, H., 2001, "Fundamental Analysis on Rotor-Stator Interaction in a Diffuser Pump by Vortex Method," ASME J. Fluids Eng., 123, pp. 737-747.
- [47] Shi, F., and Tsukamoto, H., 2001, "Numerical Study of Pressure Fluctuations Caused by Impeller-Diffuser Interaction in a Diffuser Pump Stage," ASME J. Fluids Eng., 123, pp. 466-474.
- [48] Berten, S., Dupont, P., Fabre, L., Kayal, M., Avellan, F., and Farhat, M., 2009, "Experimental Investigation of Flow Instabilities and Rotating Stall in a High-Energy Centrifugal Pump Stage," Proc. ASME Fluids Eng. Division Summer Meeting (FEDSM2009), August 2-5, Vail, Colorado, FEDSM2009-78562.
- [49] Yoshida, Y., Tsujimoto, Y., Kawakami, T., and Sakatani, T., 1998, "Unbalanced Hydraulic Forces Caused by Geometrical Manufacturing Deviations of Centrifugal Impellers," ASME J. Fluids Eng., 120, pp. 531-537.
- [50] Bolleter, U., 1988, "Blade Passage Tones of Centrifugal Pumps," Vibrations 4(3), pp. 8-13.

- [51] Franke, G., Fisher, R., Powell, C., Seidel, U., and Koutnik, J., 2005, "On Pressure Mode Shapes Arising from Rotor/Stator Interactions," *Sound and Vibration*, March, pp. 1-5.
- [52] Guo, S., and Okamoto, H., 2003, "An Experimental Study on the Fluid Forces Induced by Rotor-Stator Interaction in a Centrifugal Pump," *Int. J. of Rotating Machinery*, 9(2), pp. 135-144.
- [53] Zhang, M., and Tsukamoto, H., 2005, "Unsteady Hydrodynamic Forces due to Rotor-Stator Interaction on a Diffuser Pump with Identical Number of Vanes on the Impeller and Diffuser," *ASME J. Fluid Eng.*, 127, pp. 743-751.
- [54] Bolleter, U., Schwarz, D., Carney, B., and Gordon, E. A., 1991, "Solution to Cavitation Induces Vibration Problems in Crude Oil Pipeline Pumps," *Proc. 8th Int. Pump User Symp.*, Houston, Texas, pp. 21-28.
- [55] Gülich, J. F., 1992, "Diagnosis of Cavitation in Centrifugal Pumps," *Sulzer Tech. Review* 1/1992, pp. 29-35.
- [56] Sinha, M., Pinarbasi, A., and Katz, J. 2001, "The Flow Structure During Onset and Developed States of Rotating Stall Within a Vaned Diffuser of a Centrifugal Pump," *ASME J. Fluids Eng.*, 123, pp. 490-499.
- [57] Takamine, T., Furukawa, D., Watanabe, S., Watanabe, H., and Miyagawa, K., 2018, "Experimental Analysis of Diffuser Rotating Stall in a Three-Stage Centrifugal Pump," *Int. J. Fluid Machinery and Systems*, 11(1), pp. 77-84.
- [58] Harris, C. M., and Piersol, A. G., 2002, *Harris' Shock and Vibration Handbook*, McGraw-Hill.
- [59] ISO9906, 2012, *Rotodynamic Pumps – Hydraulic Performance Acceptance Tests – Grades 1, 2 and 3*, Int. Organization for Standardization, Geneva.

- [60] IEC60193, 1999, Hydraulic Turbines, Storage Pumps and Pump-Turbines – Model Acceptance Tests, Int. Electrotechnical Commission, Geneva.
- [61] Bolleter, U., 1993, “Generation and Propagation of Pressure Pulsations in Centrifugal Pump Systems,” AECL Seminar on Acoustic Pulsations in Rotating Machinery, Toronto.
- [62] White, F. M., 1998, Fluid Mechanics, McGraw-Hill.
- [63] Kundu, P. K., Cohen, I. M., and Dowling, D. R., 2012, Fluid Mechanics, Elsevier.
- [64] Kim, J., Moin, P., and Moser, R., 1987, “Turbulence Statistics in Fully Developed Channel Flow at Low Reynolds Number,” J. Fluid Mechanics, 177, pp. 133-166.
- [65] Pope, S. B., 2000, Turbulent Flows, Cambridge University Press.
- [66] Spalart, P. R., Jou, W. -H., Streletst, M., and Allmaras, S. R., 1997, “Comments on the Feasibility of LES for Wings, and on a Hybrid RANS/LES Approach,” Proc. 1st AFOSR Int. Conf. on DNS/LES, Ruston, Louisiana, pp. 137-147.
- [67] Wesseling, P., 2001, Principles of Computational Fluid Dynamics, Springer.
- [68] Kolmogorov, A. N., 1942, “Equations of Turbulent Motion in an Incompressible Fluid,” Izv. Acad. Nauk SSSR, ser. Fiz. 6, p. 56-58.
- [69] Prandtl, L., 1945, “Über ein neues Formelsystem für die ausgebildete Turbulenz,” Nachrichten der Akademie der Wissenschaften in Göttingen, Mathematisch-Physikalische Klasse, 6-19.
- [70] Wilcox, D. C., 1993, Turbulence Modeling for CFD, DCW Industries.
- [71] Menter, F. R., 1993, “Zonal Two Equation $k - \omega$ Turbulence Models for Aerodynamic Flows,” 24th Fluid Dynamics Conf., AIAA 93-2906.

- [72] Menter, F. R., 1994, "Two-Equation Eddy-Viscosity Turbulence Models for Engineering Applications," *AIAA J.* 32(8), pp. 1598-1605.
- [73] Menter, F. R., Kuntz, M., and Langtry, R., 2003, "Ten Years of Industrial Experience with SST Turbulence Model," *Turbulence, Heat and Mass Transfer* 4.
- [74] Braun, O., 2009, "Part-Load Flow in Radial Centrifugal Pumps," Doctoral Dissertation, EPFL.
- [75] Feng, J., Benra, F. -K., and Dohmen, H. J., 2010, "Application of Different Turbulence Models in Unsteady Flow Simulations of a Radial Diffuser Pump," *Forsch Ingenieurwes*, 74, pp. 123-133.
- [76] Juckelandt, K., and Wurm, F. -H., 2015, "Applicability of Wall-Function Approach in Simulations of Turbomachines," *Proc. ASME Turbo Expo*, Montreal, Canada, GT2015-42014.
- [77] Menter, F. R., and Egorov, Y., 2005, "A Scale-Adaptive Simulation Model using Two-Equation Models," 43rd AIAA Aerospace Sciences Meeting and Exhibit, January 10-13, Reno, Nevada, AIAA 2005-1095.
- [78] Menter, F. R., Kuntz, M., and Bender, R., 2003, "A Scale-Adaptive Simulation Model for Turbulent Flow Predictions," 41st Aerospace Science Meeting and Exhibit, January 6-9, Reno, Nevada, AIAA 2003-0767.
- [79] Egorov, Y., Menter, F. R., Lechner, R., and Cokljat, D., 2010, "The Scale-Adaptive Simulation Method for Unsteady Turbulent Flow Predictions. Part 2: Application to Complex Flows," *Flow Turbulence and Combustion*, 85(1), pp. 139-165.
- [80] Menter, F. R., 2015, "Best Practice: Scale-Resolving Simulations in Ansys CFD," ANSYS Germany GmbH.
- [81] Egorov, Y., and Menter, F. R., 2007, "Development and Application of SST-SAS Turbulence Model in the DESIDER Project," *Symp. Hybrid RANS-LES Methods*, Corfu, Greece, pp. 261-270.

- [82] ANSYS, 2011, “ANSYS CFX-Solver Theory Guide,” Release 14.0, Canonsburg, Pennsylvania.
- [83] Chaouat, B., 2017, “The State of the Art of Hybrid RANS/LES Modeling for the Simulation of Turbulent Flows,” *Flow, Turbulence and Combustion*, Springer, 99(2), pp. 279-327.
- [84] Höller, S., Jaberg, H., Benigni, H., and Kim, J. J., 2016, “Low Specific Speed Mixed Flow API Pump for Single and Multistage Usage – Multi-Objective Design Challenge,” *Proc. Int. Rotating Equipment Conf.*, Düsseldorf.
- [85] Höller, S., Jaberg, G., Benigni, H., and Kim, J. J., 2016, “Cavitation Optimization of a Variable Pitch Mixed Flow Pump for Cooling Water by Numerical Methods and Test Rig Verification,” *Proc. Int. Rotating Equipment Conf. Düsseldorf*.
- [86] Lucius, A., and Brenner, G., 2010, “Unsteady CFD Simulations of a Pump in Part Load Conditions using Scale-Adaptive Simulation,” *Int. J. Heat and Fluid Flow*, 31, pp. 1113-1118.
- [87] Ennouri, M., Kanfoudi, H., Bel Hadj Taher, A., and Zgolli, R., 2019, “Numerical Flow Simulation and Cavitation Prediction in a Centrifugal Pump using an SST-SAS Turbulence Model,” *J. Applied Fluid Mechanics*, 12(1), pp. 25-39.
- [88] Launder, B. E. and Spalding, D. B., 1972, *Mathematical Models of Turbulence*. London, Academic Press.
- [89] Rodi, W., and Mansour, N. N., 1993, “Low Reynolds Number $k - \epsilon$ Modelling with the Aid of Direct Simulation Data,” *J. Fluid Mechanics*, 250, pp. 509-529.
- [90] Menter, F. R., and Esch, T., 2001, “Elements of Industrial Heat Transfer Predictions,” *Proc. 16th Brazilian Congress of Mechanical Eng.*, 20, pp. 117-127.
- [91] Menter, F. R., Ferreira, J. C., Esch, T., and Konno, B., 2003, “The SST Turbulence Model with Improved Wall Treatment for Heat Transfer

Predictions in Gas Turbines,” Proc. the Int. Gas Turbine Congress, Tokyo, Japan, IGTC2003-TS-059.

- [92] Currie, I. G. 1993, *Fundamental Mechanics of Fluids*, McGraw-Hill.
- [93] Moin, P., 2010, *Fundamentals of Engineering Numerical Analysis*. Cambridge University Press.
- [94] Bracewell, R. N., 2000, *The Fourier Transform and Its Applications*, McGraw-Hill.
- [95] Wang, H. and Tsukamoto, H, 2003, “Experimental and Numerical Study of Unsteady Flow in a Diffuser Pump at Off-Design Conditions,” *ASME J. Fluids Eng.*, 125, pp. 767-778.
- [96] Figliola, R. S., and Beasley, D. E, 2011, *Theory and Design for Mechanical Measurements*, John Wiley and Sons.
- [97] Meschkat, S., 2004, “Experimentelle Untersuchung der Auswirkungen instationärer Rotor-Stator-Wechselwirkungen auf das Betriebsverhalten einer Spiralgehäusepumpe,” *Doctoral Dissertation*, TU Darmstadt.
- [98] Waitman, B. A., Reneau, L. R. and Kline S. J., 1961, “Effects of Inlet Conditions on Performance of Two-Dimensional Subsonic Diffusers,” *ASME J. Basic Eng.*, pp. 349-360.
- [99] Wolf, S., and Johnston, J. P., 1969, “Effects of Nonuniform Inlet Velocity Profiles on Flow Regimes and Performance in Two-Dimensional Diffusers,” *ASME J. Basic Eng.* pp. 462-474.
- [100] Blevins, R. D. 1984, *Applied Fluid Dynamics Handbook*, Van Nostrand Reinhold Company.
- [101] Fox, R. W. and Kline, S. J. 1962, “Flow Regimes in Curved Subsonic Diffusers,” *ASME J. Basic Eng.*, pp. 303-316.
- [102] Sharan, V. K., 1976, “An Exponential Investigation of the Behaviour of Conical Diffusers in Turbulent Flow,” *J. Applied Mathematics and Physics*. 27, pp. 447-462.

- [103] Hirsch, Ch., Kang, S., and Pointel, G., 1996, “A Numerically Supported Investigation of the 3D Flow in Centrifugal Impellers Part II: Secondary Flow Structure,” Proc. Int. Gas Turbine and Aeroengine Congress and Exhibition, June 10-13, Birmingham, UK, 96-GT-152.
- [104] Spence, R., and Amaral-Teixeira, J., 2008, “Investigation into Pressure Pulsations in a Centrifugal Pump Using Numerical Methods Supported by Industrial Tests,” *Computers & Fluids*, 37, pp. 690-704.
- [105] Spence, R., and Amaral-Teixeira, J., 2009, “A CFD Parametric Study of Geometrical Variations on the Pressure Pulsations and Performance Characteristics of a Centrifugal Pump,” *Computers & Fluids*, 38, pp. 1243-1257.
- [106] Barrio, R., Blanco, E., Parrondo, J., González, J., and Fernández, J., 2008, “The Effect of Impeller Cutback on the Fluid-Dynamic Pulsations and Load at the Blade-Passing Frequency in a Centrifugal,” *ASME J. Fluids Eng.*, 130, 111102.

List of Supervised Student Thesis

Artur Schimpf	Development of a High-Pressure Test Loop for Centrifugal Pumps	DA 2018
Kevin Tilgner	Numerical Investigation of the Last Stage Diffuser and Discharge Chamber for a Multistage Centrifugal Pump	DA 2018
Ernst Nikolajew	Influence of Near-Wall Mesh Quality on Pump Performances Predicted by CFD Simulation	DA 2020

Curriculum Vitae

Personal Data

Name: Joohyen Kim

Education

2001 – 2005 Bachelor of Science in Mechanical Engineering
Seoul National University

2005 – 2007 Master of Science in Mechanical Engineering
Center for Turbulence and Flow Control Research
Seoul National University
Master's Thesis: Sustainable Sub-Laminar Drag from
Stationary Blowing and Suction in a Channel Flow

Work Experience

2007 – 2009 International Volunteer in Senegal
Korea International Cooperation Agency

2009 – 2015 Research Engineer
Hydraulic Development Group in Research Team
HYOSUNG GOODSPRINGS

2015 – Present Research Engineer
Institute of Fluid Mechanics and Turbomachinery (SAM)
Technical University of Kaiserslautern, Germany
Doctoral Dissertation: Influence of Meridional Width on
Head-Curve Instability and Pump Performances